

**Nanosecond Laser Flash Photolysis Studies for the
Elucidation of Photoinduced Processes
in Different TiO₂ Photocatalysts**

Von der Naturwissenschaftlichen Fakultät der
Gottfried Wilhelm Leibniz Universität Hannover

zur Erlangung des Grades

Doktorin der Naturwissenschaften
(Dr. rer. nat.)

genehmigte Dissertation

von

M. Sc. Jenny Schneider

geboren am 08.11.1985 in Kokpekty (Kasachstan)

2016

Referent: Prof. Dr. rer. nat. Detlef W. Bahnemann

Korreferent: Prof. Dr. rer. nat. Thomas Scheper

Korreferent: Prof. Dr. rer. nat. Oliver Diwald

Tag der Promotion: 26.09.2016

Für meine Familie

Danksagung

An dieser Stelle möchte ich mich bei allen bedanken, die mich während meiner Promotion unterstützt und begleitet haben.

Zuerst möchte ich mich ganz besonders bei Prof. Bahnemann für die Betreuung meiner Arbeit bedanken. Ich danke für die anregenden Diskussionen, für das entgegengebrachte Vertrauen, für die Möglichkeit an verschiedenen Projekten mitwirken zu können und für die Freiheit der Entwicklung und Realisierung eigener Ideen.

Prof. Dr. Thomas Scheper danke ich recht herzlich für die Möglichkeit am Institut für Technische Chemie zu promovieren und für die Übernahme des Korreferats.

Prof. Dr. Oliver Diwald danke ich ganz herzlich für die Bereitschaft zur Übernahme des Korreferats.

Prof. Dr. Jürgen Caro danke ich ganz herzlich für die Übernahme des Drittprüferamtes.

Ganz herzlich möchte ich mich bei Dr. Ralf Dillert für die kritischen und produktiven Diskussionen, sowie für die Weitergabe seiner enormen Erfahrung und seines Wissens bedanken.

Ich möchte mich bei Dr. Tarek Kandiel für die Betreuung meiner Arbeit im früheren Stadium und für die Hilfestellung bei der Inbetriebnahme der Laser-Blitz-Photolyse-Anlage bedanken.

Ein großer Dank geht an alle Mitarbeiter des Arbeitskreises Bahnemann, alle ausländischen Kollegen und das gesamte Institut für Technische Chemie für die angenehme Zusammenarbeit und die schöne Zeit.

Ganz besonders möchte ich mich bei Prof. Dr. Cecilia Mendive, Dr. Amer Hakki, Mariano Curti und Konstantin Nikitin für deren Mitwirkung bei der Entwicklung der Ideen für die Interpretation der in dieser Doktorarbeit erzielten Ergebnisse bedanken. Zudem möchte ich Konstantin Nikitin für die EPR- und Raman-Analyse danken.

Ich möchte mich herzlich bei Faycal Atitar, Ana Blanco, Pilar Esteban, Maryam Jami und Irina Ivanova für die Freundschaft und für die schönen Momente innerhalb und außerhalb der Arbeitszeit bedanken.

Ich danke Irina Ivanova für die tolle Zusammenarbeit, für die vielen Diskussionen und für ein offenes Ohr bei all meinen Belangen.

Ich möchte mich ganz herzlich bei meinen Freunden und meiner Familie, insbesondere bei meinen Eltern, für die jahrelange Unterstützung und ihr Vertrauen in mich bedanken. Ich danke meinem Mann Adnan Talafha, der in den schweren Momenten fest an meiner Seite stand.

Kurzzusammenfassung

Während des letzten Jahrzehnts wurde der Synthese von verschiedenen Photokatalysatoren viel Aufmerksamkeit gewidmet, während grundlegende Untersuchungen der zugrunde liegenden photokatalytischen Prozesse nur selten durchgeführt wurden. Die Kenntnis dieser Prozesse ist jedoch von großer Bedeutung für das Verständnis des Reaktionsmechanismus und damit für eine bessere Gestaltung photokatalytischer Systemen. Obwohl Titandioxid (TiO_2) einer der am besten untersuchten Photokatalysatoren ist, gibt es aktuell viele offene Fragen in Bezug auf die Ladungsträgerthermalisierung und ihre Rekombinationskinetik. Die Laserblitzphotolyse-Spektroskopie ist eine weit verbreitete Methode, um solche lichtinduzierten Vorgänge zu untersuchen.

In der vorliegenden Arbeit wurde die Rekombinationsdynamik der lichtinduzierten Ladungsträger in verschiedenen TiO_2 Pulvern mittels der Nanosekunden-Diffusreflektions-Laserblitzphotolyse-Spektroskopie untersucht. Für diese Studien wurden verschiedene Anatas- TiO_2 und Rutil- TiO_2 Proben ausgewählt. Unter gleichen Versuchsbedingungen und bei gleicher Kristallitgröße zeigten die im Anatas erzeugten Ladungsträger kürzere Lebensdauern als die im Rutil gebildeten. Neben dem Einfluss der Morphologie auf die Lebensdauer der Ladungsträger wurde ihre Korrelation mit der Partikelgröße untersucht.

Um den getrappten Elektronen und Löchern in den transienten Absorptionsspektren von TiO_2 den jeweils korrekten Wellenlängenbereich zuzuordnen, wurden Elektronenakzeptoren und -donatoren eingesetzt. Hierdurch konnten die transienten Absorptionssignale im Wellenlängenbereich oberhalb von 450 nm den getrappten Elektronen zugeordnet werden, während die transienten Absorptionen der getrappten Löcher unterhalb von 450 nm detektiert wurden.

Der Anstieg der Laserenergie hatte einen starken Einfluss auf die optischen Eigenschaften der Ladungsträger. Eine detaillierte Charakterisierung der laserbestrahlten TiO_2 Pulverproben zeigte bei diesen erhebliche strukturelle Veränderungen. Sowohl bei Rutil als auch bei Anatas wurde die Bildung langlebiger Ti^{3+} -Zentren detektiert, und es wurde im Falle der reinen Anatas Proben zusätzlich ein Phasenübergang zu Rutil beobachtet. Zudem wurde eine signifikante Zunahme des Absorptionskoeffizienten der getrappten Löcher aufgrund der langlebigen Ti^{3+} -Zentren festgestellt, während die Rekombinationskinetik unverändert blieb. Schließlich konnte ein einheitliches kinetisches Modell hergeleitet werden, um die Zerfallsprofile der erhaltenen transienten Absorptionssignale im Detail zu beschreiben.

Stichwörter: Titandioxid, Laserblitzphotolyse, Transiente Absorptionssignale, getrappte Ladungsträger, Rekombinationsdynamik.

Abstract

During the last decade great attention has been paid to the synthesis of different photocatalysts possessing high photocatalytic activity, whereas fundamental studies concerning the underlying photocatalytic processes have rarely been executed. The knowledge of these processes is, however, of utmost importance for the understanding of the reaction mechanism and thus for a better design of photocatalytic systems. Although titanium dioxide (TiO_2) is one of the most studied photocatalysts until now many open questions are existing concerning charge carrier trapping and charge transfer processes. The Laser Flash Photolysis Spectroscopy is one widely used method to study such fundamental processes.

In the present work the recombination dynamics of the charge carriers photogenerated in different TiO_2 powders have been investigated by means of Nanosecond Diffuse Reflectance Laser Flash Photolysis Spectroscopy. For these studies different 100 % anatase TiO_2 and 100 % rutile TiO_2 samples have been chosen. Provided that the same experimental conditions and the same crystallite size are employed shorter life-times of the photogenerated charge carriers have been found for anatase TiO_2 as compared with rutile TiO_2 . Besides the effect of the morphology and crystallinity on the charge carrier life-time the correlation of the latter with the particle size has been investigated.

To identify the wavelength region in the transient absorption spectra of TiO_2 where the photogenerated electrons and holes absorb, electron acceptors and donors have been employed. In the presence of the former the transient absorption at wavelengths above 450 nm could be attributed to the trapped electrons, while in presence of the latter the transient absorption of the trapped holes below 450 nm has been identified.

The increase of the laser energy had a strong effect on the absorption properties of the charge carriers. A detailed characterization of the employed TiO_2 powder samples following their laser exposure revealed considerable structural changes. For both rutile and anatase, the formation of long-lived Ti^{3+} centers was detected, and in the case of the pure anatase sample a phase transition to rutile occurred. Moreover, the formed Ti^{3+} species lead to enhanced extinction coefficient of the trapped holes, while their recombination kinetics were not affected. Finally, a unified kinetic model could be derived to describe the decay profiles of the obtained transient absorption signals.

Keywords: titanium dioxide, laser flash photolysis, transient absorption signals, trapped charge carriers, recombination dynamics.

Table of contents

1. Introduction and objectives	1
2. Theoretical background	5
2.1 TiO ₂ in the dark.....	5
2.2 TiO ₂ upon bandgap irradiation.....	8
2.2.1 Hole trapping	10
2.2.2 Electron trapping.....	13
2.2.3 Electron-hole recombination.....	15
2.2.4 Electron transfer.....	17
3. Materials and experimental methods	21
3.1 Materials	21
3.2 Experimental methods	22
3.2.1 Diffuse UV-Vis spectroscopy.....	22
3.2.2 Raman spectroscopy	22
3.2.3 EPR spectroscopy	23
3.3 Laser flash photolysis spectroscopy.....	23
4. Results	31
4.1 Effect of laser excitation on the physical and morphological properties of TiO ₂	31
4.2 Effect of laser intensity and energy on the transient absorption signals.....	33
4.2.1 Colloidal anatase TiO ₂ powder	35
4.2.2 Bulk anatase TiO ₂ powder (Hombikat UV100).....	38
4.2.3 Bulk rutile TiO ₂ powder (R15)	42
4.3 Effect of electron donor and of acceptor on the transient absorption signals.....	46
4.3.1 Colloidal anatase TiO ₂ suspensions.....	46
4.3.2 Colloidal anatase TiO ₂ powder	49
4.3.3 Bulk anatase TiO ₂ powder (UV100).....	52
4.3.4 Bulk rutile TiO ₂ powder (R15)	54
4.4 Dependency of the transient absorption signals on the particle size	55
4.4.1 Bulk anatase TiO ₂ powder	56
4.4.2 Bulk rutile TiO ₂ powder.....	58

Table of contents

5. Discussion	61
5.1 Formation of Ti^{3+} centers and anatase to rutile phase transition upon laser exposure	61
5.2 Assignment of the transient absorption spectra	67
5.3 Contribution of the long-lived Ti^{3+} centers to the transient absorption spectra upon high laser excitation density.....	74
5.4 Recombination kinetics of the photogenerated charge carriers	78
5.4.1 Dependency on the laser intensity	78
5.4.2 Dependency on the particle size	90
6. Summary and conclusions	95
7. References	99
8. Appendix	111
A. Determination of the laser intensity	111
B. Transient absorption spectra under O_2 and N_2	112
Publications	113
Curriculum vitae	115

Abbreviations

EPR	Electron Paramagnetic Resonance
TRMC	Time Resolved Microwave Conductivity
TOF	Time of Flight
UV	Ultraviolet ($315 \text{ nm} \leq \lambda < 380 \text{ nm}$)
Vis	Visible ($380 \text{ nm} \leq \lambda < 760 \text{ nm}$)
IR	Infrared
HOMO	Highest Occupied Molecular Orbital
LUMO	Lowest Unoccupied Molecular Orbital
MOs	Molecular Orbitals
DFT-U	Density Functional Theory

Physical Constants

c	Speed of Light in Vacuum ($299\,792\,458 \text{ m s}^{-1}$)
h	Planck's Constant ($6.62606896 \cdot 10^{-34} \text{ J s}$)
N_A	Avogadro Constant ($6.02214179 \cdot 10^{23} \text{ mol}^{-1}$)

Symbols

E_g	Band Gap Energy (eV)
E_{CB}	Conduction Band Edge
E_{VB}	Valance Band Edge
$V_O^{\bullet\bullet}$	Oxygen Vacancy
D_h, D_e	Diffusion Coefficient of hole and electron ($\text{m}^2 \text{ s}^{-1}$)
$O.D.$	Optical Density
R	Reflectance
ΔA	Transient Absorption
ΔJ	Change in Reflection (%)
α	Absorption Coefficient (m^{-1})
ε	Extinction Coefficient ($\text{M}^{-1} \text{ cm}^{-1}$)
λ	Wavelength (nm)
f	Frequency (Hz)
γ_0	Reorganization Energy (eV)
d	Particle Diameter (m)

Abbreviations

r	Particle Radius (m)
V	Volume (L)
V_{EZ}	Volume of the Unit Cell (m^3)
I	Laser Intensity ($\text{J cm}^2 \text{ pulse}^{-1}$)
T	Temperature (K)
ρ	Density (g cm^{-3})
C	Specific Heat Capacity (J g K^{-1})
τ :	Transient Time (s)
t	Time (s)
k_r :	Recombination Rate Constant ($\text{s}^{-1} \text{ M}^{-1}$)
$\langle x \rangle$:	Average Number of Pairs
c :	Concentration (mol l^{-1} or M)
γ	Distribution
V_{BB}	Magnitude of the Band Bending (V)
ϵ_r	Relative Dielectric Constant
N_d	Dopant Concentration (m^{-3})

1. Introduction and objectives

The catastrophic consequences of increased power consumption, such as drastically raising CO₂ levels, natural disasters, and environmental pollution have given reason, in particular, following the earthquake-tsunami disaster in Fukushima, to raise serious concerns about the supply of energy from fossil fuels and nuclear power. Being part of the development of environmentally clean and safe sustainable technologies photocatalysis is attracting increasing attention. The concept of photocatalysis, which includes the conversion of solar into chemical energy by means of a photocatalyst, has been described for the first time in the second decade of the 20th century (1910-1920).¹ At this time, the scientists observed the oxidative degradation of organic molecules such as dye pigments on the illuminated surfaces of metal oxides such as zinc oxide, ZnO, and titanium dioxide, TiO₂. The subsequent research focused on the development of photocatalytic materials for the cleaning of surfaces, air, and water.² After Honda and Fujishima discovered in 1971 the photosensitizing effect of a TiO₂ electrode for the electrolytic splitting of water into hydrogen and oxygen, photocatalysis gained additional significance as a potential method for the storage of solar energy in the form of hydrogen gas.³

Despite years of intensive research the photocatalytic activity of the known photocatalysts is still not sufficient for widespread applications. The development of new effective photocatalysts is therefore the focal point of research in this field. At the present time this has prompted many research groups to employ so-called high-throughput methods enabling the rapid development of new compounds through a systematic and efficient investigation of a very complex parameter space.⁴ However, until now no real progress could be achieved. Hence, studies concerning the mechanisms of the underlying photocatalytic processes represent an alternative elegant way for the design of efficient, tailored photocatalysts.

In the present study, the laser flash photolysis spectroscopy has been applied to investigate fundamental photocatalytic processes. Herein, the photocatalyst is excited by a pulsed laser in the nanosecond range resulting in the photogeneration of the active species responsible for photocatalysis, that is, the electron-hole pairs, which can be monitored through their respective transient optical absorption signature. The decay time or rather the life-time of these active species varies depending on the morphological and physical properties of the photocatalyst thus determining its photocatalytic activity.⁵

1. Introduction and objectives

TiO₂, being the most investigated photocatalyst, was used in this study as a reference material. Although research on TiO₂ has been carried out for more than 40 years, there are still a lot of conflicting opinions and confusion regarding the underlying photocatalytic reaction mechanism. Hence, it is important to fill the existing knowledge gaps and to use the results obtained here for the development of new photocatalytic materials.

TiO₂ as a semiconductor with a band gap of 3.2 eV absorbs light in the UV range. The applied light energy is used to excite electrons from the filled valence band to the conduction band. The charge carriers thus generated, that is, the electron in the conduction band (a reducing species) and the hole in the valence band (an oxidizing species), migrate to the surface where they can undergo redox reactions with adsorbed molecules. The photocatalytic activity represents the ability of a photocatalyst to convert a certain amount of absorbed photons into the respective redox products. The photocatalytic activity of TiO₂ is limited by the fast recombination of the photogenerated charge carriers, with about 90% of them being lost within a few nanoseconds. This means, that not even 10% "surviving" carriers are responsible for the photocatalytic activity. Using the nanosecond laser flash photolysis spectroscopy it is possible to trace the "fate" and the pathways of these charge carriers. The carriers surviving in the nanosecond range are mostly trapped at surface defects such as under coordinated atoms or at oxygen vacancies. These trap states can, on the one side, serve as recombination centers and thereby adversely affect the activity of the photocatalyst. On the other side, they can act as charge transfer agents, from which the electron transfer can proceed, in particular, to surface-bound molecules. Which function the trap states execute depends, in particular, on the morphological and physical properties of the photocatalyst.

Most of the previous fundamental studies on TiO₂ dealing with the reaction dynamics of the photogenerated charge carriers have been performed employing colloidal TiO₂ suspensions or transparent films.⁶⁻¹⁴ By means of these studies the entire time regime of the photoinduced processes such as formation, trapping, recombination, and transfer of the charge carriers has been analyzed. Moreover, the trapped charge carriers could be spectroscopically characterized with the holes absorbing in the UV-vis and the electrons in the visible-IR spectral region. However, the charge carrier dynamics in bulk commercial TiO₂ powders have rarely been studied, although in many reports the obtained photocatalytic activities have been explained in terms of the respective charge carrier recombination kinetics, even though the latter have not been measured. Hence, in

the present work different commercial TiO₂ powders and self-prepared colloidal nanoparticles are investigated. The particular focus of the studies is directed towards the effect of the morphology and the particle size on the charge carrier trapping behavior and the recombination kinetic.

Moreover, possible irreversible changes of the samples following their laser exposure during the measurement have rarely been studied in detail, although most of the published transient absorption signals detected in TiO₂ do not decay to the initial value observed before the laser pulse but rather exhibit long-lived transients within the respective time scales of observation.^{6, 7, 9, 11, 15, 16} For example, Serpone *et al.*⁶ attributed the observed long-lived transient absorption to deeply trapped electrons formed *via* so-called Auger-processes. Another explanation for these irreversible changes of the optical properties might be an irreversible alteration of material's properties resulting from changes of its stoichiometric composition or from a phase transition. However, until now no experimentally based explanation for any observed permanent change of the optical properties of TiO₂ after laser flash photolysis measurements has been given. Hence, in the present study the laser-induced changes of the optical and morphological properties of TiO₂ photocatalysts are investigated by means of Raman-, EPR-, and UV-vis spectroscopy.

It is the decisive element of this thesis to derive a physical model from the above presented correlations between the life-time of the charge carriers and such parameters as morphology, particle size, number of surface defects, and carrier concentration by which the temporal decay of the transient absorption of active species or charge carriers can be accurately described. This fundamental relationship should, in the future, allow both to understand the properties of other photocatalyst systems and to specifically develop new photocatalysts with higher activities, longer life-times or other improved properties.

2. Theoretical background

Chapter begins with the chemical and physical properties of TiO₂ in the dark. The processes occurring in TiO₂ under illumination such as trapping, recombination, and transfer of the charge carriers will be introduced in chapter 2.2. Herein, the transient absorption signals and spectra obtained by means of laser flash photolysis technique will be presented. At the end different fit models for the description of the photoinduced reaction kinetics obtained from the transient decays will be specified.

2.1 TiO₂ in the dark

TiO₂ occurs in the nature in three crystalline polymorphs, namely rutile, anatase, and brookite. Rutile is thermodynamically the most stable mineral. The metastable anatase and brookite phases convert irreversibly to the rutile phase at temperatures above 600 °C. Anatase and rutile exhibit tetragonal unit-cell structure, while brookite crystalizes in a more complex orthorhombic cell as shown in Figure 2.1 (upper). TiO₆ octahedra in anatase (4 edge sharing partly distorted octahedra) and rutile (2 edge sharing nondistorted octahedra) result in different physicochemical properties.

In TiO₂, as in any semiconductor, the conduction band CB is separated from the valence band VB by a bandgap E_g . Herein, the conduction band is mostly Ti⁴⁺ 3d derived, while the occupied states in the valence band are mostly formed by O²⁻ 2p orbitals. The different local crystal environments of the Ti and the O atoms in the unit cells of the three different TiO₂ phases lead to their different electronic structure. Figure 2.1 (lower) presents the calculated band structure of the three TiO₂ polymorphs. For rutile the calculated bandgap of 1.78 eV is direct at Γ , the calculated minimal bandgap of 2.04 eV for anatase is indirect with the bottom of the CB at Γ and the top of the VB at M, while brookite shows a direct bandgap of 2.2 eV at Γ .¹⁷ The difference in the calculated bandgap energies between the three polymorphs is consistent with the experimental data, although the absolute experimental values for the bandgap energy are larger than the calculated ones, thus the reported experimental bandgap energy for rutile is 3.0 eV¹⁸, for anatase 3.2 eV¹⁹, and for brookite 3.4 eV²⁰.

2. Theoretical background

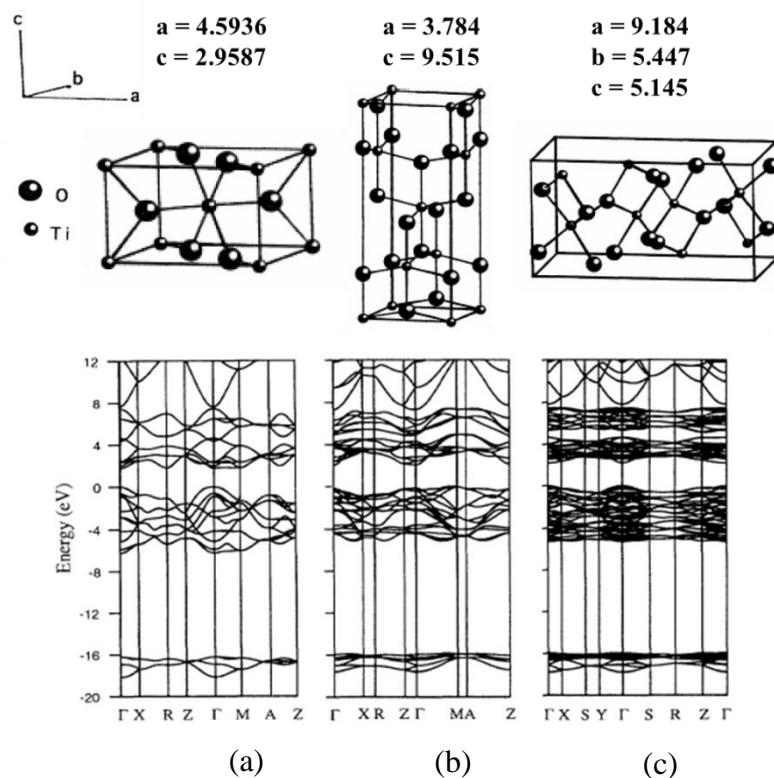


Figure 2.1: (upper) The crystallographic structure of (a) rutile (tetragonal), (b) anatase (tetragonal), and (c) brookite (orthorhombic), respectively with the corresponding lattice constants in Å, respectively. (lower) Calculated band structures of (a) rutile, (b) anatase, and (c) brookite. Adapted with permission from ref.¹⁷ Copyright 1995 American Physical Society.

The energy of the band levels in TiO_2 can vary not only with the crystallite phase but also with the particle size, when the crystallite dimension of a semiconductor particle falls below a critical radius. Figure 2.2 (left) shows how the splitting of the energetic levels proceeds from the HOMO and LUMO orbitals of 2 molecules into a filled and an empty region as the number of contributing MOs increases. In large particles the ensemble of energetic levels becomes dense yielding the valence and the conduction band, respectively. Hence, the apparent bandgap decreases and the band edges E_{CB} and E_{VB} shift with increasing particle size. This so-called quantum-size effect has been quantitatively described by using a quantum mechanical model developed by Brus.²¹ Experimentally the shift of the energetic levels with increasing particle size has been monitored applying spectroscopic methods, where the shift of the absorption onset is detected. For example, Kormann *et al.*²² have reported a red-shift of the absorption onset of 1 eV in the spectra of colloidal TiO_2 nanoparticles during their growth up to a diameter of 3 nm (see Figure 2.2 (right)).

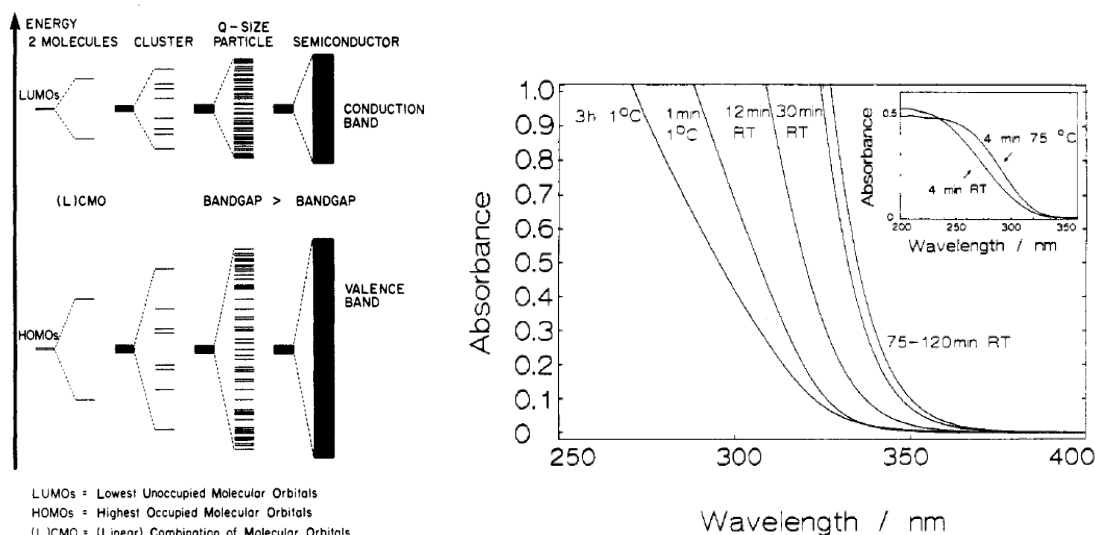


Figure 2.2: (left) MO model for the particle growth of colloidal TiO_2 particles. Reprinted with permission from ref.²³. Copyright (1987) American Chemical Society. (right) Absorption spectra of TiO_2 colloids at various growth stages, obtained by hydrolysis of 5mM TiCl_4 . Reprinted with permission from ref.²². Copyright 1988 American Chemical Society.

The band structures shown in Figure 2.1 (lower) correspond to the intrinsic TiO_2 phase. However, at room temperature TiO_2 contains a lot of different defects. This can drastically alter the electronic structure of the semiconductor by introducing additional energy levels in the middle of the bandgap as shown in Figure 2.3. Oxygen vacancies represent the most common defects in TiO_2 . Such surface defects can be understood as unpaired electrons, which were located initially in an O 2p orbital of the valence band and can then be either transferred, by the removal of the corresponding oxygen atom, into the conduction band under formation of Ti^{3+} centers or remain in the vacancy $V_o^{\bullet\bullet}$ (see Figure 2.3).^{24, 25} Diebold²⁶ concluded from a detailed analysis of this electronic situation, that these extra electrons in the vacancies act as donor-like states. Since most of the defects are located at the particle surface an accumulation layer in the near-surface region occurs. In the presence of acceptor molecules at the TiO_2 surface these additional electrons can be transferred to adsorbed molecules in order to achieve electronic equilibrium leaving empty energy levels in the middle of the bandgap, which can then act as possible traps for the photogenerated electrons.

2. Theoretical background

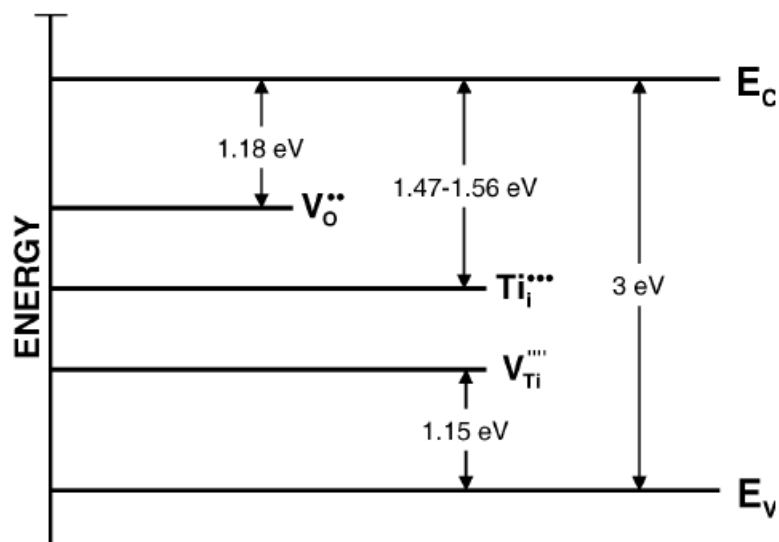


Figure 2.3: Band model of rutile TiO₂ showing the energy levels of intrinsic lattice defects. Reprinted with permission from ref.²⁷ Copyright 2008 American Chemical Society.

2.2 TiO₂ upon bandgap irradiation

The illumination of TiO₂ with an energy $h\nu$ greater or equal to the bandgap energy E_g leads to the excitation of electrons from the valence band into the conduction band. Excitation of TiO₂ is typically thought to pass through an excitonic state (where the electron is bound as a quasi-particle by the hole) followed by the charge separation due to a low exciton binding energy of approx. 4 meV.²⁸ Ultrafast laser flash photolysis experiments have shown that the formation of the electron-hole pairs proceeds within a few femtoseconds after the photon absorption (see Figure 2.4 (1)).

To reduce the excess energy the charge carriers migrate from the bulk to the surface. Enright *et al.*²⁹ observed in nanocrystalline (nc) TiO₂ (anatase) films by means of spectroelectrochemical techniques that the diffusion coefficient for the holes is higher ($D_h = 4 \cdot 10^{-5} \text{ m}^2 \text{ s}^{-1}$) than that of the electrons ($D_e < 1 \cdot 10^{-6} \text{ m}^2 \text{ s}^{-1}$). Lantz *et al.*³⁰ reported similar hole mobilities in rutile. Using these values the average transit time of the photogenerated charge carriers from the bulk to the surface of the particle can be calculated by:⁸

$$\tau = \frac{r^2}{\pi^2 D} \quad (2.1)$$

With a particle radius r of 10 nm the transit time for the holes is 250 fs and that for the electrons > 10 ps.

Once they reach the surface the charge carriers can be trapped at pre-existing defect states thus reducing their motion speed. Di Valentin *et al.*³¹ reported that holes and electrons populate surface sites due to the following reasons: 1. The lattice relaxation associated with the trapping is more feasible at the surface than in the bulk because of the possibility for the surface structure to relax with fewer constraints. 2. At the surface the energy levels calculated for the self-trapped charge carriers are deeper in the gap with respect to the bulk levels, confirming that there is a driving force for electrons and holes to migrate to the surface.

One of the first studies focused on the charge transfer dynamics of these systems was performed by Rothenberger *et al.*¹⁵ employing colloidal TiO₂ nanoparticles. The required time for the electron transfer to their respective surface traps was found to be > 30 ps, while the hole trapping time was reported to be 250 ns. In more recent studies much faster trapping times have been obtained, thus the trapping at the shallow traps (energetically close to the conduction or valence band) has been found to be in the time range between 50 to 200 fs for photogenerated electrons and holes, while the relaxation of the electrons into deeper traps (energetically in the middle of the bandgap) occurs within 500 ps (see Figure 2.4 (2)-(5)).³²⁻³⁴

These fast charge carrier trapping times indicate that both, the electrons and the holes can be rapidly localized at the surface of the semiconductor evincing efficient charge separation. This is one of the reasons why TiO₂ exhibits relatively high reactivity for various photocatalytic reactions.^{5, 35}

However, the time-resolved spectroscopic studies reveal that most of the photogenerated electron-hole pairs recombine rapidly, thus after a few nanoseconds only 10 % of the initially generated charge carriers remain (see Figure 2.4 (6)-(7)). The surviving charge carriers can be transferred to surface adsorbed molecules initiating different reduction and oxidation reactions (see Figure 2.4 (8)-(12)).

All photoinduced processes presented in Figure 2.4 such as trapping, recombination, and interfacial charge transfer will be discussed in more detail in the next chapter.

2. Theoretical background

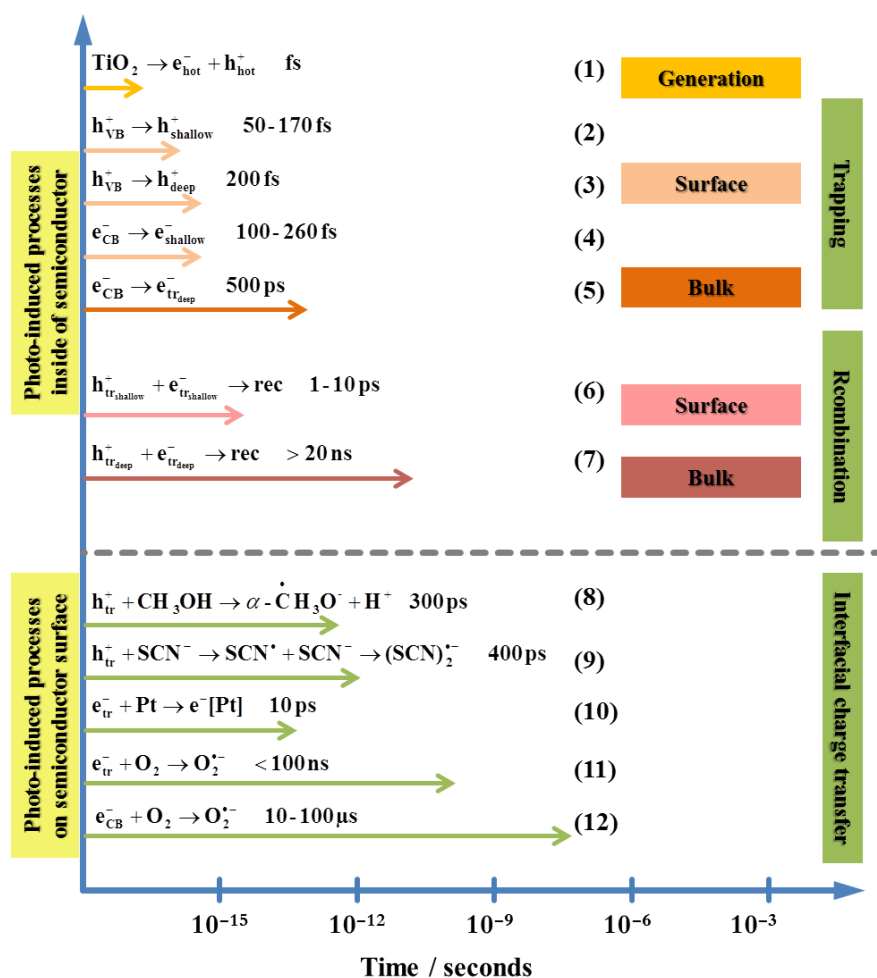
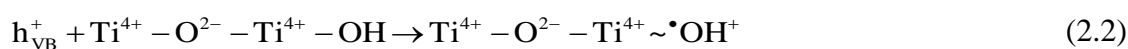


Figure 2.4: Photoinduced reactions in TiO_2 photocatalysis with the corresponding timescales. Adapted with permission from ref.⁵ Copyright 2014 American Chemical Society.

2.2.1 Hole trapping

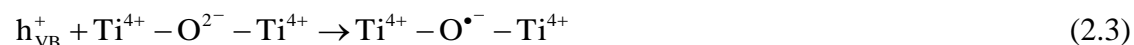
Many studies have been performed to establish the chemical nature of the trapping sites for photogenerated holes in TiO_2 .²⁸ Generally, it is assumed that holes can be trapped at low coordinated oxygen atoms present at the particle surface. Ti^{4+} vacancies represent further possible trapping sites in p-type TiO_2 .³⁶ However, the most controversial point in the discussions concerning the trapping of the holes is, whether superficially adsorbed hydroxyl groups, or surface bound oxygen atoms can trap the photogenerated holes. Older reports propose the hydroxyl radical $\cdot\text{OH}$ generation as a result of the hole trapping:³⁷⁻³⁹



Recently, W. Choi and coworker reported direct observation of the generation and the subsequent diffusion of $\cdot\text{OH}$ radicals from the illuminated TiO_2 surface to the solution

bulk using a single-molecule detection method.⁴⁰ Herein, the mobile $\cdot\text{OH}$ is found to be generated on anatase but not on rutile, thus this molecular phenomenon could explain the different macroscopic behavior of anatase and rutile in photocatalysis.

Other groups reported results, which clearly showed that the primary products of the hole trapping are not superficially bound or free hydroxyl radicals but rather oxygen radical anions in the TiO_2 lattice:⁴¹⁻⁴⁴



According to the results discussed above the trapped holes are considered to be localized at certain surface sites. This can be the case at very low temperatures, as for example during the Electron Paramagnetic Resonance spectroscopy (EPR) measurements (an experimental technique to monitor the formation of paramagnetic species) with the hopping of the charge carriers being limited and thus more localized trapped states will be formed. Nevertheless, at room temperature the photogenerated holes will rather be trapped at different locations distributed over a certain radius within the surface layer, with this surface of the particles having a thickness that can range between 0.35 nm⁴⁵ and several atomic layers.⁴⁶ In this way the trapped holes do not remain localized at certain surface sites, but are rather delocalized over the surface region. Shapovalov *et al.*⁴⁷ have, for example, suggested that the holes can be delocalized over at least two surface oxygen atoms, and can be transferred between surface oxygen atoms and adsorbed species, thus, both $\text{O}^{\bullet-}$ and $\cdot\text{OH}$ species can be formed. These results are supported by theoretical DFT-U calculations performed for the TiO_2 (110) surface by Ji *et al.*⁴⁸. These authors reported that in the presence of a water molecule the electron can be transferred from water to a bridging oxygen atom through the formation of a $\cdot\text{OH}$ radical. The latter is adsorbed on the Ti row and shares the hole with an in-plane oxygen atom.

The laser flash photolysis spectroscopy (the measuring principle of which will be presented in chapter 3. Experimental) provides an useful technique to study reaction dynamics and the formation of the trapped states at the TiO_2 surface. Hereby, the transient absorption or the luminescence of the excited states is usually detected. For example, free $\cdot\text{OH}$ and free $\text{O}^{\bullet-}$ exhibit transient absorption spectra with maxima located around 260 nm.⁴⁹ When these free radical groups are, however, located at surficial Ti sites usually a substantial red shift of the transient absorption spectrum results.³⁹ Figure 2.5

2. Theoretical background

shows typical transient absorption spectra of trapped holes observed for colloidal TiO₂ modified with platinum as electron scavenger.

The transient spectra of the trapped holes are slightly different when comparing the results reported by different researchers. The absorption maxima of the trapped holes have been reported to lie in the wavelength region between 350 nm and 630 nm^{7, 11-13, 16, 32, 33, 39, 50-56}, indicating that apparently different trapped states for the holes coexist in TiO₂ particles. Bahnemann *et al.*¹⁶ performed a laser flash photolysis study employing colloidal TiO₂ suspensions and found that at least two different types of holes have to be considered, namely, deeply trapped holes, which are unreactive and exhibit a transient absorption around 450 nm, and shallowly trapped holes, which exist in a thermally activated equilibrium with free holes and possess a very high oxidation potential. These differences in the transient absorption spectra of the trapped holes can also be attributed to the fact that the charge carriers are delocalized over different trapping sites, with the charge carriers being trapped at different energetic depths resulting in broad transient absorption spectra. Moreover, some studies even predict that the [•]OH radicals exhibit different transient absorption features as compared with O^{•-}, with the former absorbing primarily light in the ultraviolet range, while the latter absorb photons in the visible range.^{12, 39}

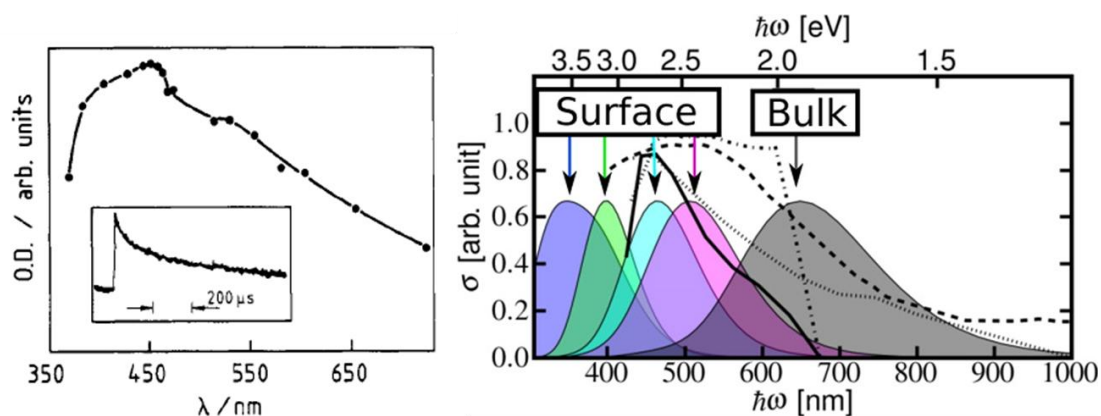


Figure 2.5: (left) Transient optical absorption spectrum observed upon laser flash excitation of an aqueous TiO₂ sol containing deposited colloidal platinum immediately after the laser flash and the corresponding time profile of the absorption at 472 nm (inset). Reprinted with permission from ref.⁷ Copyright 1984 American Chemical Society. (right) Calculated and experimental optical absorption spectra of the self-trapped holes in anatase TiO₂. Absorption bands due to the surface and bulk trapping centers are marked by shaded curves. The experimental spectra are marked with lines: solid (time resolution 50 ns); dashed (measured after 5 ms); dash-dotted (measured after 20 ns); dotted (measured after 20 ms). Reprinted with permission from ref.⁵⁷ Copyright 2013 American Chemical Society.

Although the energetic positions of the trapped states for holes have been reported to be in the range between 1.3 eV and 2.5 eV above the valence band,^{39, 58} the corresponding transition of the excited states has still not been clarified. Either this is a transition from the valence band to the trap state or from the trap state to the conduction band, respectively. Recently, and for the first time, Zawadzki calculated the transient absorption spectra of trapped holes in bulk anatase TiO₂ and on its 001 and 101 surfaces.⁵⁷ According to his calculations the transient absorption can be assigned to the (O²⁻-O⁻) transition, called interpolaron transition. Depending on the distance between neighboring O atoms the transition energy will vary, with higher transition energies corresponding to longer distances. As the result of these calculations the absorption spectra of trapped holes extend from 300 to 800 nm (see Figure 2.5 (right)). Bulk trapped holes exhibit long wavelengths transient absorption spectra due to the fact that the energetic difference between the hole trapping strength at oxygen lattice sites in the bulk is zero while on the surface it is high, since the surface exhibits different oxygen lattice sites.

The analysis of the decay kinetics of the transient absorption signals allows the determination of the trapped charge carrier life-times. The life-time of the trapped holes can be increased from the ps into the ms timescale in the presence of electron acceptors such as Pt as shown, for example, in Figure 2.5 (left).^{6, 7, 11, 16, 33, 50, 56} Their transient absorption signal at 472 nm decays (see Figure 2.5 (left)), most likely, resulting in the formation of surface peroxides according to:



2.2.2 Electron trapping

Generally, it is assumed that the electrons can be trapped at Ti⁴⁺ cations yielding Ti³⁺ species or at oxygen vacancies under formation of the so-called F⁺ and F-centers. Both, theoretical and experimental studies are predicting bulk (subsurface) trapping rather than surface trapping of the photogenerated electrons.^{44, 59, 47, 48, 60} However, alternative studies also exist demonstrating that Ti⁴⁺OH groups located at the TiO₂ surface act as trapping centers for the electrons.^{38, 42, 61} Hoffmann and co-workers assume that the photogenerated electrons can be both surface-trapped as Ti³⁺OH and bulk trapped as Ti³⁺, respectively.^{62, 63}

2. Theoretical background

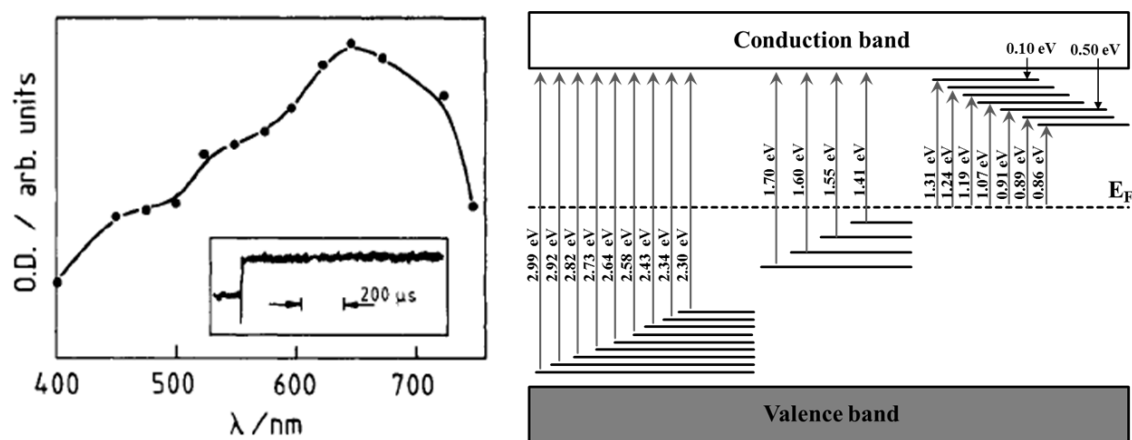


Figure 2.6: (left) Transient optical absorption spectrum observed upon laser flash excitation of an aqueous 5-10 mM polyvinyl alcohol containing TiO_2 sol immediately after the laser flash and the corresponding time profile of the absorption at 625 nm (inset). Reprinted with permission from ref.⁷ Copyright 1984 American Chemical Society. (right) Schematic diagram summarizing the experimentally observed midgap energy levels for the trapped electrons beneath the Fermi level E_F and those for the localized states (shallow trap states) below the conduction band. Adapted with permission from ref.⁶⁴ Copyright 2013 American Chemical Society.

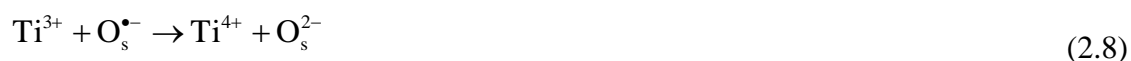
A broad transient absorption spectrum with a maximum around 625 nm has been observed for electrons trapped in TiO_2 in the presence of polyvinyl alcohol (see Figure 2.6 (left)).⁷ Usually, the transient absorption maxima vary in the wavelength region between 600 nm and 800 nm.^{7, 11, 16, 32, 33, 51, 52, 54, 56} This transient absorption is usually associated with the excitation of a trapped electron from its trapping site to the conduction band.⁶⁵ According to the transition wavelength the trap state should be located 1.7 eV below the conduction band. Due to such a decrease of the one-electron reduction power of molecular photogenerated electrons the reduction of the oxygen molecules should not be possible. This contradicts with the literature reporting the peroxy radical anion $\text{O}_2^{\bullet-}$ formation *via* the trapped electrons.¹⁶ Therefore, Bahnemann *et al.*¹⁶ proposed that the transient absorption is due to the excitation of a trapped electron within a surface molecule.

However, it should be noted that the transient absorption spectrum of the trapped electrons is very broad indicating a wide distribution of the trapped states within the entire bandgap (see Figure 2.6 (right)). This could be proven experimentally by

monitoring the transient absorption of the free electrons formed *via* the excitation with energies corresponding to certain transitions from the trapped state to the conduction band.

Some studies report an additional transient absorption in the IR range that has been attributed to the presence of free electrons being distributed in the bulk of the semiconductor particle.¹¹ Such a transient absorption in the near-IR region can be assigned to the transition from the bottom of the conduction band to upper levels within the same band.

Peiro *et al.*⁵¹ studied the life-time of trapped electrons in nc TiO₂ films employing transient absorption spectroscopy and reported in the absence of ethanol (being a potential electron donor) and O₂ (being a potential electron acceptor) a half-life of its absorption signal of ~25 μs. The corresponding decay has been attributed to the recombination at trap sites:



In the presence of ethanol but still in the absence of O₂ the life-time of the trapped electrons was found to increase up to 500 ms. Principally, in the absence of electron acceptors, the transient absorption of the trapped electrons should not exhibit any decay behavior in the presence of a hole scavenger such as ethanol, since no recombination can proceed due to the complete removal of the holes and the remaining Ti³⁺/e⁻ do not react with each other. Moreover, the organic radicals formed upon the oxidation of the hole scavengers, such as hydroxyalkyl radicals like CH₃ĊHOH can inject an additional electron into the conduction band forming the respective aldehyde as stable product, i.e., CH₃CHO (this is the so-called current doubling effect, *vide infra*). Kuznetsov *et al.*⁶⁶ investigated the charge separation and storage in media-wet TiO₂ gels (anatase) and observed that under UV illumination more than 14 % of the Ti⁴⁺ centers are converted into Ti³⁺. The trapped electron life-time was found to be on timescales of months in the absence of oxygen.

2.2.3 Electron-hole recombination

The photocatalytic activities of TiO₂ photocatalysts are usually limited by the fast recombination of the photogenerated electron-hole pairs. Although this process is

2. Theoretical background

undesirable its study provides crucial information concerning the charge carrier dynamics in TiO₂. The recombination of the charge carriers can occur coupled with heat evolution *via* non-irradiative pathways or accompanied by light emission *via* irradiative routes.⁶ Since in TiO₂ the non-irradiative processes dominate they will be presented below.

The non-radiative recombination of the photogenerated charge carriers can be studied by means of time-resolved absorption spectroscopy. According to the reported results, the electron-hole recombination can be affected by many factors such as the sample preparation, the reaction temperature, the charge trapping, the interfacial charge transfer, and the excitation light intensity.^{11, 34, 51, 65, 67-69} Consequently, the life-time of the charge carrier recombination in TiO₂ extends from the ps to the ms time scale. For example, some studies have shown that the recombination rate in rutile is slower than in anatase.^{56, 70} This can be explained by the fact that rutile is usually synthesized at higher temperatures resulting in larger particles with higher crystallinity. Murakami *et al.*⁷¹ have reported that the recombination rate decreases as the calcination temperature increases, since the number of Ti³⁺ trapping sites is reduced acting as the recombination centers. Moreover, Serpone *et al.*⁶ found slower recombination kinetics in larger particles and related this fact to the greater distance between the photogenerated electron-hole pairs.

In many reports the transient absorption decay curve of the trapped charge carriers has been described by second order reaction kinetics according to the bimolecular recombination of the electron-hole pairs coupled by Coulombic forces. Rothenberger *et al.*¹⁵ proposed the recombination process involving trapped electrons and free valence band holes to occur on the picosecond time scale, while on the nanosecond time scale the incorporation of the trapped holes into the recombination process is suggested.¹⁵ Accordingly, this recombination competes with the trapping of the free charge carriers by lattice defects at the surface or in the bulk. Using a stochastic kinetic model Rothenberger and co-workers showed that at high pulse energies (2 mJ), where the number of charge carriers in the particle is high, i.e. >60, their recombination follows second order kinetics, while at very low occupancy of the semiconductor particle by electron-hole pairs their recombination obeys first order kinetics, respectively:¹⁵

$$\langle x \rangle(t) = \frac{\langle x \rangle_0}{1 + \langle x \rangle_0 k_r t} \quad (2.9)$$

$$\langle x \rangle(t) = \langle x \rangle_0 \exp(-k_r t) \quad (2.10)$$

where $\langle x \rangle(t)$ represent the average number of pairs at time t , $\langle x \rangle_0$ at time $t = 0$, and k_r is the recombination rate constant.

The concept for the recombination process of the photogenerated charge carriers proposed by Rothenberger has subsequently been confirmed by other research groups working in this field, although equations 2.4 and 2.5 have been expanded with a further term $f(t)$ to account for the long-lived absorption at the end of the decay.^{6, 34, 69, 72, 73} This long-lived absorption has been attributed to interstitially trapped electrons in the interior of the nanoclusters rather than to ejected electrons resulting from a photo electron emission process as has been proposed by earlier studies.

However, Grela and Colussi argue that bimolecular recombination never follows a second order kinetic rate law claiming that the apparent second order process coupled with a non-zero baseline may be a metaphor hiding the actual nature of the phenomena.⁷⁴ The authors proposed an alternative kinetic model based on a stochastic treatment of the charge carriers in a two-dimensional lattice with the electrons being immobilized at deep traps, while the holes remain mobile or shallowly trapped randomly hopping to their neighbors. Hence, the authors assume that the mobility of the holes determines the recombination process. Cavaleri *et al.*⁷⁵ reported that the model proposed by Grela and Colussi describes the process occurring on the nanosecond time scale correctly, while it does account representatively for the entire recombination process, especially in the picosecond time regime.

2.2.4 Electron transfer

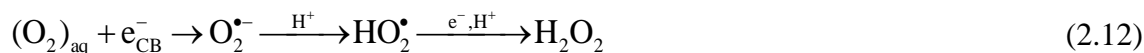
In most photoinduced oxidation processes employing TiO_2 molecular oxygen is added and it is generally assumed that at the reduction site superoxide radical anions are generated according to:



The reduction of molecular oxygen by trapped electrons has been reported to occur within less than 100 ns¹¹, while the reduction process with the free conduction band electrons is found to be 10-100 times slower.^{51, 67} These different reaction dynamics with molecular oxygen can be explained by the fact that the trapped electrons are mostly localized at the surface and thus can be faster transferred to the surface bound oxygen atoms than the bulk located free conduction band electrons, although the former exhibit a lower reduction

2. Theoretical background

potential than the latter.¹¹ Further reduction of the peroxy radical can lead to the formation of hydroxyl radicals according to the following equations:



Some research groups assume this reductive route to be the main source for the hydroxyl radical formation, rather than the water oxidation by the photogenerated holes.^{76,77}

Rabani *et al.*⁷⁸ investigated the interfacial electron transfer to other inorganic molecules besides molecular oxygen such as nitrate, nitrite, perchlorate, and copper. The authors presented results which correlate very well with the predictions of the electron transfer theory developed by Hush and Marcus^{79, 80}. According to this theory, the electron transfer rate constant increases with an increasing electrochemical driving force in the so-called normal Marcus-region, while in the so-called inverted Marcus-region the reactivity decreases again with a further rise of the electrochemical driving force. Hence, Rabani and co-workers found a linear dependency of the electron transfer rate constant on the redox potential of the inorganic molecules.⁷⁸ For both, small and large particles an increase of the one-electron redox potential of the scavenger, E_s , leads, in most cases, to an improvement of the electron transfer kinetics. These results indicate that the electron transfer rate constant can be predetermined on the basis of the redox potential of the reducing species.

Discussing the reduction processes induced by the photogenerated electrons it is important to mention the electron transfer process from TiO_2 to platinum, which is responsible for the photocatalytic generation of molecular hydrogen over platinized TiO_2 . The results from time-resolved diffuse reflectance spectroscopy experiments showed that trapped and free conduction band electrons migrate to the Pt contact within a time interval between 1.4 ps and 2.3 ps, respectively (values have been reported for 1 % Pt/ TiO_2).^{81, 82} As shown in Figure 2.7 (left) the decay rate of the transient absorption at 600 nm increases with increasing Pt-loading indicating that a larger Pt coverage on the TiO_2 surface enhances the probability of electron migration from TiO_2 to Pt.⁸¹ These results are

in agreement with the results of EPR measurements evincing the transfer of electrons from TiO_2 to $\text{Pt}(0)$ as shown in Figure 2.7 (right).⁸³

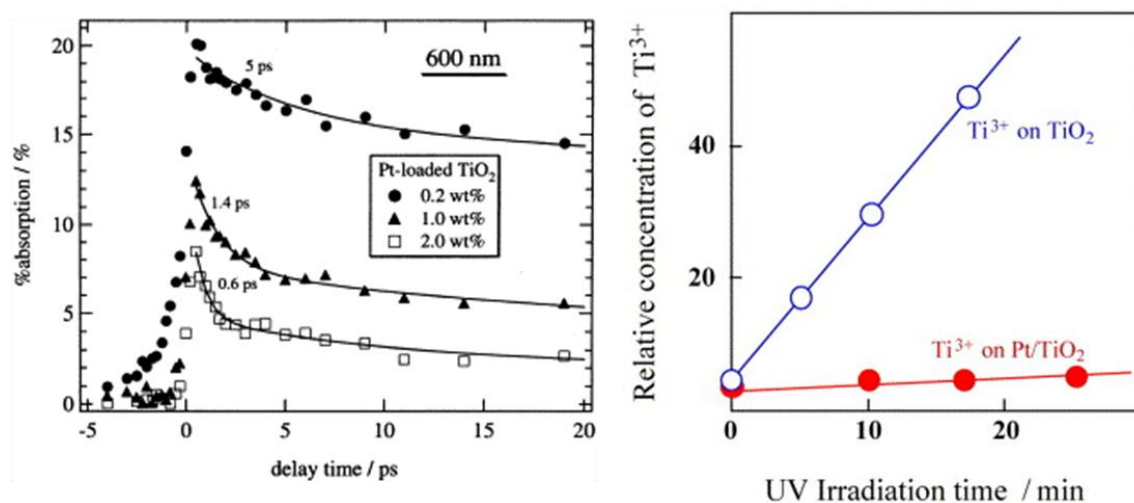


Figure 2.7: (left) Dependence of the transient absorption decay curves measured at 600 nm for Pt-loaded TiO_2 powder on the Pt-loading (wt %) following 390 nm laser excitation. Reprinted from ref.⁸¹. Copyright 2003, with permission from Elsevier. (right) Growth of the EPR signal intensity of the photoformed Ti^{3+} active sites on Pt-loaded and unloaded TiO_2 catalysts (recorded at 77 K). Reprinted from ref.⁸³ Copyright 2001, with permission from Elsevier.

The reaction dynamics of photogenerated holes with molecules adsorbed at the TiO_2 surface have been intensively investigated by means of transient absorption spectroscopy. For example, Tamaki *et al.*⁸⁴ investigated the reaction dynamics of the trapped holes with different alcohols and observed in the presence of the alcohols a rapid decay of the transient absorption of the trapped holes. The life-time of the trapped holes in methanol, ethanol, and 2-propanol was found to be 300 ps, 1000 ps, and 3000 ps, respectively. Generally, it is assumed that the hole induced alcohol oxidation includes the cleavage of the C-H bond resulting in the formation of the respective α -hydroxyalkyl radicals while the formation of the respective aldehyde occurs in the second step under injection of an electron into the conduction band of TiO_2 , called “current doubling”.⁸⁵⁻⁸⁷

While a fast reaction of the trapped holes with different alcohol molecules on the time scale of several ps has been observed, it was shown that holes which manage to survive until the ns time scale possess lower reactivity. These deeply trapped holes exhibiting characteristic transient absorption maxima around 450 nm are neither able to oxidize dichloroacetate, DCA^- , nor thiocyanate, SCN^- , anions. Bahnemann *et al.*¹⁶ concluded from these results that just shallowly trapped holes, being in a thermally activated equilibrium with free holes, are able to initiate such oxidation reactions.

2. Theoretical background

Calculations using the Marcus electron transfer theory for adiabatic processes resulted in a reorientation energy $\gamma_0 = 0.64$ eV suggesting that in the case of SCN^- the hole transfer should occur in the adsorbed state. Furube *et al.*⁸⁸ have indeed observed an ultrafast hole transfer from TiO_2 to surface adsorbed SCN^- taking place in less than 1 ps followed by a subsequent structural stabilization of the formed $(\text{SCN})_2^{\bullet-}$ within a few picoseconds. Moreover, it has been shown that the interfacial electron transfer from the SCN^- to a hole on the photoexcited TiO_2 effectively competes with the electron-hole recombination on an ultrafast time scale.⁶⁹

Frequently, the decay kinetics of the photoinduced electron transfer processes are fitted by a multi-exponential expression, which includes more than two adjustable parameters. Although this mathematical approach may describe perfectly the decay behavior of the transient signal, it does not entail any physical meaning. Hence, to fit the decay signal induced by interfacial electron transfer processes on semiconductor nanoparticles Albery and co-workers developed a kinetic model, which is based on the Gaussian distribution of the logarithm of the rate constants thus introducing only one additional parameter, i.e., the width of the distribution γ :

$$\frac{c}{c_0} = \frac{\int_{-\infty}^{\infty} \exp(-x^2) \exp[-\tau_k \exp(\gamma x)] dx}{\int_{-\infty}^{\infty} \exp(-x^2) dx} \quad (2.16)$$

where c is the concentration of the excited species and τ_k is related to the rate constant k ($\tau_k = kt$). With $\gamma=0$ the expression is converted into the simple first-order exponential decay.

For example, besides other research groups Draper and Fox successfully applied this model to fit experimentally observed transient decay curves and found that the kinetics in TiO_2 powders appear to be first order with a Gaussian distribution of reaction rate constant reflecting the distribution of the particle radii.^{89, 90}

3. Materials and experimental methods

3.1 Materials

Commercial TiO₂

All chemicals were of analytical grade and used as received without further purification. Table 2.1 summarizes the characteristics of the employed TiO₂ materials.

Table 2.1: TiO₂ materials. Manufacturer, phase modification (polymorph), crystalline domain (particle size), and Brunauer–Emmet–Teller (BET) surface area.

Sample	Manufacturer	Phase modification ⁹¹	Crystalline domain ⁹¹	BET ⁹²
			/ nm	/ m ² ·g ⁻¹
PC10	Cristal Global	100% anatase	152	10
PC50	Cristal Global	100% anatase	40	50
PC105	Cristal Global	100% anatase	26	85
PC500	Cristal Global	100% anatase	7	340
S230	Finn-Ti Kemira	100% anatase	7	230
UV100	Sachtleben	100 % anatase	12	-
R15*	Cristal Global	100% rutile	20	65
R25*	Cristal Global	100% rutile	27	42
R34*	Cristal Global	100% rutile	36	33

*Development samples provided by the manufacturer.

Colloidal TiO₂

Colloidal TiO₂ was prepared according to Ref.⁷ by the dropwise addition of 1.33 ml titanium tetraisopropoxide dissolved in 23.11 ml 2-Propanol to 225.76 ml aqueous hydrochloric acid solution of pH 1.5. The total concentrations of titanium tetraisopropoxide and 2-propanol were 1.5·10⁻² and 1.2 M, respectively. The mixture was stirred for two days. The obtained suspension was dried by vacuum evaporation at 30 mbar at 30°C until a white powder of TiO₂ remained. 500 mg of this powder were resuspended in 1 L of water at pH=3. The suspension was optically transparent and showed a steep increase in absorption below 380 nm which is typical for colloidal TiO₂ (see Figure 3.1 (left)). From the Raman spectrum a pure anatase modification of the colloid was identified (see Figure 3.1 (left)). A signal at 1500 cm⁻¹ could be related to the organic groups, which remain after the synthesis of colloidal TiO₂ using tetra isopropoxide as the precursor. The powder received from the drying of the colloidal TiO₂ suspension has been denoted as colloidal TiO₂ powder in the present study.

3. Materials and experimental methods

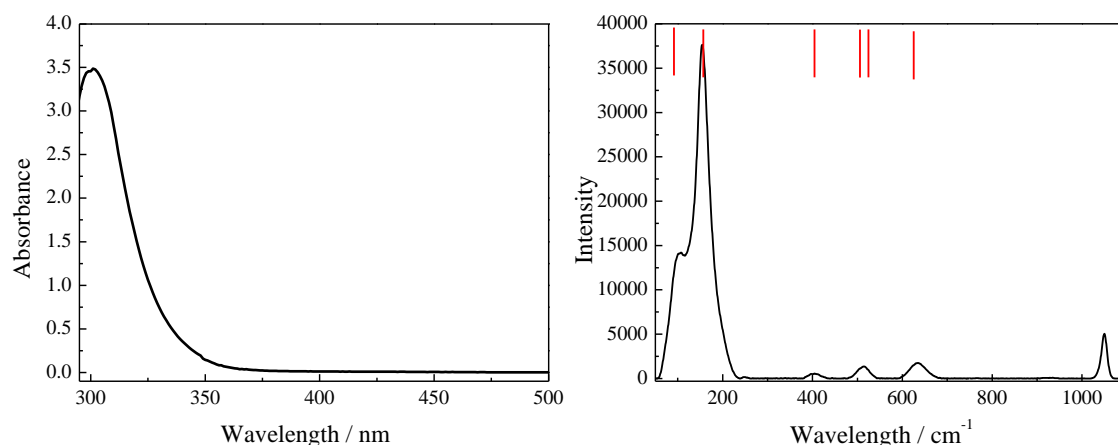


Figure 3.1: (left) UV-vis spectrum of a colloidal TiO₂ suspension (1.5 g/l, pH=3) in water and (right) Raman spectrum of the powder obtained after evaporation of the solvent (red lines indicate reference of anatase phase).

The colloidal TiO₂ was modified with platinum by mixing the above acidic TiO₂ suspension with colloidal platinum in a ratio of 15:1 (%wt). Colloidal platinum was obtained by reducing $3 \cdot 10^{-4}$ M H₂PtCl₆ with $1.7 \cdot 10^{-3}$ M sodium citrate under heating for 1 h at 100 °C. Excess ions were removed with an ion-exchange resin until a specific conductivity of $3\text{-}5 \text{ mS} \cdot \text{cm}^{-1}$ was reached. After evaporation at 30 mbar at 30 °C a brown powder was obtained.

3.2 Experimental methods

3.2.1 Diffuse UV-Vis spectroscopy

Diffuse reflectance spectra of the TiO₂ powders were recorded on a Varian Cary 100 Scan UV-Vis spectrophotometer equipped with a labsphere diffuse reflectance accessory. The reflectance data were converted to F(R) values according to the Kubelka-Munk theory.

3.2.2 Raman spectroscopy

Raman spectra and micrographes were recorded with a SENTERRA Raman microscope. The spectral resolution of the analyzing spectrograph was 0.5 cm^{-1} . A 532 nm laser was used as an excitation source. The power of the laser at the sample was 2.0 mW. The presented spectra were obtained at room temperature by averaging five spectra with an integration time of 10 s.

3.2.3 EPR spectroscopy

EPR spectra were registered with a MiniScope MS 400 X-band EPR spectrometer at liquid nitrogen temperature. The device parameters during the measurements were as follows: microwave frequency 9.42 GHz, microwave power 5 mW, modulation frequency 100 kHz, modulation amplitude 0.15 mT.

3.3 Laser flash photolysis spectroscopy

Equipment

In 1950 Norrish and Porter showed that a very intense flash of light can initiate different chemical reactions, the kinetics of which can be spectroscopically monitored by the second flash lamp fired at a known delay after the first.⁹³ For practically all chemical compounds the absorption of light leads to the formation of transient species *via* oxidation, reduction, isomerization, association, dissociation etc. reactions. This alters the optical properties of the substance, thus the transient species formed after the excitation can be detected by the absorption of light from a continuous or a pulsed analyzing source.

Figure 3.2 demonstrates the underlying processes. Since the excitation process should be completed before decay measurements will start, the pulse duration of the flash of light determines the time resolution. Due to the development of lasers the time scales of the measurement extend nowadays from the nanosecond to the femtosecond domain. This allows to study the formation kinetics of the transient species as well as the subsequent reaction dynamics.

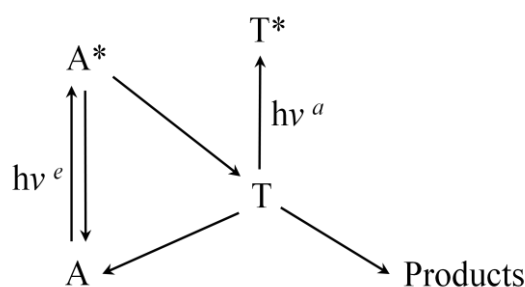


Figure 3.2: Scheme of the flash photolysis principle. Optical excitation $h\nu^e$ of a substance A undergoing photochemical conversion to give a transient T, which may either revert to the ground state of A or decay into other products. The transient is detected by the excitation with the analyzing light $h\nu^a$. Adapted with permission from ref.⁹⁴

Since this invention numerous reports have been published on the flash photolysis technique applied to transparent samples measuring the transmitted light before and after

3. Materials and experimental methods

the excitation. In Ref.^{95, 96} examples for the studies on transparent nanocrystalline semiconductor systems are given.

The first successful report of diffuse reflectance laser flash photolysis on opaque samples was published by Kessler and Wilkinson in 1981.⁹⁷ The transient species were detected after excitation by monitoring the changes in the level of diffusely reflected light. The main difference to the technique used in transmission experiments is the geometrical arrangement of the analyzing light. Herein, the detector and the analyzing light are assembled to insure that no specular reflected light enters the detector and that the maximum amount of the diffusely reflected light is collected and analyzed as shown in Figure 3.3 (left), since the diffusely reflected light has penetrated a substantial portion of the sample and thus contains the information concerning its absorption. The area of the sample that receives the monitoring light should be either equal or smaller than that of the exciting pulse to ensure that all diffusely reflected analyzing light has been probing only those parts of the sample that were excited by the laser. Moreover, the specular and diffuse reflected exciting pulse should be prevented from entering the monochromator to avoid any interference with the analyzing light, the former one *via* this reflection at 45 ° (see Figure 3.3 (left)) and the later one by introducing an appropriate filter at the monochromator entrance. Further requirements for the arrangement of the components are described in detail elsewhere.^{94, 98-100}

A typical experimental set of data obtained with a diffuse reflectance laser flash photolysis apparatus is depicted in Figure 3.3 (right). The baseline for transient absorption measurements is observed by detecting the diffusely reflected signal of the monitoring light from the unexcited sample, while the transient emission decay traces are monitored by recording the signal when only the laser falls onto the sample. The transient absorption decay trace is produced by the simultaneous irradiation of the sample by the laser and the arc lamp.

Figure 3.4 illustrates the time-resolved diffuse reflection laser flash photolysis set-up used in our laboratories. The suitable excitation of the sample proceeds with an excimer laser (LPX 200) provided by Lambda Physic. The pulse duration is 20 ns. Two different excitation wavelengths are available, namely 248 nm and 351 nm. The laser energy per pulse at 248 nm lies between 15-45 mJ and at 351 nm 4-16 mJ (determined with ferrioxalate actinometry, see 8. Appendix). In the diffuse reflectance experiments the laser beam entered the sample at an oblique angle. The angle of the laser beam path can be adjusted by rotating the Pellin-Broca prism beam steering module.

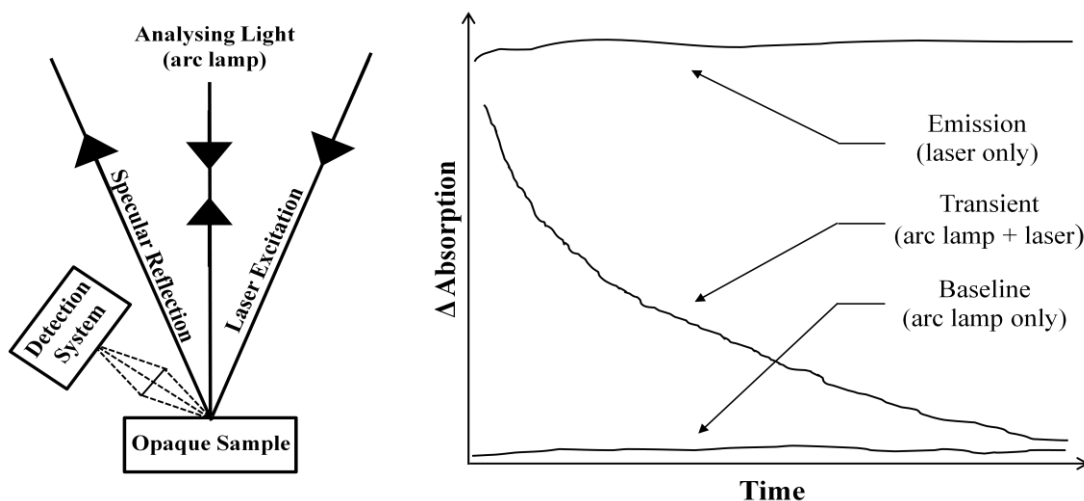


Figure 3.3: (left) Schematic illustration of the sample geometry used in diffuse reflectance laser flash photolysis and (right) a typical set of experimental traces. Adapted with permission from ref.¹⁰¹

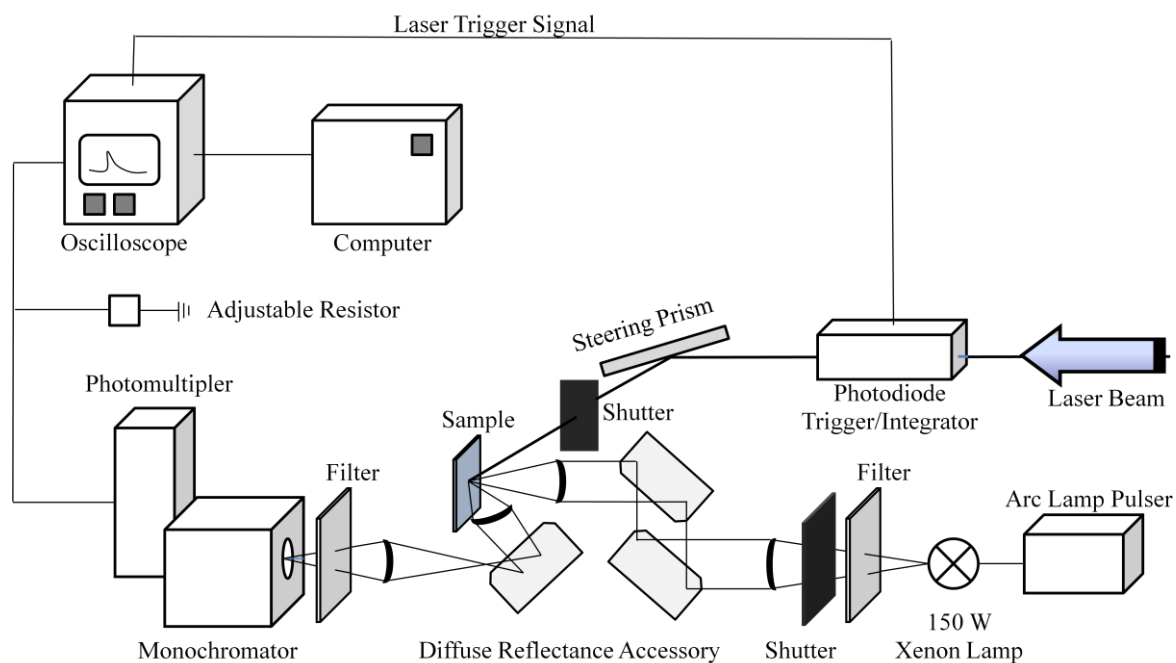


Figure 3.4: Schematic diagram of the nanosecond diffuse reflectance laser flash photolysis apparatus to produce and detect transient absorptions in light-scattering samples.

The change in the reflectance is monitored with the laser flash photolysis spectrometer LKS 80 from Applied Photophysics. The light absorption by the photogenerated transient species is analyzed with a 150 W xenon arc lamp. The pulsing of the xenon lamp for 1.5 ms by a capacitor discharge leads to 50-fold increase of the light intensity. The diffuse reflectance accessory is employed to steer the incoming xenon light beam (*via* two plane folding mirrors) in relation to the main optical axis. A spectroil lens focuses the optical

3. Materials and experimental methods

beam onto the solid sample. The diffusely reflected light from the sample is collected by a second lens. The third folding mirror reflects the converging beam to the monochromator. Subsequently, the monochromator light falls into the photomultiplier detector (Hamamatsu R928 photomultiplier) where it produces a current. The photometric light level falling on the photomultiplier is kept at 100 mV for all measurements by applying the required high voltages of 550-800 V. The current output from the photomultiplier is terminated by the variable signal terminator (set to 100 Ω) inserted onto the signal input socket of the digital oscilloscope. The change in the reflectance is then recorded by the oscilloscope as voltage changes.

To avoid the overloading of the photomultiplier and any interferences with the analyzing light cut off filters at 370 nm for $\lambda_{\text{ex}} = 351$ nm and at 310 nm by $\lambda_{\text{ex}} = 248$ nm have been introduced in the front of the monochromator entrance. Moreover, the UV illumination of the analyzing light with wavelengths < 385 nm has been filtered, when the samples were excited with the laser at 351 nm excitation wavelength. However, the effect of the additional excitation with a Xenon-Lamp could be excluded, since the transients observed with and without the filter were identical.

A dry powder in a quartz cuvette has been used in all diffuse reflectance experiments. Herewith, the illumination area of laser beam and of the analyzing light are 0.5 cm² and 0.196 cm², respectively. The laser irradiation caused the formation of a thin transparent TiO₂ film on the cuvettes wall and the grey-blue coloration of the sample. Due to this undesirable effect, the powder and the cuvette have been exchanged after every 20 pulses. The formed TiO₂ film could be removed by boiling of the cuvette in concentrated sulphuric acid.

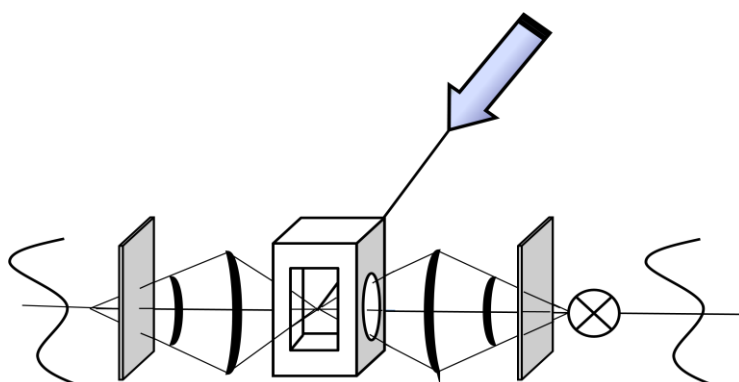


Figure 3.5 Schematic diagram of the sample housing of the nanosecond laser flash photolysis apparatus used for studies on transparent samples.

Figure 3.5 shows the sample housing for the studies on transparent samples. The only difference to the diffuse reflectance measurement set-up is that the laser beam hits the sample perpendicular to the analyzing light.

Data Analysis

For the analysis of the observed transients obtained in transmission mode the Beer-Lambert law is normally applied. Herein, the transient absorption of the photogenerated species is detected as the ratio of the light transmitted by an unexcited sample, I_0 , and the light transmitted after the excitation with the laser I_t :

$$A = -\log\left(\frac{I_t}{I_0}\right) \quad (3.1)$$

For an optically dense sample studied by diffuse reflectance laser flash photolysis the reflected light is measured. The reflectance R is defined as the quotient of the incident intensity of the analyzing light, I_0 , at a wavelength λ_x and the diffuse reflected light, J_0 : $R_0 = J_0/I_0$. If the laser excitation generates a transient species that has an absorption at a wavelength λ_x this will result in the decrease of J_0 to J_x , while I_0 remains constant. Hence, the reflectance will be reduced to R_x . In the case that the transient species has no reaction partner in the system a built-up of the transient occurs, otherwise, if any reaction proceeds, e.g., recombination, reduction, oxidation, etc., the disappearance of the species will lead to an increase of J_x and the decay of the transient can be followed until the original level of J_0 is approached. Mathematically, this can be summarized as:⁹⁸

$$\Delta R = \frac{R_0 - R_x}{R_0} = 1 - R_T^x \quad \text{or} \quad \Delta J = \frac{J_0/I_0 - J_x/I_0}{J_0/I_0} = \frac{J_0 - J_x}{J_0} = 1 - J_T^x \quad (3.2)$$

where R_T^x is defined as R_x/R_0 and J_T^x as J_x/J_0 .

To assign the observed change in reflection after the pulse excitation to the transient absorption and thus to a concentration of the excited states two limiting types of transient concentration profiles should be considered, namely, the homogeneous and the exponentially falling-off profile as depicted in Figure 3.6.

3. Materials and experimental methods

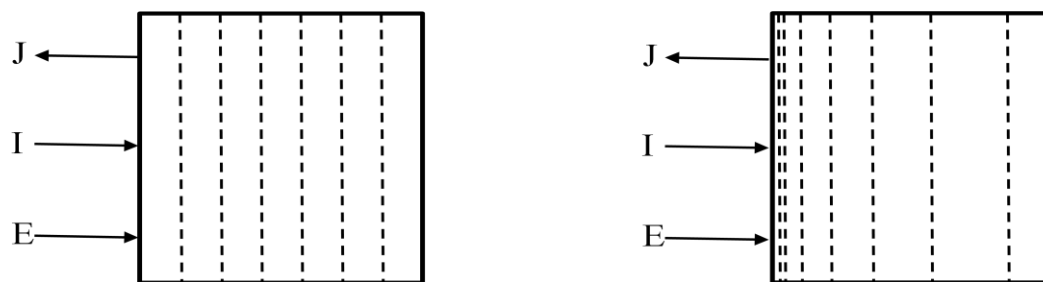


Figure 3.6: Schematic diagram of the (left) homogeneous and (right) exponentially falling-off concentration profile of the photogenerated transient species (*E*: exciting light; *I*: incident monitoring light; *J*: reflected monitoring light). Adapted with permission from Ref.¹⁰⁰

Homogeneous distribution of the transient species (see Figure 3.6 (left)) occurs at larger laser fluxes in diluted samples with a high ground state extinction coefficient at the exciting wavelength to ensure a high conversion percentage of the ground to the excited state.⁹⁹ In this case the transient can be described using the Kubelka Munk approach¹⁰² which relates the observed reflectance R to the absorption coefficient K and the scattering coefficient S :

$$\frac{(1-R)^2}{2R} = \frac{K}{S} \quad (3.3)$$

as follows:

$$\Delta R_K = \frac{(1-R_x)^2}{2R_x} - \frac{(1-R_0)^2}{2R_0} = \frac{K_t}{S} \quad (3.4)$$

where R_0 and R_x represent the reflection before and after laser excitation and K_t the transient absorption. In the diffuse reflectance measurement the value of R can be determined if the incident analyzing light intensity I_0 is known. The later one can be calculated from the experimentally measured value of J using a powder with a known value of R .

According to the Kubelka-Munk approach the absorption coefficient exhibits a linear dependency on the concentration:

$$K = \varepsilon c \quad (3.5)$$

with ε being the extinction coefficient and c the concentration.

For relating the observed transient reflectance to the transient concentration c_T at any time after the flash the extinction coefficient of the ground state absorber ε_G and of the transient species ε_T should be considered:⁹⁹

$$\Delta R_K = \frac{K_T}{S} = \frac{2(\varepsilon_T - \varepsilon_G)c_T}{S} \quad (3.6)$$

However, it can be assumed that in the diffuse reflectance laser flash photolysis studies the exponential distribution of the excited states prevails (see Figure 3.6 (right)).¹⁰⁰ This is due to the fact that the experiments are mostly performed at such conditions at which the ratio of the number of absorber units to the number of the exciting photons is high, thus a low conversion percentage of the ground state to the transient state is expected. Here, equation 3.6 cannot be applied. For the description of the exponentially falling-off concentration the system can be divided into a series of “thin slices” for which the Kubelka-Munk function is valid. Numerical solutions for this approach predict that a linear relationship exists between the reflectance change ($1 - R_T^x$) and the total transient concentration at values of ($1 - R_T^x$) below 0.1.^{94, 103}

In the present work according to equation 3.2 the ΔJ value (%) has been used to describe the optical changes obtained in TiO₂ upon laser excitation. The absolute value of ΔJ has been attributed to the transient absorption as explained above.

4. Results

4.1 Effect of laser excitation on the physical and morphological properties of TiO₂

It has been observed that the illumination of all TiO₂ samples studied here (colloidal TiO₂ powders and bulk TiO₂ powders) by the intense laser pulses leads to colour changes from white to grey-blue. This effect was stable and thus no changes were observed under ambient condition during few months. Hence, for a better understanding of the processes occurring at the TiO₂ surface during the laser flash photolysis experiment it was important to characterize the samples before and after laser excitation. For this propose the Hombikat UV100 powder provided by Sachtleben has been analyzed by means of different spectroscopic methods presented below. To quantitatively and qualitatively understand the effect of the laser illumination the TiO₂ sample has been exposed to a higher laser intensity than that usually employed per pulse (10 x 50 mJ cm⁻² pulse⁻¹).

From the micrograph of laser illuminated TiO₂ surface shown in Figure 4.1 (left) the nonhomogeneous distribution of the colour centers can be seen. Some areas exhibit dark coloration, while the majority of the sample's surface areas remained white. The Raman spectra of different sample areas are presented in Figure 4.1 (right). When the analyzing beam is focused on a white area, the Raman spectrum shows only anatase peaks: 149, 200, 395.5, 513 and 636.5 cm⁻¹, which can be assigned to major modes of the anatase phase as *E_g*, *E_g*, *B_{1g}*, and superpositions of *A_{1g}* and *B_{1g}*, and *E_g*, respectively.¹⁰⁴⁻¹⁰⁷ The Raman spectrum of the dark areas exhibits additional peaks with maxima at 238, 447.5 and 610 cm⁻¹. These three bands can be attributed to the two-phonon scattering, *E_g*, and *A_{1g}* modes of the rutile phase, respectively.¹⁰⁵⁻¹⁰⁸ Moreover, the highest anatase peak at 149 cm⁻¹ has narrowed and shifted to 143.5 cm⁻¹. Probably, such alteration happened due to an increase in particle size¹⁰⁴, while the influence of the *B_{1g}* mode of the rutile phase with a maximum at 143 cm⁻¹ could be excluded for this interpretation because of its low line intensity¹⁰⁵⁻¹⁰⁷.

4. Results

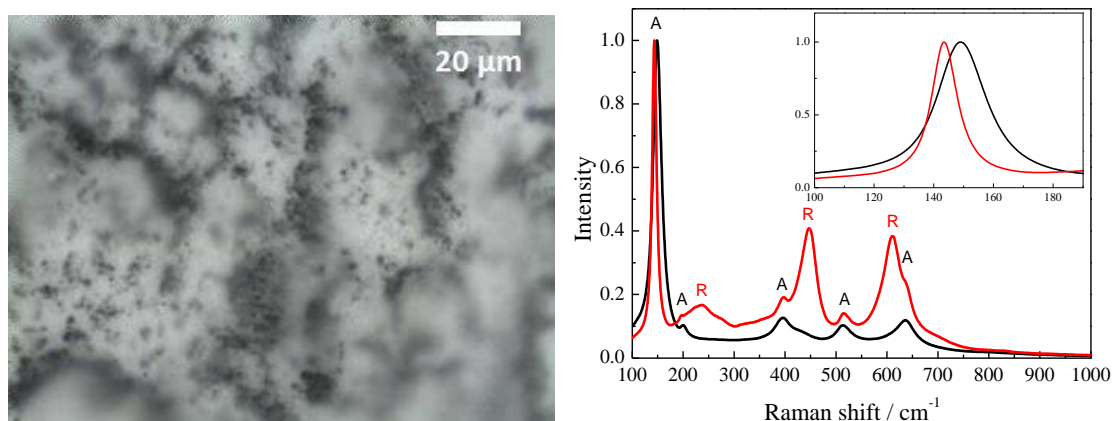


Figure 4.1: (left) Micrograph of an illuminated UV100 sample surface (50 x magnification). (right) Normalized Raman spectra of the illuminated UV100 sample: (black) white area and (red) dark area (exposed to the laser beam with a laser intensity of $10 \times 50 \text{ mJ cm}^{-2} \text{ pulse}^{-1}$).

However, the detected anatase to rutile phase transition does not explain the dark grey-blue coloration of the UV100 TiO_2 powder after the exposure to the laser. Figure 4.2 (left) presents the diffuse reflectance UV-vis spectra of untreated and illuminated TiO_2 powder, respectively. It can be seen that the absorption of the illuminated TiO_2 in the visible range increases continuously with the wavelength. This visible absorption indicates the presence of long-lived Ti^{3+} -species in the TiO_2 formed after the laser illumination.⁵ Apparently, these trap states are energetically distributed through the entire band gap exhibiting metallic-like character. Zhu *et al.*⁶⁴ reported a wide distribution of the trapped states for electrons within the entire bandgap (see Figure 2.6). The presence of the Ti^{3+} centers in the laser treated TiO_2 sample could furthermore be confirmed by means of electron paramagnetic resonance (EPR) spectroscopy. The initial uncolored sample does not show any EPR signal without UV-Vis illumination, while the laser illuminated sample exhibits an intense signal as shown in Figure 4.2 (right). A broad peak with $g_{\text{iso}} = 1.95$ with slight asymmetry can be assigned to Ti^{3+} centers in TiO_2 .^{109, 110} Most commonly, Ti^{3+} centers have axial symmetry and show specific signals which correspond to this anisotropy.¹⁰⁹⁻¹¹² In our case the axial signals are not resolved because the sample temperature is still too high for this and resolved signals could only be obtained with a helium cryostat.¹⁰⁹ Usually, similar EPR signals are assigned to Ti^{3+} in the rutile phase while anatase shows narrower Ti^{3+} signals with a higher g -value (1.98-1.99).¹¹⁰⁻¹¹² The formation of Ti^{3+} species in the laser-generated rutile phase could be confirmed by recording the EPR-spectra of the laser illuminated rutile phase, which exhibits the same EPR signal as laser illuminated anatase TiO_2 (see Figure 4.2 (right)). This also

corresponds to the fact that rutile can be reduced much more easily than anatase. Moreover, it should be noted that the Ti^{3+} centers detected here are stable in the presence of molecular oxygen as it has also been shown for Ti^{3+} centers obtained in black TiO_2 consisting anatase/rutile phases.¹¹³ Hence, both the UV-vis spectra and the EPR results reveal that upon the laser excitation anatase/rutile TiO_2 is formed exhibiting properties similar to those of black TiO_2 .

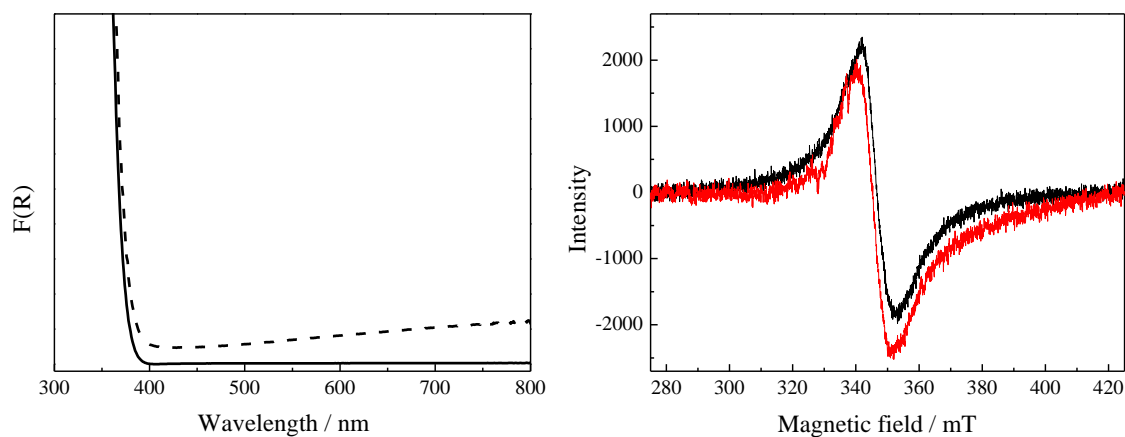


Figure 4.2: (left) UV-vis diffuse reflectance spectra of (solid) untreated and (dash) illuminated UV100. (right) EPR spectra measured at 77 K of (black) illuminated UV100 TiO_2 anatase and (red) illuminated R15 TiO_2 rutile (exposed to the laser beam with laser intensity: $10 \times 50 \text{ mJ cm}^{-2} \text{ pulse}^{-1}$).

4.2 Effect of laser intensity and energy on the transient absorption signals

The dependency of the decay kinetics on the excitation intensity is an important correlation to derive the rate law of the observed transient absorption decays. Upon variation of the excitation intensity the concentration of the photogenerated charge carriers changes and thus the kinetic features of the relaxation processes can be different.^{11, 82, 114, 115} For example, it has been shown that at low laser intensities the decay kinetics do not depend on the laser intensity, while at higher laser intensities, i.e., above $160 \text{ nJ pulse}^{-1}$, the decay rate increases as the laser intensity increases.³³ The processes observed at weak excitation conditions have been explained by the relaxation of the bound electron-hole pairs, called geminate recombination, while at higher laser intensities bimolecular second order bulk recombination occurs.

4. Results

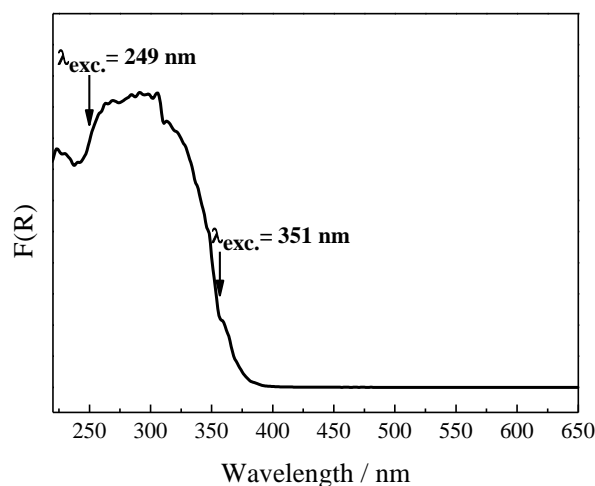


Figure 4.3: UV-vis diffuse reflectance spectrum of bulk anatase TiO₂ (UV100). Arrows indicate the excitation wavelengths employed in the transient absorption measurements.

The excitation energy can also influence the transient absorption properties of the photogenerated species. Figure 4.3 shows the diffuse reflectance spectra of the bulk anatase TiO₂ sample including arrows indicating the laser excitation wavelengths chosen in this work, i.e., 248 nm and 351 nm. At 351 nm the absorption is three times weaker than at 248 nm, thus at longer wavelengths the laser beam can penetrate more deeply into the powdered sample leading to a lower charge carrier density photogenerated per laser pulse in comparison to the excitation at 248 nm. According to the argument presented above, upon illumination with $\lambda_{\text{exc}} = 351$ nm a slower recombination is expected as compared with the 248 nm excitation provided that identical laser intensities or rather photon concentration per pulse are employed. Moreover, Tamaki *et al.*^{13, 14} have demonstrated by means of femtosecond transient absorption spectroscopy that the excitation with excess energy considerably exceeding the bandgap energy of the semiconductor can slow down the trapping process, since the electrons are excited into higher energy levels within the conduction band in comparison to the interband excitation employing 355 nm photons.

However, the above presented effect of laser energy and laser intensity has so far been mostly studied on transparent colloidal semiconductor suspensions or on transparent films made therefrom. The reaction dynamics of the charge carriers photogenerated in powdered samples, which are mostly applied in photocatalytic tests, have, however rarely been investigated. Moreover, for the design of new photocatalysts it is important to study the transient absorption properties of charge carriers photogenerated in different TiO₂ morphologies. Therefore, in the following chapter the reaction dynamics of charge

carriers photogenerated under inert atmosphere in colloidal anatase (powder), bulk anatase, and bulk rutile, will be presented.

4.2.1 Colloidal anatase TiO₂ powder

The transient absorption spectra and decay kinetics of the charge carriers formed upon laser illumination in dry colloidal TiO₂ particles have been studied by means of time-resolved diffuse reflectance spectroscopy. Herewith, the change in the diffusely reflected light ΔJ given in percentage rather than the transmitted light is detected. As already specified in chapter 3.2 the ΔJ value can be correlated to the transient absorption, thus for the presentation of the results obtained by the detection of the diffusely reflected light the latter term will be employed.

Figure 4.4 (left) presents the transient absorption signal recorded at 450 nm for N₂ saturated bare colloidal TiO₂ powder in the absence of any electron acceptor or donor at a laser intensity of 10 mJ cm⁻² pulse⁻¹. The chosen laser intensity is the lowest intensity at which evaluable transients produced in colloidal TiO₂ could be detected averaging only 2 laser pulses. As can be seen for the transient absorption signal shown in this figure, a strong increase in absorption is apparent immediately after the laser pulse, which decreases rapidly within the first ~0.3 μs, followed by a slower decay before reaching a long-lasting, nearly constant transient absorption with about 28 % (t = 17 μs) of the original intensity. This long-lived transient absorption is observed over the entire wavelength regime studied here, that is from 390 nm to 750 nm. Hence, for a better comparison of the initial decay behavior at different wavelengths, the plateau absorbance has been subtracted from the absorption decay, and the resulting difference has been normalized to the original intensity according to:

$$f_{\lambda}(t) = \frac{\Delta J_{\lambda}(t) - \Delta J_{\lambda}(t = 18\mu\text{s})}{\Delta J_{\lambda}^{\text{max}} - \Delta J_{\lambda}(t = 18\mu\text{s})} \quad (4.1)$$

The modified decay signals for the transients at 390 nm, 450 nm, 550 nm, and 650 nm are plotted in the inset of Figure 4.4 (left). Apparently, the decay kinetics do not depend on the wavelength of observation in the region between 390 nm and 750 nm and exhibit a characteristic life-time $t_{1/e}$ of around 0.5 μs after which the initial change in reflection ΔJ_{max} , that is, before the start of the linear decay, has decayed to $\Delta J_{\text{max}}/e$. The transient absorption spectrum of dry colloidal TiO₂ powder has already been measured by Bowman

4. Results

and co-workers^{69, 72} in the picosecond time scale, while Durrant *et al.*¹¹⁵ have studied the decay kinetics of trapped holes and electrons in opaque TiO₂ films prepared from colloidal TiO₂ by means of μ s-ms transient absorption spectroscopy. These authors have obtained slower decay kinetics with $t_{1/e}$ of 1 μ s, which can be explained by the fact that the measurements have been performed at much lower laser intensities (0.350 mJ cm⁻² pulse⁻¹).

The transient absorption spectra obtained at four selected times after the laser pulse are presented in Figure 4.4 (right). In the absence of any electron donor or acceptor broad and featureless transient absorption spectra are observed. During the first few microseconds after the laser pulse the signal intensity increases slightly with decreasing wavelength, while the transient spectrum taken 17 μ s after the laser pulse does not follow this trend, instead a shapeless spectrum is observed exhibiting similar intensity values over the entire wavelength region studied.

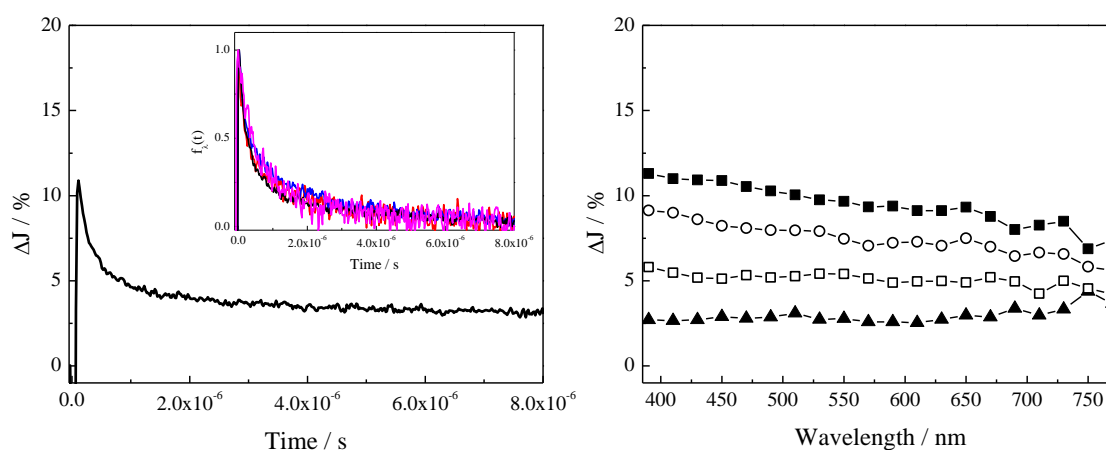


Figure 4.4: (left) Transient absorption signal observed at 450 nm upon laser excitation with $\lambda_{\text{exc}} = 351$ nm, inset: transient absorption signals normalized according to equation (4.1) observed at (pink) 390 nm, (black) 450 nm, (blue) 550 nm, and (red) 650 nm, respectively. (right) Transient absorption spectra observed (-■-) 0.109 μ s, (-○-) 0.229 μ s, (-□-) 0.8 μ s, and (-▲-) 17 μ s after the laser pulse. Experimental conditions: N₂-saturated colloidal TiO₂ powder, laser intensity: 10 mJ cm⁻² pulse⁻¹.

A threefold increase of the employed laser intensity leads to a 1.5 fold increase of the transient absorption signal at 450 nm as shown in Figure 4.5 (left). While during the first 0.15 μ s the decay kinetics remain the same as at lower excitation intensities, the following exponential decay accelerates, thus $\Delta J_{\text{max}}/e$ is reached already after 0.28 μ s. Moreover, the relative intensity of the long-lasting absorption decreases to 9 % in comparison to the values obtained at a laser intensity of 10 mJ cm⁻² pulse⁻¹. A similar decay behavior of the transient absorption signals is observed in the wavelength range

between 430 nm and 490 nm, while the decay of the transients measured at 390 nm, 410 nm, and above 490 nm remains the same as that found upon $10 \text{ mJ cm}^{-2} \text{ pulse}^{-1}$ excitation. The inset of Figure 4.5 (left) shows the decays of the transients at four different wavelengths (390 nm, 450 nm, 550 nm, and 650 nm) representing the different region of the spectra from 390 nm to 410 nm, from 430 nm to 490 nm, and from 510 nm to 590 nm to 750 nm.

The increase of the laser intensity has also a drastic effect on the feature of the transient absorption spectra. As seen in Figure 4.5 (right) the transient absorption intensity measured at $0.109 \mu\text{s}$ after the laser pulse in the wavelength region between 390 nm and 470 nm increased upon excitation with the higher laser intensity, while at wavelengths above 470 nm an unexpected decrease of the transient absorption intensities is detected. In general, a more pronounced increase of the transient absorption intensity upon decreasing the wavelengths is observed.

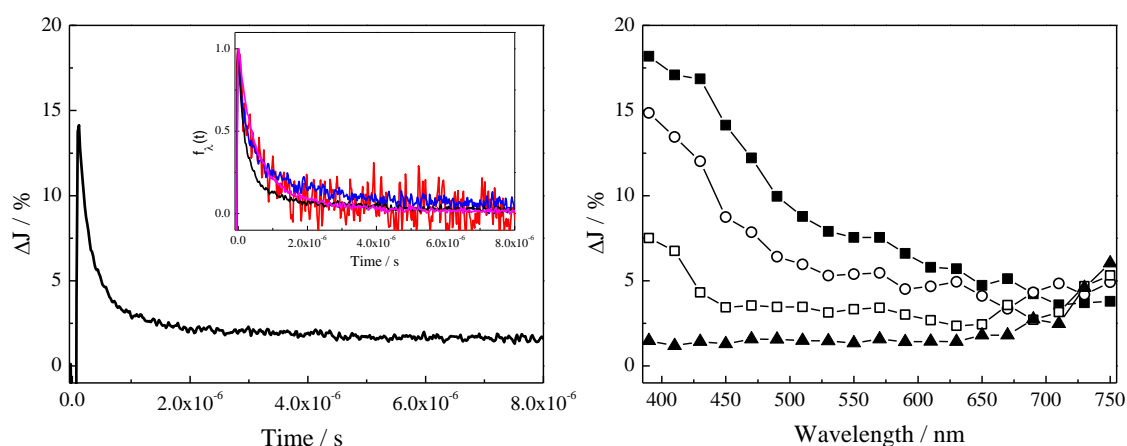


Figure 4.5: (left) Transient absorption signal observed at 450 nm upon laser excitation with $\lambda_{\text{exc}} = 351 \text{ nm}$, inset: transient absorption signals normalized according to equation (4.1) observed at (pink) 390 nm, (black) 450 nm, (blue) 550 nm, and (red) 650 nm, respectively. (right) Transient absorption spectra observed (-■-) $0.109 \mu\text{s}$, (-○-) $0.229 \mu\text{s}$, (-□-) $0.8 \mu\text{s}$, and (-▲-) $17 \mu\text{s}$ after the laser pulse. Experimental conditions: N_2 -saturated colloidal TiO_2 powder, laser intensity: $28 \text{ mJ cm}^{-2} \text{ pulse}^{-1}$.

The excitation of colloidal TiO_2 powder at 248 nm, that is with an energy considerably exceeding the bandgap energy of TiO_2 leads to the disappearance of the transient absorption at 450 nm (see Figure 4.6 (left)). The decay of the absorption signals observed in the wavelength range between 330 nm and 410 nm is found to be wavelength dependent with the decay kinetics accelerating at longer wavelengths as illustrated in the inset of Figure 4.6 (left). With $t_{1/e} = 0.15 \mu\text{s}$ the decay at 390 nm is faster in comparison to the transients observed upon illumination with 351 nm laser pulses, $t_{1/e}$ of the transient at

4. Results

370 nm is found to be 0.25 μs . In general, it should be noted here, that when the TiO_2 particles are excited with 248 nm laser pulses the density of charge carriers formed per particle increases drastically due to their lower penetration depth.

Figure 4.6 (right) shows the transient absorption spectra of the colloidal particles taken at different times after the 248 nm laser pulse. A transient absorption maximum located at 370 nm is detected. To the best of our knowledge, this maximum has been observed here for the first time for colloidal TiO_2 powder. In contrast to the transient absorption spectra measured upon excitation with 351 nm laser pulses no transient absorption signals are encountered at wavelengths longer than 410 nm. Moreover, the drastic increase of the laser intensity upon excitation at 248 nm leads to a decrease of the transient absorption in comparison to the results obtained when employing 351 nm laser light (see Figure 4.5).

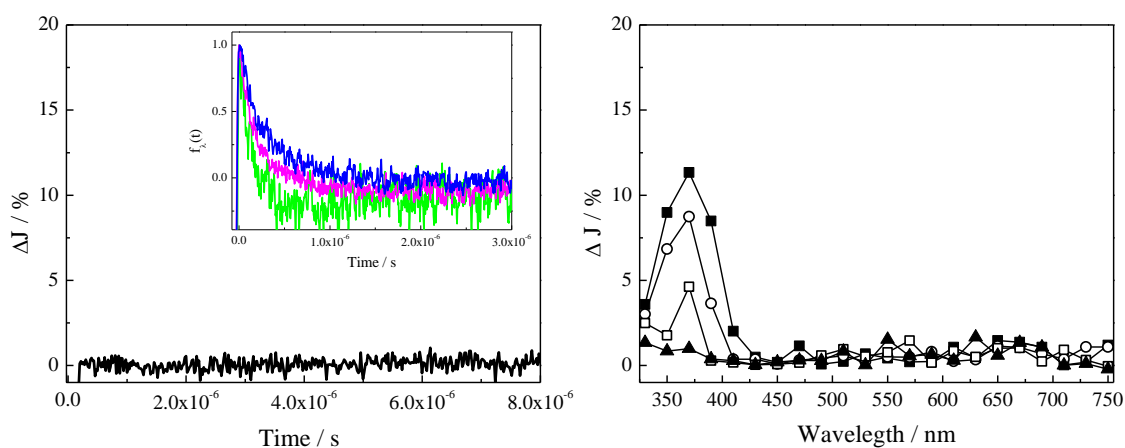


Figure 4.6: (left) Transient absorption signal observed at 450 nm upon laser excitation with $\lambda_{\text{exc}} = 248$ nm, inset: transient absorption signals normalized according to equation (4.1) observed at (blue) 370 nm (pink) 390 nm, and (green) 410 nm, respectively. (right) Transient absorption spectra observed (-■-) 0.109 μs , (-○-) 0.229 μs , (-□-) 0.8 μs , and (-▲-) 4 μs after the laser pulse. Experimental conditions: N_2 -saturated colloidal TiO_2 powder, laser intensity: $55 \text{ mJ cm}^{-2} \text{ pulse}^{-1}$.

4.2.2 Bulk anatase TiO_2 powder (Hombikat UV100)

As already mentioned above, most of the previous fundamental studies dealing with the reaction dynamics of the photogenerated charge carriers have been performed employing colloidal TiO_2 systems. By means of these studies the entire time regime of the photoinduced processes such as formation, trapping, recombination, and transfer of the charge carriers transfer was studied. Moreover, the trapped charge carriers could be spectroscopically characterized with the holes absorbing in the UV and the electrons in the visible spectral region. However, the life-time of the charge carriers in bulk

commercial powders has been rarely studied, although in many publications different obtained photocatalytic activities have been explained in terms of different charge carrier recombination kinetics, even though the latter have not been measured.

In this work the widely used commercial powder Hombikat UV100 from Sachtleben has been investigated using diffuse reflectance laser flash spectroscopy. This commercial powder has been chosen, on the one hand, because it is a well known photocatalyst exhibiting relatively high photocatalytic activity and, on the other hand, due to its relatively small particle size with crystalline diameters of 12 nm being thus comparable with the colloidal TiO_2 .

Figure 4.7 shows the transient absorption properties of the charge carriers photogenerated in UV100 (anatase TiO_2) under weak excitation conditions (i.e., $\lambda_{\text{exc}} = 351 \text{ nm}$ and $7 \text{ mJ cm}^{-2} \text{ pulse}^{-1}$) in the absence of any electron donor or acceptor. The transient signal observed at 450 nm decays linearly within the first $0.3 \mu\text{s}$ after the laser pulse followed by a slower exponential decay (see Figure 4.7 (left)). Similar to the colloidal particles the transient does not decay to zero and rather a long-lived component with 20 % of the initial absorption remains. As illustrated in the inset of Figure 4.7 (left) the transients observed at wavelengths higher than 410 nm decay faster with $t_{1/e}$ of $0.25 \mu\text{s}$ in comparison to the transients at shorter wavelengths ($t_{1/e} = 0.5 \mu\text{s}$).

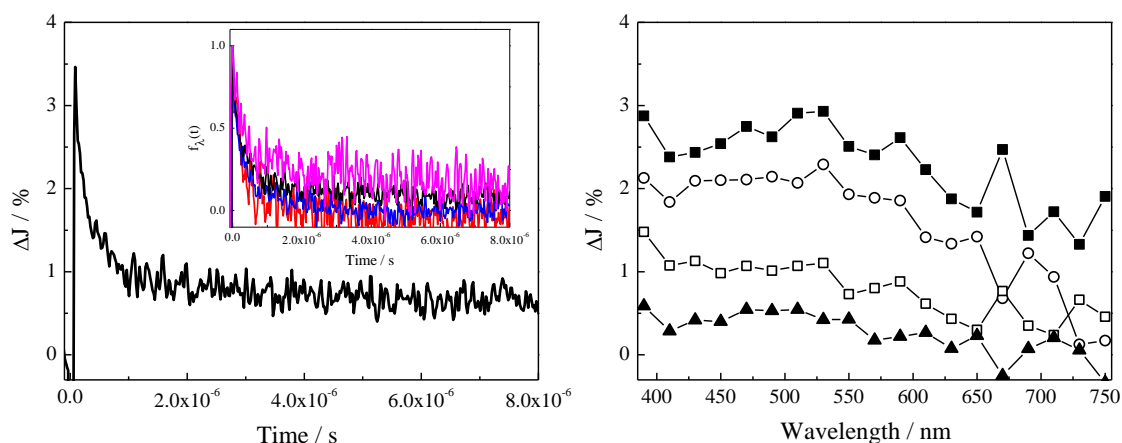


Figure 4.7: (left) Transient absorption signal observed at 450 nm upon laser excitation with $\lambda_{\text{exc}} = 351 \text{ nm}$, inset: transient absorption signals normalized according to equation (4.1) observed at (pink) 390 nm, (black) 450 nm, (blue) 550 nm, and (red) 650 nm, respectively. (right) Transient absorption spectra observed (-■-) 0.109 μs , (-○-) 0.229 μs , (-□-) 0.8 μs , and (-▲-) 17 μs after the laser pulse. Experimental conditions: N_2 -saturated UV100 powder, laser intensity: $7 \text{ mJ cm}^{-2} \text{ pulse}^{-1}$.

The transient absorption spectra measured in the wavelength range between 390 nm and 750 nm are very broad and featureless at all times after the laser pulse (see Figure 4.7

4. Results

(right)). Two relative maxima in the wavelength region studied are identified, one located around 520 nm and another one at 390 nm.

As shown in Figure 4.8, an increase of the laser intensity leads to higher initial transient absorption signals. Similar to the results obtained with the colloidal TiO₂ powder the intensity of the long-lived absorption relative to the initial absorption decreases from 20 % at 7 mJ cm⁻² pulse⁻¹ to 8 % at 23 mJ cm⁻² pulse⁻¹. The decay of the transient at 450 nm exhibits a similar trend as detected for the colloidal particles, namely, in the first 0.1 μs the decay does not change with the laser intensity, while the following exponential decrease of the absorption signal is accelerated, thus the characteristic time $t_{1/e}$ at which the transient absorption decays to 37 % of its initial value is found to be 0.18 μs (see Figure 4.8 (left)), the decay kinetics remain unchanged upon increasing the laser intensity both, at 390 nm and at wavelengths above 490 nm.

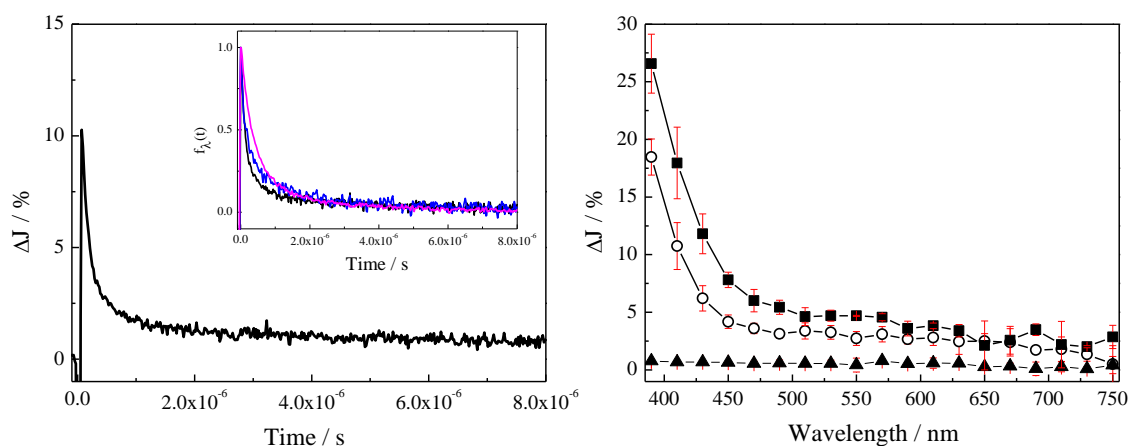


Figure 4.8: (left) Transient absorption signal observed at 450 nm upon laser excitation with $\lambda_{\text{exc}} = 351$ nm, inset: transient absorption signals normalized according to equation (4.1) observed at (pink) 390 nm, (black) 450 nm, and (blue) 550 nm, respectively. (right) Transient absorption spectra observed (-■-) 0.109 μs, (-○-) 0.229 μs, and (-▲-) 17 μs after the laser excitation. Experimental conditions: N₂-saturated UV100 powder, laser intensity: 23 mJ cm⁻² pulse⁻¹.

The transient absorption spectra obtained after different decay times are shown in Figure 4.8 (right). Similar to the colloidal particles a strong increase of the transient absorption intensity is detected between 390 nm and 450 nm at high excitation intensity. In the wavelength region between 450 nm and 750 nm the increase of the laser intensity causes only a slight increase of ΔJ of 6 %. The plot of the long-lived component measured 17 μs after the laser pulse as a function of the wavelength results in a featureless broad spectrum. In general, the shape of the transient absorption spectra does not change with the decay time.

Figure 4.9 (left) shows that the height of the initial transient absorption signals obtained at 390 nm, 450 nm, and 550 nm increases linearly with the laser intensity. The rise of the transient absorption is wavelength dependent, thus at 390 nm the slope is $1.7\% \text{ mJ}^{-1} \text{ cm}^2 \text{ pulse}^{-1}$, at 450 nm it is $0.6\% \text{ mJ}^{-1} \text{ cm}^2 \text{ pulse}^{-1}$, and at 550 nm it is $0.1\% \text{ mJ}^{-1} \text{ cm}^2 \text{ pulse}^{-1}$. The linear function does not go through the origin indicating either a slower increase of the transient absorption signal intensity with the laser intensity at weaker laser power or a nonlinear relationship of the transient absorption on the laser intensity at laser intensities lower than $7 \text{ mJ cm}^{-2} \text{ pulse}^{-1}$. However, the measurements performed in this work have all been conducted within the linear region, where neither nonlinear absorption nor nonlinear relaxation within the time resolution occurred. The long-lasting transient absorption detected $18 \mu\text{s}$ after the laser pulse exhibits almost no dependency on the laser intensity in the region between $6 \text{ mJ cm}^{-2} \text{ pulse}^{-1}$ and $23 \text{ mJ cm}^{-2} \text{ pulse}^{-1}$ (see Figure 4.9 (right), while at higher excitation intensities the long-lived transient absorption at 390 nm increases and it decreases at longer wavelengths.

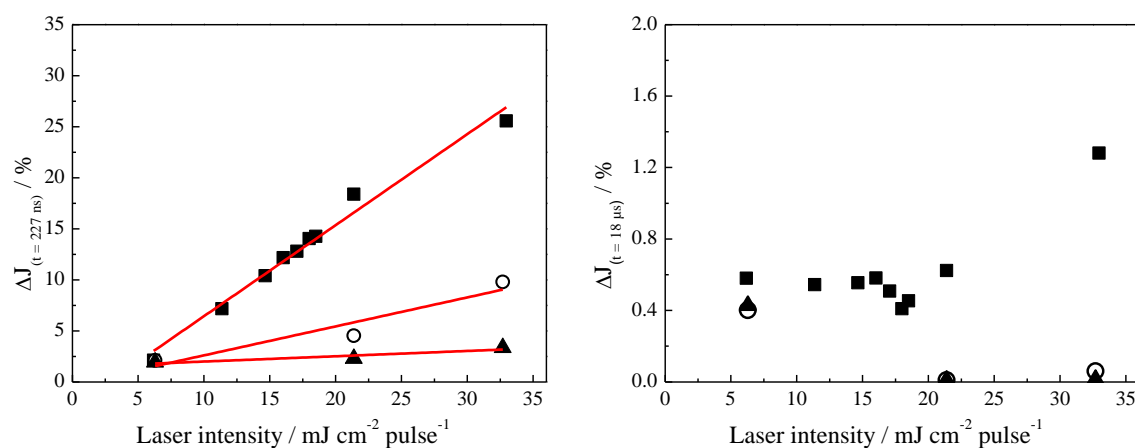


Figure 4.9: Height of the transient absorption signal as the function of the laser intensity observed at (■) 390 nm, (○) 450, and (▲) at 550 nm (left) 227 ns and (right) $18 \mu\text{s}$ after the laser excitation. Red lines present the linear fit. Experimental conditions: N_2 -saturated UV100 powder.

Similar to the observation made with the colloidal TiO_2 powder the excitation of bulk anatase UV100 with 248 nm laser pulses leads to a drastic decrease of the transient absorption at 450 nm as shown in Figure 4.10 (left). The decay kinetics are wavelength dependent and an acceleration of the decay is observed at longer wavelengths (see the inset of Figure 4.10 (left)). The transients at 350 nm and at 370 nm decay to $\Delta J_{\text{max}}/e$ within $0.7 \mu\text{s}$, while $t_{1/e}$ at 390 nm and at 410 nm is found to be $0.4 \mu\text{s}$ and $0.2 \mu\text{s}$,

4. Results

respectively. This characteristic decay time is smaller upon excitation at 248 nm in comparison to the excitation with laser pulses at 351 nm.

The transient absorption spectra measured at different times after the 248 nm laser pulse are shown together with the respective error bars in Figure 4.10 (right). Similar to colloidal TiO₂ powder a transient maximum is detected at 370 nm, which does not change with the decay time. The transient absorption at wavelengths higher than 410 nm decreases almost by a factor of 5 in comparison to the excitation at 351 nm (see Figure 4.8 (right)).

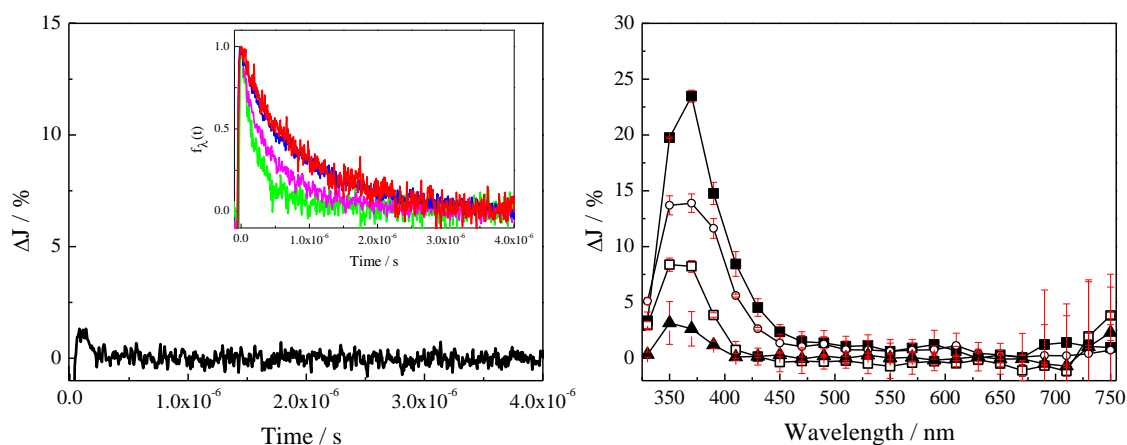


Figure 4.10: (left) Transient absorption signal observed at 450 nm upon laser excitation with $\lambda_{\text{exc}} = 248$ nm, inset: transient absorption signals normalized according to equation (4.1) observed at (red) 350 nm, (blue) 370 nm, (pink) 390 nm, and (green) 410 nm, respectively. (right) Transient absorption spectra observed (-■-) 0.109 μ s, (-○-) 0.229 μ s, (-□-) 0.8 μ s, and (-▲-) 4 μ s after the laser pulse. Experimental conditions: N₂-saturated UV100 powder, laser intensity: 52 mJ cm⁻² pulse⁻¹.

4.2.3 Bulk rutile TiO₂ powder (R15)

Rutile is one of the most extensively investigated TiO₂ modifications. It is usually reported that rutile exhibits lower photocatalytic activity when illuminated with light in the UV region in comparison to the anatase phase.¹¹⁶ However, it should be noted here, that for any meaningful comparison of different phases of TiO₂ other parameters such as crystallinity and particle size should be the same. Since, however, rutile is usually synthesized at higher temperatures than anatase the preparations of the former contain bigger particles. To enable a comparison of the reaction dynamics of the charge carriers photogenerated in different TiO₂ phases, the commercial rutile powder R15 has been chosen in the present work as it contains similar particle sizes ($d = 20$ nm) as bulk anatase TiO₂ UV100.

After excitation with a 351 nm laser pulse the bulk rutile TiO₂ R15 sample exhibits a sharp transient absorption increase at 450 nm, which initially decays almost linearly within 0.5 μ s followed by an exponential decay reaching a long-lived transient absorption with apparently 10 % of the initial value (see Figure 4.11 (left)). In comparison to the UV100 samples (see Figure 4.7) the photogenerated species absorbing at 450 nm exhibits a longer life-time with $t_{1/e}$ of 0.75 μ s. The transients detected at 390 nm, 410 nm, 450 nm, and 550 nm have been normalized according to equation 4.1, that is, the long-lived absorption measured at 45 μ s after the laser pulse has been subtracted. As seen from the inset of Figure 4.11 (left) the decay kinetics are different at different observation wavelengths, indeed, at 390 nm $t_{1/e}$ is found to be 3.6 μ s, at 410 nm $t_{1/e}$ is 2.4 μ s, while at wavelengths above 450 nm the decay occurs much faster with a $t_{1/e}$ of 0.4 μ s.

The transient absorption spectra exhibit already at low excitation intensity conditions, in contrast to the anatase sample presented above, high absorption intensities which increase exponentially with decreasing observation wavelengths. The transient absorption in the visible region, however, is very low. (see Figure 4.11 (right)). The shape of the transient absorption spectra does not change with the decay time.

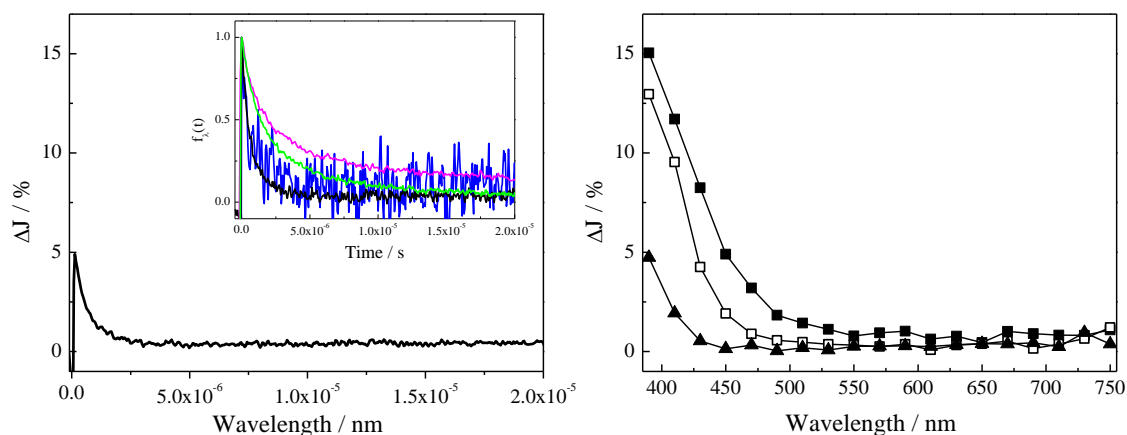


Figure 4.11: Transient absorption signal observed at 450 nm upon laser excitation with $\lambda_{\text{exc}} = 351$ nm, inset: transient absorption signals normalized according to equation (4.1) observed at (pink) 390 nm (black) 450 nm, and (blue) 550 nm, respectively. (right) Transient absorption spectra observed (—○—) 0.109 μ s, (—□—) 0.8 μ s, and (—▲—) 45 μ s after the laser pulse. Experimental conditions: N₂-saturated R15 powder, laser intensity: 7 mJ cm⁻² pulse⁻¹.

An increase in the laser intensity leads to a higher transient absorption signal at 450 nm, while the decay kinetics do not change. The ratio of the long-lived absorption to the initial absorption decreases to 5 % at higher laser intensity. The decay kinetics of the transients

4. Results

recorded at 390 nm, at 410 nm, and at 550 nm remain the same as those obtained at lower laser intensities (see inset of Figure 4.12 (left)).

The increase of the laser intensity leads to a shift of the transient absorption maximum from 390 nm to 410 nm indicating a saturation of the states absorbing at 390 nm (Figure 4.12 (right)). In general, the transient absorption increases with decreasing wavelength and the shape of the transient absorption spectrum does not depend on the decay time. In contrast to the results obtained with the anatase powder the initial transient absorption recorded for the rutile powder 0.229 μ s after the laser pulse lies below 5 % at wavelengths higher than 500 nm.

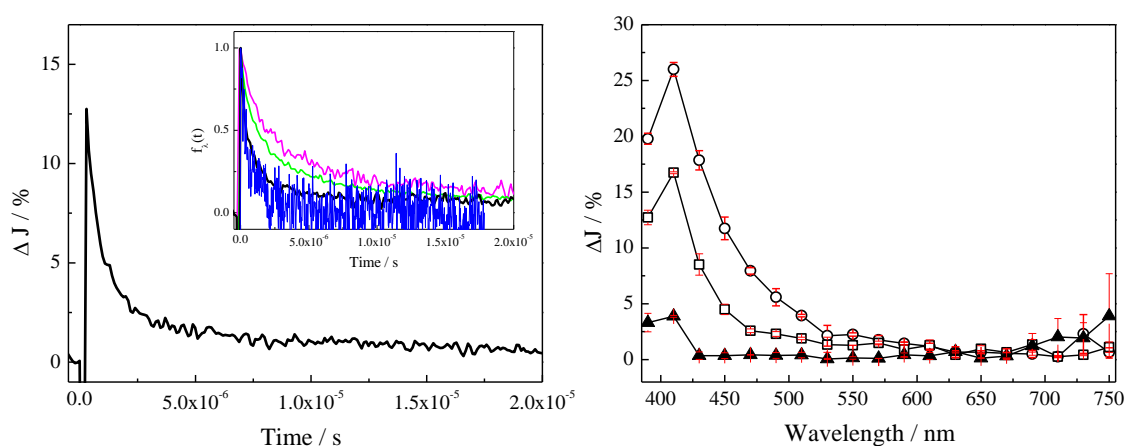


Figure 4.12: (left) Transient absorption signal observed at 450 nm upon laser excitation with $\lambda_{\text{exc}} = 351$ nm, inset: transient absorption signals normalized according to equation (4.1) observed at (pink) 390 nm, (green) 410 nm, (black) 450 nm, and (blue) 550 nm, respectively. (right) Transient absorption spectra observed (-○-) 0.229 μ s, (-□-) 0.8 μ s, and (-▲-) 45 μ s after the laser excitation. Experimental conditions: N_2 -saturated R15 powder, laser intensity: 30 $\text{mJ cm}^{-2} \text{pulse}^{-1}$.

A linear relationship is noted between the transient absorption signal intensity measured 227 ns after the laser pulse and the laser intensity as shown in Figure 4.13 (left) for transients at 390 nm, 450 nm, and at 550 nm. However, the linear dependency for the transient at 390 nm is only given at excitation intensities between 7 $\text{mJ cm}^{-2} \text{pulse}^{-1}$ and 16 $\text{mJ cm}^{-2} \text{pulse}^{-1}$, while with higher laser intensities no change in the initial transient absorption intensity is observed indicating a saturation of the rutile sample. Moreover, on contrast to UV100 the linear function crosses zero. The slope of the linear correlations is wavelength dependent and is found to be 2.1 % $\text{mJ}^{-1} \text{cm}^2 \text{pulse}$ at 390 nm, 0.85 % $\text{mJ}^{-1} \text{cm}^2 \text{pulse}$ at 450 nm, and 0.4 % $\text{mJ}^{-1} \text{cm}^2 \text{pulse}$ at 550 nm. In contrast to UV100 for R15 the long-lived absorption at 390 nm recorded 45 μ s after the laser pulse is proportional to

the laser pulse intensity, while at longer wavelengths there is no change of the signal height upon increasing the laser intensity (Figure 4.13 (right)).

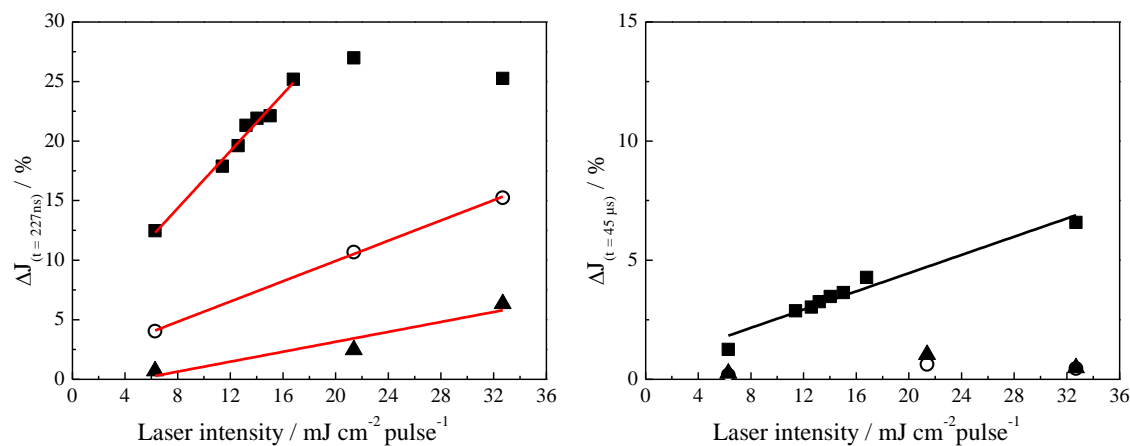


Figure 4.13: Height of the transient absorption signal as a function of the laser intensity observed at (■) 390 nm, (○) 450, and (▲) 550 nm (left) 227 ns and (right) 45 μ s after the laser excitation. Red lines present the linear fit. Experimental conditions: N_2 -saturated R15 powder.

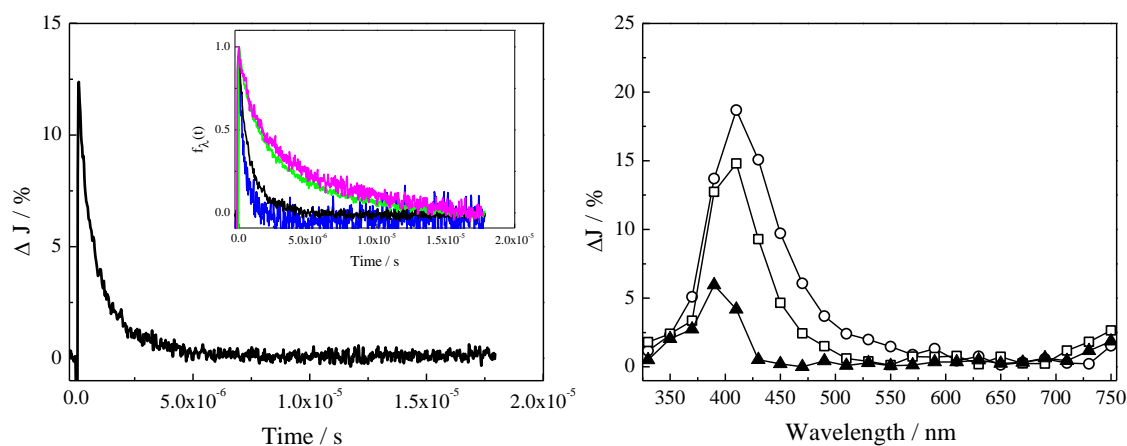


Figure 4.14: (left) Transient absorption signal observed at 450 nm upon laser excitation with $\lambda_{exc} = 248$ nm, inset: transient absorption signals normalized according to equation (4.1) observed at (pink) 390 nm, (green) 410 nm, (black) 450, and (blue) 510 nm, respectively. (right) Transient absorption spectra observed (○) 0.229 μ s, (□) 0.8 μ s, and (▲) 20 μ s after the laser pulse. Experimental conditions: N_2 -saturated R15 powder, laser intensity: 50 $mJ\ cm^{-2}\ pulse^{-1}$.

Upon excitation of R15 with 248 nm laser pulses a slightly faster transient decay is observed at 450 nm with $t_{1/e}$ of 0.7 μ s in comparison to the measurements with 351 nm excitation (see Figure 4.14 (left)). Similar to the anatase sample the decay kinetics depend on the wavelength and a faster decay is observed at longer wavelengths. The characteristic life-time $t_{1/e}$ at 390 nm is reduced from 3.6 μ s to 3 μ s in comparison to the

4. Results

measurements with excitation at 351 nm, while at 410 nm it decreases from 2.4 μs to 2.2 μs and at 510 nm from 0.45 μs to 0.4 μs .

As shown in Figure 4.14 (right) the excitation with laser energies considerably exceeding the bandgap energy causes time dependent shifts of the transient absorption spectra, thus 0.109 μs after the laser pulse a transient absorption maximum is detected at 410 nm, while 20 μs after the excitation the maximum shifts to 390 nm. The transient absorption at the wavelengths above 550 nm is similar to the measurements performed at $\lambda_{\text{exc}} = 351 \text{ nm}$.

4.3 Effect of electron donor and of acceptor on the transient absorption signals

From the above presented transient absorption spectra it is not possible to attribute the obtained transient absorption in the studied wavelength region to certain photogenerated transient species. Upon illumination of TiO_2 both electrons and holes are generated altering the optical properties of TiO_2 . Depending at which energy levels the charge carriers are located the transient absorption is known to vary.⁵ According to the literature dealing with this topic the transient absorption of trapped electrons and holes overlaps.¹¹ Under inert atmosphere both electrons and holes are present, thus to identify the region where the photogenerated electrons and holes absorb in the transient absorption spectra of TiO_2 , electron acceptors and donors have to be employed.

The following chapter will at first present the laser flash photolysis studies performed on transparent colloidal TiO_2 suspensions in the presence of platinum (Pt) as electron acceptor and polyvinyl alcohol as electron donor, respectively. These results will then be used as reference for the experiments with the colloidal TiO_2 powder, the bulk anatase UV100, and the bulk rutile R15.

4.3.1 Colloidal anatase TiO_2 suspensions

For the investigation of the dynamics of the photoinduced charge carriers in semiconductor nanoparticles the first laser flash experiments have been performed on transparent colloidal suspensions. The advantage of transparent nanoparticle suspensions is that the concentration of the colloidal particles exposed to the laser light is known

exactly, and that the amount of the photogenerated electron-hole pairs per particle can be readily adjusted.

Figure 4.15 (left) presents the transient absorption signal at 450 nm of an air saturated colloidal suspension of TiO₂ particles modified with Pt islands acting as electron scavenger. As shown in this figure a strong increase in absorption is apparent immediately after the laser pulse, which decreases rapidly during the first ~5 μs reaching a long-lasting, nearly constant transient absorption with about 28 % (t = 180 μs) of the initial intensity. This long-lived transient absorption is observed over the entire wavelength regime studied, although the residual intensity relative to the initial intensity is higher at shorter wavelengths with 40 % at 390 nm in comparison to the longer wavelengths, e.g., 20 % at 650 nm. Hence, in analogy to the treatment of the transient reflection signals obtained for the powder samples for a better comparison of the initial decay behavior at different wavelengths, the long-lived plateau absorbance is subtracted from the absorption decay, and the resulting difference is normalized to the original intensity according to:

$$f_{\lambda}(t) = \frac{\Delta A_{\lambda}(t) - \Delta A_{\lambda}(t = 180\mu\text{s})}{\Delta A_{\lambda}^{\text{max}} - \Delta A_{\lambda}(t = 180\mu\text{s})} \quad (4.2)$$

While, as can be seen from the inset in Figure 4.15 (left), the initial decay behavior for the different wavelengths is qualitatively similar, it is obvious from the precise analysis of the decay kinetics that the decay rate decreases with decreasing wavelength, thus at 390 nm and 400 nm the characteristic life-time after which the initial absorption ΔA_{max} decays to $\Delta A_{\text{max}}/e$ is found to be $t_{1/e} \sim 33\text{-}39 \mu\text{s}$, while in the wavelength range from 450 nm to 650 nm $\Delta A_{\text{max}}/e$ is reached after 15-20 μs. A similar decay rate dependency on the wavelength has been already reported.¹⁶

Figure 4.15 (right) presents the transient absorption spectra taken 227 ns and 17 μs after the laser pulse. Immediately 227 ns after the laser pulse a broad transient absorption spectrum with a maximum centered at 450 nm is observed, similar to the spectra previously reported.^{7, 11, 16} This maximum shifts towards shorter wavelengths during the decay of the transient signal. This transient absorption can be attributed to the trapped holes, since the electrons are transferred to the Pt islands. However, the broadness of the spectra (width at half maximum 200 nm for the initial spectrum) indicates either that the electrochemical environment of the photogenerated hole at the TiO₂ surface differs depending on its location thus shifting its absorption strongly into the *vis* range, or that

4. Results

not all photogenerated electrons have been transferred to Pt and part of the spectrum can be attributed to the trapped electrons. The latter is more likely, since the decay could not be completely suppressed in the presence of the Pt, although the trapped holes can recombine *via* the route expressed in equations 2.4 and 2.5. Moreover, according to the published TRMC results, Pt is found not to be sufficient to accept all electrons generated during the laser pulse.¹¹⁷

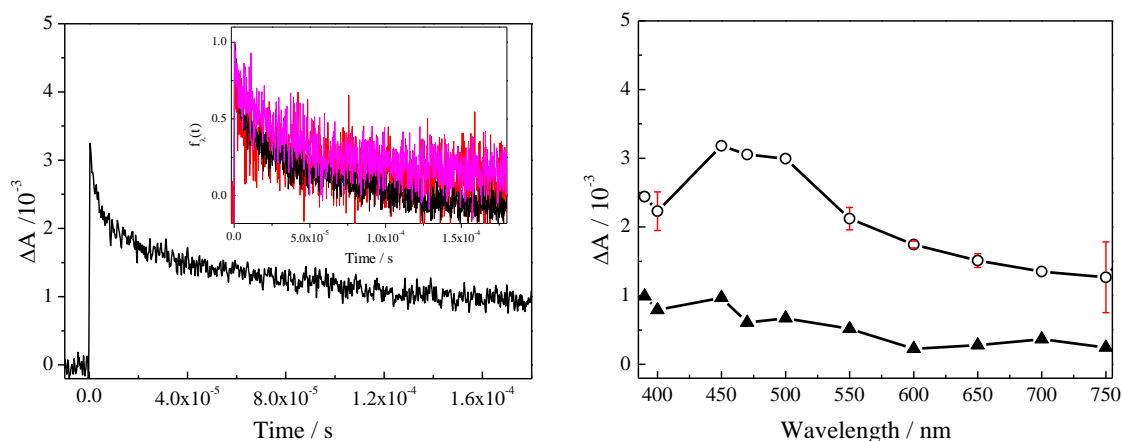


Figure 4.15: (left) Transient absorption signal observed at 450 nm upon laser excitation with $\lambda_{\text{exc}} = 351$ nm, inset: transient absorption signals normalized according to equation (4.2) observed at (pink) 390 nm (black) 450 nm, and (red) 650 nm, respectively. (right) Transient absorption spectrum observed (-■-) 227 ns and (-▲-) 150 μs after the laser excitation. Experimental conditions: $6.3 \cdot 10^{-3}$ M colloidal TiO_2 suspension containing 0.3 % wt deposited colloidal Pt, pH=3, laser intensity: $13.6 \text{ mJ cm}^{-2} \text{ pulse}^{-1}$.

To observe only the trapped electrons in TiO_2 different alcohols are frequently applied, which can react with the holes.⁸⁴ An example reaction of the holes with methanol is given below:



The formed α -hydroxy methyl radical can inject an electron into the conduction band resulting in formation of two electrons following the absorption of only one photon (this is well known as the so-called current doubling effect):



Figure 4.16 (left) shows the transient absorption vs. time signal obtained at 650 nm for N_2 -saturated TiO_2 -suspensions in the presence of an electron donor such as polyvinyl alcohol. This long chain alcohol has been chosen for its additional property acting as a

stabilizer of the TiO₂ colloid. A rapid decay lasting only a few ns followed by a long-lived absorption is observed. A similar decay behavior is observed for the entire studied wavelength range studied. It has been reported that 80 % of the holes can be scavenged by the alcohol within 1 ns.⁸⁴ Since Ti³⁺ centers formed by the trapping of the electrons have no other chance than to recombine with the holes, this initial rapid decay can be related to the reaction of the trapped holes with alcohol, as it has been suggested by Yoshihara *et al.*¹¹ as an explanation for such a decay behavior.

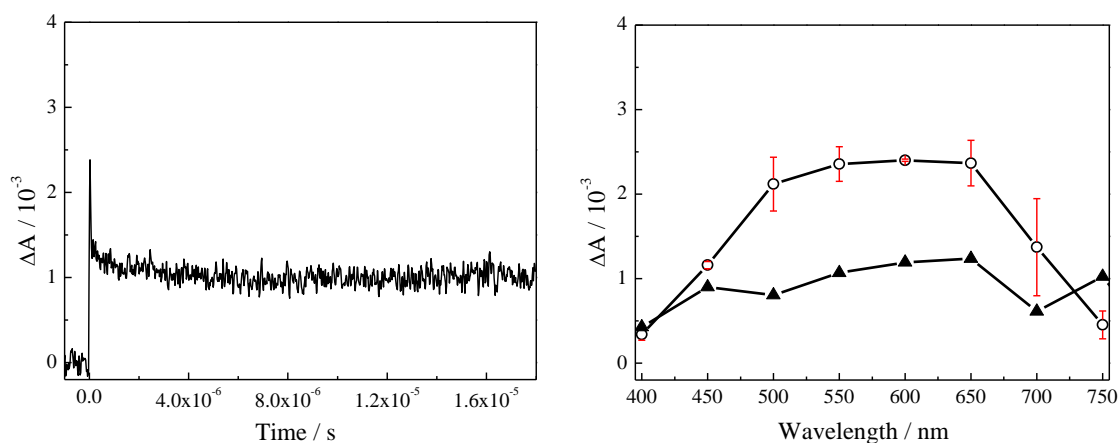


Figure 4.16: (left) Transient absorption signal observed at 650 nm upon laser excitation with $\lambda_{\text{exc}} = 351$ nm. (right) Transient absorption spectra observed (-o-) 269 ns and (-▲-) 18 μ s after the laser excitation. Experimental conditions: $6.3 \cdot 10^{-3}$ M colloidal TiO₂ suspension containing $5 \cdot 10^{-3}$ M PVA, pH=3, laser intensity: $8 \text{ mJ cm}^{-2} \text{ pulse}^{-1}$.

The transient absorption spectra measured 269 ns and 18 μ s after the laser pulse in the presence of polyvinyl alcohol are shifted towards longer wavelengths with a maximum at 630 nm in comparison to the transient absorption spectrum observed in the presence of Pt (see Figure 4.15 (right)). Again a very broad transient absorption band (width at half maximum 250 nm for the spectrum measured 269 ns after the laser pulse is obtained, the position and the shape of which do not change with the time. The broadness of these spectra is most probably related to the different trapping sites for the electrons in TiO₂ as already mentioned in chapter 2.1.

4.3.2 Colloidal anatase TiO₂ powder

For the identification of the transient absorption regions of the trapped electrons and of the trapped holes, respectively, in colloidal TiO₂ powder an electron acceptor such as molecular oxygen has been introduced into the powder. It has been reported that

4. Results

molecular oxygen reacts with the photogenerated electrons trapped in TiO_2 resulting in the formation of peroxy radical anions (see Figure 2.4 eqs. 11 and 12).^{111, 118} Figure 4.17 (left) shows the transient absorption signals recorded in this system at 450 nm. In the presence of O_2 the decay kinetics and the absorption intensity of the transient at 450 nm remains unchanged in comparison to the measurements under N_2 -atmosphere (see Figure 4.4 (left)). Moreover, the decay kinetics obtained in oxygen-atmosphere at other wavelengths do not differ from the transient decays recorded in the presence of nitrogen (see inset Figure 4.17 (left)). This indicates that the transfer of the trapped electrons to the adsorbed oxygen molecules cannot compete with the recombination process, although reported electron transfer times have been found to be within <100 ns.¹¹ In analogy to the transient decays in the presence of N_2 , the decay behavior in O_2 atmosphere does also not depend on the analyzing wavelengths, as can be seen in the inset of Figure 4.17 (left). The transient absorption spectra measured at different times after the laser pulse (shown in Figure 4.17 (right)) do not change with the decay time.

The transient spectrum observed 8 μs after the laser pulse exhibits lower intensities at wavelengths above 500 nm in comparison to the transient spectra obtained in nitrogen atmosphere (Figure 4.4 (right)). According to these changes observed in the presence of the electron acceptor O_2 the wavelength region from 500 nm to 750 nm can be attributed to the transient absorption of the trapped electrons, while the transient absorption at lower wavelengths belongs to the trapped holes.

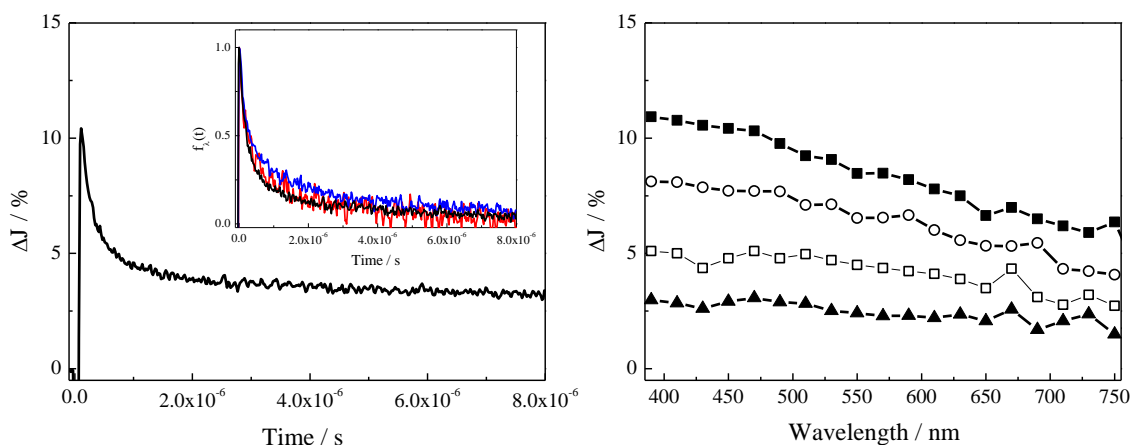


Figure 4.17: (left) Transient absorption signal observed at 450 nm upon laser excitation with $\lambda_{\text{exc}} = 351$ nm, inset: transient absorption signals normalized according to equation (4.1) observed at (black) 450 nm, (blue) 550 nm, and (red) 650 nm, respectively. (right) Transient absorption spectra observed (-■-) 0.109 μs , (-○-) 0.229 μs , (-□-) 0.8 μs , and (-▲-) 17 μs after the laser pulse. Experimental conditions: O_2 -saturated colloidal TiO_2 powder, laser intensity: $10 \text{ mJ cm}^{-2} \text{ pulse}^{-1}$.

In contrast to the slight effect of molecular oxygen on the transient absorption features of the colloidal TiO₂ powder, drastic changes are observed in the presence of electron donors such as methanol. After nitrogen saturated methanol has been added to the nitrogen saturated powder a build-up of the transient absorption at 650 nm is observed indicating an accumulation of trapped electrons as Ti³⁺ species in the system (Figure 4.18 (left)). These photogenerated trapped electrons remain in the TiO₂ particles for more than 1 s. As mentioned above the photogenerated holes undergo a fast reaction with the adsorbed methanol molecules (equation 4.3) thus preventing their recombination with the photogenerated electrons. Since the electrons have no other chance to react, they remain in the TiO₂ particles leading to the blue coloration of the powder.

The described build-up of the transient absorption is observed in the entire studied wavelength range from 410 nm to 800 nm, as examples the transients at 450 nm, 550 nm, and 650 nm are shown in the inset of Figure 4.18 (left). The reaction of the trapped holes with methanol apparently happens within the duration of the laser pulses since it no absorption build-up could be detected in the available time resolution of a few hundred nanoseconds. The observed two step build-up of the transients can be explained by the initial formation of Ti³⁺ centers during the laser pulse followed by the electron injection of the α -hydroxyalkyl radicals $\cdot\text{CH}_2\text{OH}$ into the conduction band according to:



In the presence of methanol the transient absorption shown in Figure 4.18 (right) increases with increasing wavelengths until a maximum around 700 nm is reached followed by a slight decrease of the height of the transient absorption in near IR. The appearance of the transient absorption maximum indicates that the electrons are localized at certain trapping states. It should be noted here that the contribution of the trapped electrons to the transient absorption at wavelengths below 500 nm is very high. However, the above proposed assignment of absorption wavelengths to the trapped holes and electrons could be confirmed using methanol as the electron donor.

4. Results

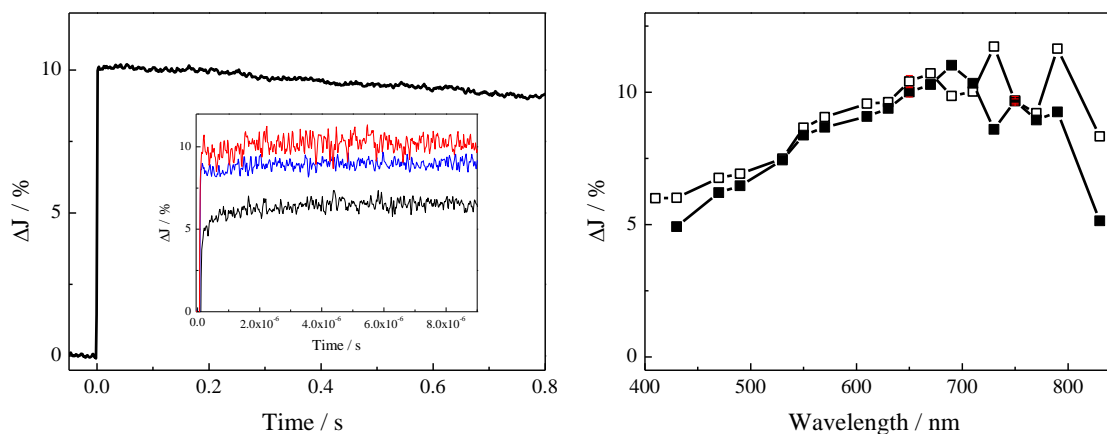


Figure 4.18: (left) Transient absorption signal observed at 650 nm upon laser excitation with $\lambda_{\text{exc}} = 351$ nm, inset: transient absorption signals observed at (black) 450 nm, (blue) 550 nm, and (red) 650 nm, respectively. (right) Transient absorption spectra observed (-■-) 0.269 μs and (-□-) 17 μs after the laser excitation. Experimental conditions: N_2 -saturated colloidal TiO_2 powder in the presence of $4 \cdot 10^{-3}$ mol/g CH_3OH , laser intensity: $10 \text{ mJ cm}^{-2} \text{ pulse}^{-1}$.

4.3.3 Bulk anatase TiO_2 powder (UV100)

For the identification of the trapped holes and electrons in the commercial TiO_2 powder Hombikat UV100 the transient absorption behavior has been measured in the presence of selected electron acceptors and donors. The transient spectra of the O_2 -saturated powder showed only minor differences in comparison to the transient absorption signals observed in inert atmosphere N_2 , only a slight decrease of the signal height is detected in the wavelength range from 450 nm to 750 nm (see 8. Appendix) Therefore, another electron acceptor, that is Pt has been used. As shown in Figure 4.19 (left) a faster decay is observed at 450 nm exhibiting $t_{1/e} = 0.18 \mu\text{s}$ with, however, a similar signal intensity in comparison to the bare UV100 of around 10 %. The addition of Pt, leads to the disappearance of the transients at wavelengths above 500 nm and to a deceleration of the decay kinetics in the wavelength range below 430 nm. The inset of Figure 4.19 (left) shows a much slower decay of the transient at 390 nm with $t_{1/e} = 0.8 \mu\text{s}$ in comparison to the decay at 450 nm.

The shape of the transient absorption spectra does not change in the presence of this electron acceptor, moreover, the absorption close to the UV region remains unchanged, while a strong decrease of the signal height in the visible region is observed (see Figure 4.19 (right)).

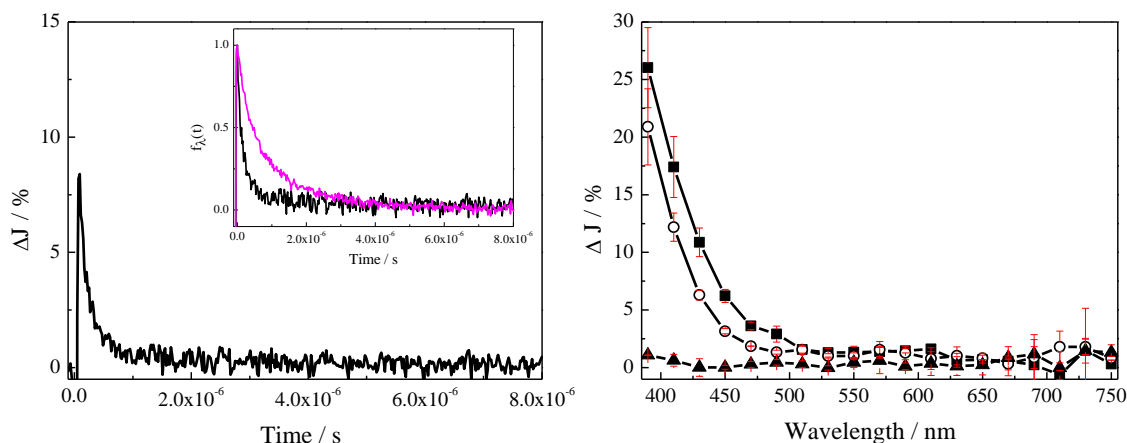


Figure 4.19: (left) Transient absorption signal observed at 450 nm upon laser excitation with $\lambda_{\text{exc}} = 351$ nm, inset: transient absorption signals normalized according to equation (4.1) observed at (pink) 390 nm, and (black) 450 nm. (right) Transient absorption spectra observed (-■-) 0.109 μs , (\circ) 0.229 μs , and (-▲-) 17 μs after the laser excitation. Experimental conditions: UV100 powder modified with 2 % wt Pt, laser intensity: $20 \text{ mJ cm}^{-2} \text{ pulse}^{-1}$.

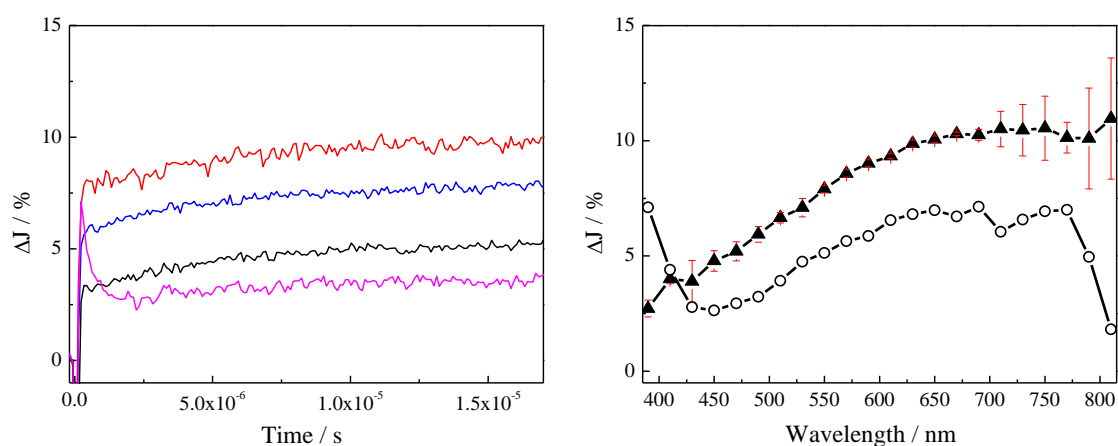


Figure 4.20: (left) Transient absorption signals observed at (pink) 390 nm, (black) 450 nm, (blue) 550 nm, and (red) 650 nm, respectively, upon laser excitation with $\lambda_{\text{exc}} = 351$ nm. (right) Transient absorption spectra observed (\circ) 0.229 μs and (-▲-) 17 μs after the laser excitation. Experimental conditions: N_2 -saturated UV100 powder in the presence of $4 \cdot 10^{-3} \text{ mol/g CH}_3\text{OH}$, laser intensity: $20 \text{ mJ cm}^{-2} \text{ pulse}^{-1}$.

The intensity of the transient absorption at 390 nm decreases after the addition of an electron donor such a methanol (see Figure 4.20 (left)). Moreover, the transient absorbing at 390 nm decays within a few microseconds until a plateau at 50 % of the initial intensity is reached. The initial decay can be related to the reaction of methanol with the trapped holes, while the long-lived absorption represents more deeply trapped electrons. The transients at higher wavelengths show a build-up similar to the transients observed for the colloidal particles. Figure 4.20 (right) presents the transient absorption spectra measured 229 ns and 17 μs after the laser pulse. The former shows two transient absorption maxima

4. Results

at 390 nm and around 700 nm with similar intensities, while 17 μs after the laser pulse the transient absorption continuously increases with increasing wavelength until 700 nm and then remains unchanged.

4.3.4 Bulk rutile TiO_2 powder (R15)

The R15 rutile powder has been modified with Pt to observe the transient absorption of the trapped holes assuming that the electrons are transferred to the metal islands. Figure 4.21 (left) demonstrates that the presence of the Pt islands leads to the deceleration of the decay at 390 nm with $t_{1/e}$ being 6 μs as compared with $t_{1/e} = 3.6 \mu\text{s}$ in absence of Pt, while the decay time observed at longer wavelengths is comparable to that of bare R15 10 % of the initial intensity of the transient absorption remains 80 μs after the laser pulse. The transient absorption spectra do not change after the modification with Pt indicating that the transient absorption observed in the wavelength range below 500 nm can be attributed to the trapped holes.

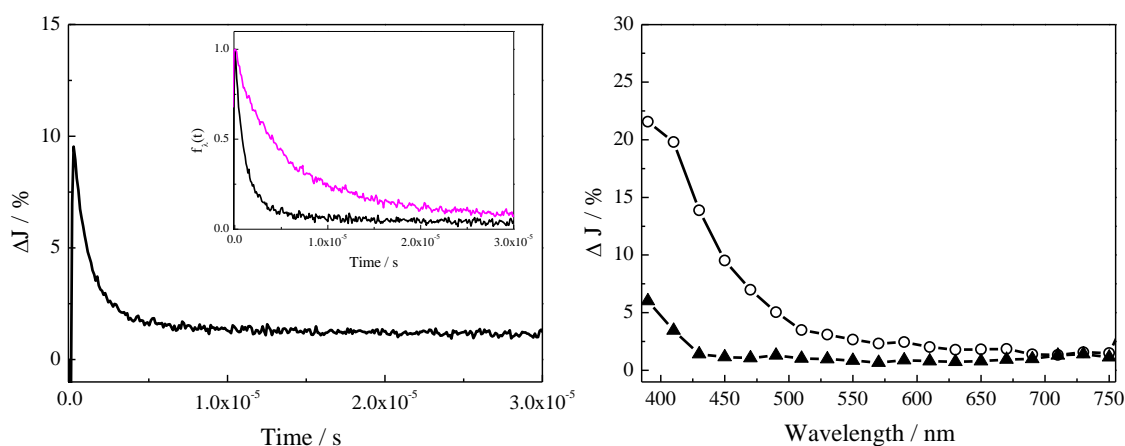


Figure 4.21: (left) Transient absorption signal observed at 450 nm upon laser excitation with $\lambda_{\text{exc}} = 351 \text{ nm}$, respectively, inset: transient absorption signals normalized according to equation (4.1) observed at (pink) 390 nm, and (black) 450 nm. (right) Transient absorption spectra observed (-o-) 0.229 μs and (- \blacktriangle -) 17 μs after the laser excitation. Experimental conditions: N_2 -saturated R15 powder, laser intensity: $16 \text{ mJ cm}^{-2} \text{ pulse}^{-1}$.

The addition of methanol to R15 leads to transient absorption signals involving two decay processes as shown in Figure 4.22 (left). The transient absorption observed over the whole studied wavelength range can be described by an initial rapid decay within 0.3 μs followed by a 1 μs long build-up of the transient absorption and by a final decay within 10 μs to a long-lasting absorption amounting to 60 % of the initial signal intensity. The observed decay processes indicate that in the presence of methanol after the excitation

two different species are formed at different times after the laser pulse. Moreover, the first decay overlaps with the subsequent build-up, however, it can be assumed that the second transient species is formed after the first one has reacted.

The transient absorption spectra measured at the two maxima and at the two minima are shown in Figure 4.22 (right). Similar to the anatase sample the transient absorption recorded at the first maximum after the laser pulse increases with the wavelength until a plateau region above 700 nm is reached. For the next maximum the transient absorption increases continuously with the wavelength. At the two minima, namely at 0.454 μs and at 17 μs , respectively, after the laser pulse, the transient absorption increases continuously until 750 nm.

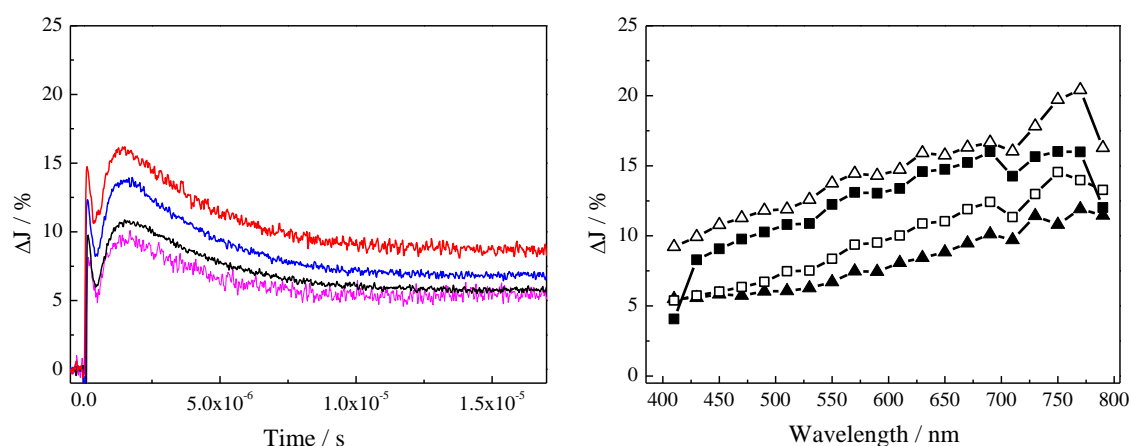


Figure 4.22: (left) Transient absorption signals observed at (pink) 390 nm, (black) 450 nm, (blue) 550 nm, and (red) 650 nm, respectively, upon laser excitation with $\lambda_{\text{exc}} = 351$ nm. (right) Transient absorption spectra observed (-■-) 0.109 μs , (-□-) 0.454 μs , (-Δ-) 1.6 μs , and (-▲-) 17 μs after the laser excitation. Experimental conditions: N_2 -saturated R15 powder in the presence of $4 \cdot 10^{-3}$ mol/g CH_3OH , laser intensity: $16 \text{ mJ cm}^{-2} \text{ pulse}^{-1}$.

4.4 Dependency of the transient absorption signals on the particle size

Crystallite size and crystallinity have been recognized as important parameters that influence the photocatalytic performance of semiconductor nanoparticles.¹¹⁹ It has been shown that the bigger the particle the higher is the photocatalytic activity of TiO_2 anatase, while the crystallinity exhibits no effect.^{120, 121} However, the effect of the particle size on the recombination kinetics of the photogenerated charge carriers in TiO_2 has rarely been studied. For example, Serpone *et al.*¹²² have observed for colloidal TiO_2 sols with mean particle diameters of 2.1, 13.3, and 26.7 nm that the transient absorption decay for the 2.1 nm sol is a simple first-order process, while for the bigger particles the transient

4. Results

absorption follows second order biphasic kinetics. In general, they reported a deceleration of the decay upon increasing the particle size. This example clearly shows that the particle size does not only effect the life-time of the photogenerated charge carriers, but also influences their recombination route.

In the following chapter the results obtained with the anatase and the rutile TiO₂ phases exhibiting different particle sizes and evidently different crystallinity will be presented.

4.4.1 Bulk anatase TiO₂ powder

Six commercially available TiO₂ anatase samples have been chosen to study the effect of the particle size and the degree of crystallinity on the recombination dynamics of the charge carriers: PC10, PC50, PC100, PC105, PC500, and S230. The powders are well known, have been well characterized, and have been tested regarding their photocatalytic activities by Pichat *et al.*¹²³⁻¹²⁵ These TiO₂ powders are all prepared *via* the hydrolysis of TiOSO₄, though the calcination time is varied. Figure 4.23 presents the crystallite size and the crystallinity of these TiO₂ powders. The determination of these parameters were performed by means of XRD-Spectroscopy as described in chapter 3. Upon increasing the calcination time, as expected, both the crystallite size and the crystallinity increase. The crystalline portion of the TiO₂ samples with particle sizes of 7 nm (S230), 10 nm (PC500), and 12 nm (UV100) lies between 66-70 %, while for bigger particles only 10 % of the material is amorphous.

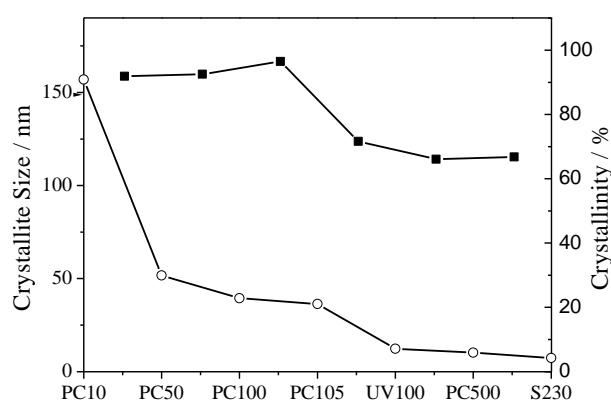


Figure 4.23: Crystallite size (particle diameter) and the crystallinity of the commercial TiO₂ anatase powders used in the present study.

Figure 4.24 shows the transients absorption signals recorded at 390 nm and at 450 nm for the different TiO₂ samples upon excitation with a 351 nm laser pulse. It is obvious that

the decay behavior depends on the different anatase samples with a deceleration of the decay occurring upon increasing particle size and increasing crystallinity. The transient absorption intensity at 390 nm decreases one half of its initial value for PC500 within 0.3 μs , while for PC10 $\Delta J/2$ is reached only after 6 μs . For the transients absorption at 450 nm faster decay times are generally recorded, thus $\Delta J/2$ for PC500 is reached after 0.15 μs and for PC10 after 1 μs . Moreover, by comparing the transients at 390 nm it is obvious that the long-lived absorption component is higher for the bigger particles.

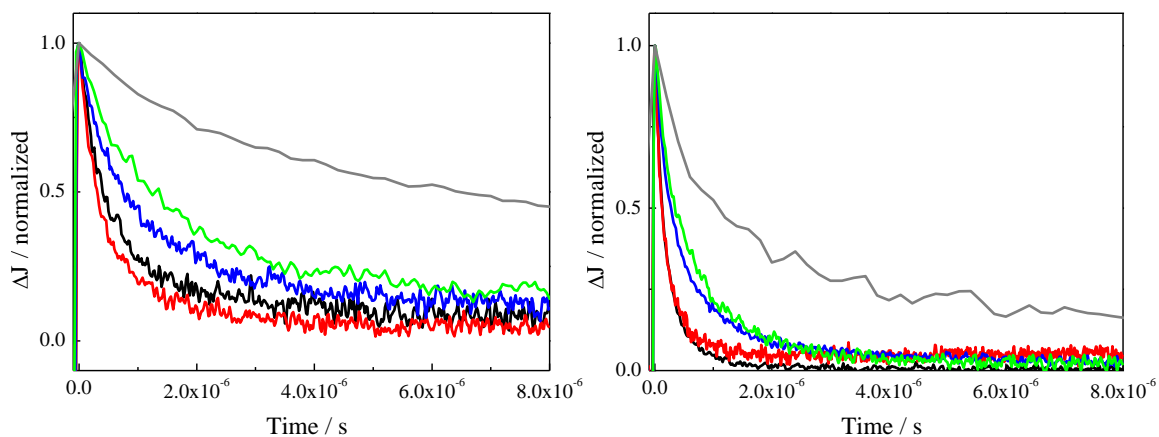


Figure 4.24 Normalized transient absorption signals observed at (left) 390 nm and (right) 450 nm of the charge carriers photogenerated in (black) S230, (red) PC500, (blue) PC105, (green) PC50, and in (grey) PC10. Experimental conditions: N₂ saturated TiO₂ powders, $\lambda_{\text{exc}} = 351 \text{ nm}$, laser intensity: $30 \text{ mJ cm}^{-2} \text{ pulse}^{-1}$.

The transient absorption spectra recorded 0.228 μs and 4.8 μs after the laser pulse for the anatase samples with different particle sizes are shown in Figure 4.25. The charge carriers photogenerated in the bigger particles exhibit a higher transient absorption 0.228 μs after the laser pulse in comparison to the smaller particles, although for all TiO₂ samples the highest transient absorption within the studied wavelength range has been detected at 390 nm. The transient absorption at 390 nm recorded 4.8 μs after the laser pulse increases upon increasing the particle size.

4. Results

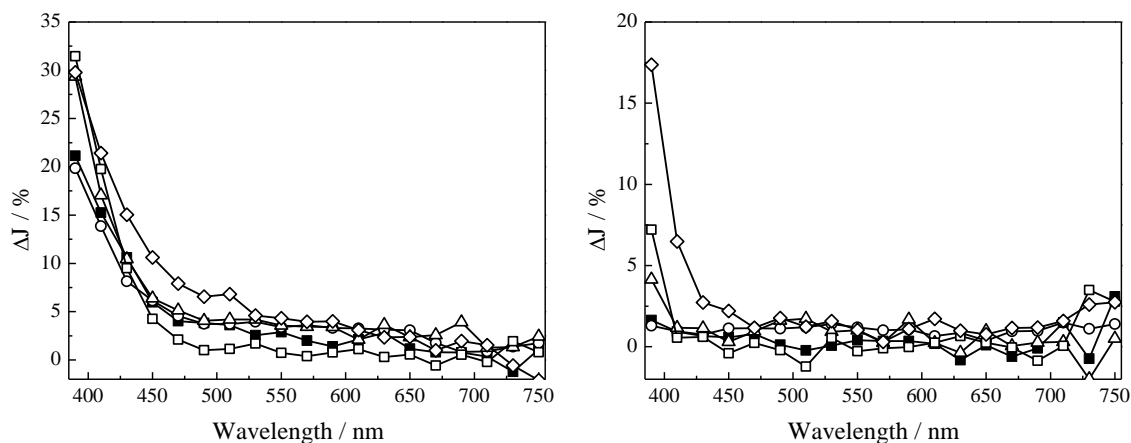


Figure 4.25: Transient absorption spectra observed (left) 0.228 μs and (right) 4.8 μs after the laser pulse of the charge carriers photogenerated in (■) S230, (○) PC500, (△) PC105, (□) PC50, and in (◇) PC10. Experimental conditions: N_2 saturated TiO_2 powders, $\lambda_{\text{exc}} = 351 \text{ nm}$, laser intensity: $30 \text{ mJ cm}^{-2} \text{ pulse}^{-1}$.

4.4.2 Bulk rutile TiO_2 powder

The effect of particle size on the recombination kinetics has also been investigated for rutile samples. Herewith, three commercially available TiO_2 powders exhibiting different crystallite sizes have been chosen. Similar to the anatase materials presented above the samples were provided by Millennium Performance Chemicals where they have been prepared *via* the oxidation of TiCl_4 . The characterization of the samples has already been performed by Cecilia Mendive.¹²⁶ The TiO_2 material R15 exhibits a crystallite size of 20 nm, R25 of 27 nm and R35 of 36 nm.

Figure 4.26 presents the transient absorption signals measured at 390 nm and at 410 nm for the three rutile samples. The decay of the transients at 390 nm slows down upon increasing the particle size from 20 to 27 nm, while a further increase of the particle size has no influence on the decay time. Similar to the experiments performed at different laser intensities, also here a saturation is observed. In contrast to the measurements at 390 nm, the decay of the transients at 410 nm decelerates continuously with an increase of the particle size. $\Delta J/2$ for R15 is reached after 1.6 μs and for R34 after 6.6 μs , thus the almost doubling of the particle size leads to a four times slower decay rate.

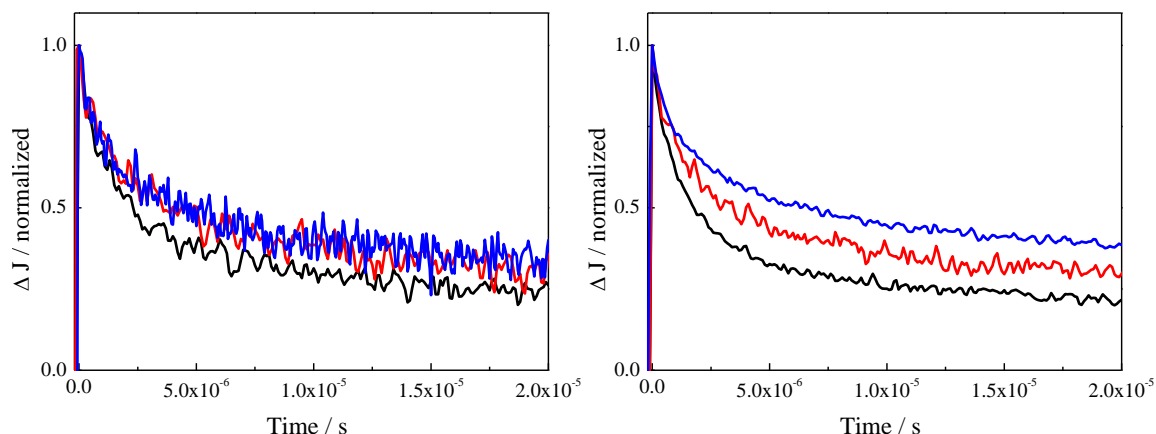


Figure 4.26: Normalized transient absorption signals observed at (left) 390 nm, and (right) 410 nm for the charge carriers photogenerated in (black) R15, (red) R25, and (blue) R34. Experimental conditions: N_2 saturated TiO_2 powders, $\lambda_{\text{exc}} = 351 \text{ nm}$, laser intensity: $30 \text{ mJ cm}^{-2} \text{ pulse}^{-1}$.

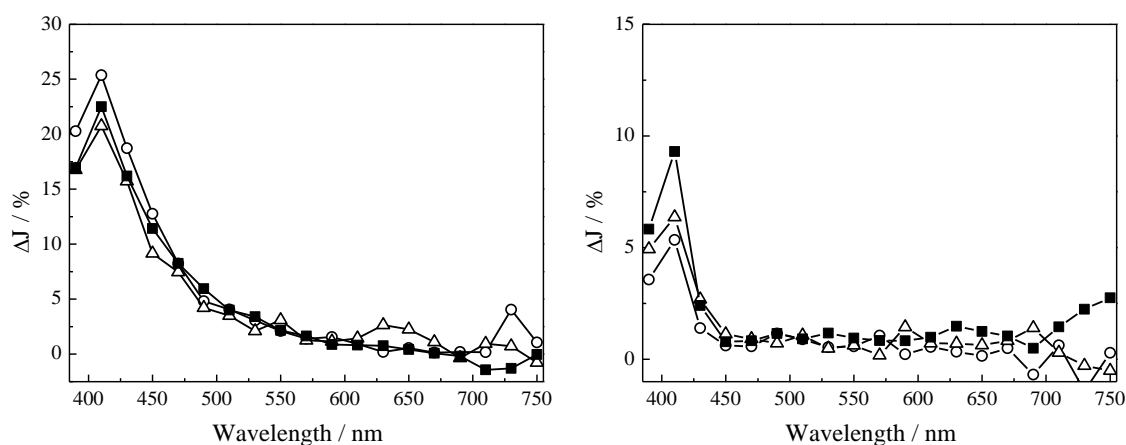


Figure 4.27: Transient absorption spectra observed (left) 0.229 μs and (right) 17 μs after the laser pulse of the charge carriers photogenerated in (-○-) R15, (-■-) R25, and in (-▲-) R34. Experimental conditions: N_2 saturated TiO_2 powders, $\lambda_{\text{exc}} = 351 \text{ nm}$, laser intensity per pulse: $30 \text{ mJ cm}^{-2} \text{ pulse}^{-1}$.

As observed for the R15 sample the transient absorption maximum at higher excitation intensity is shifted to longer wavelengths also for the two other rutile samples (see Figure 4.27). For better comparison of the decay signals recorded at different excitation wavelengths, the experiments with $\lambda_{\text{exc}} = 351 \text{ nm}$ have been carried out at higher excitation intensities. Figure 4.27 (right) presents the transient absorption signals recorded at different decay times, namely, 0.229 μs and 17 μs after the laser pulse. No shift of the transient absorption with the decay time could be detected, indicating no transformation of the initially detected transient species to another product, thus the recombination of the charge carriers apparently proceeds without the formation of additional intermediates. However, the formation of such intermediate species cannot be completely excluded,

4. Results

since the latter may exhibit similar transient absorption properties as the initially formed transient. The transient absorption intensity varies only slightly for the different rutile samples.

5. Discussion

This chapter will begin with the discussion of the obtained structural changes of TiO₂ upon laser excitation followed by the interpretation of the transient absorption spectra measured under different conditions. Hereby, the effect of the photoinduced reconstruction of the TiO₂ particles on the transient absorption properties of the trapped charge carriers will be in focus of the discussion. Finally, the recombination kinetics of the trapped charge carriers will be described employing a second order kinetic law. The latter will be modified according to the thus derived correlations of the absorption properties with the laser intensity as well as of the recombination rate constants with the particle size.

5.1 Formation of Ti³⁺ centers and anatase to rutile phase transition upon laser exposure

As the Raman spectra (see Figure 4.1) revealed the excitation of the UV100 TiO₂ anatase powder by a 351 nm laser pulse leads to an anatase to rutile phase transition. Moreover, the formation of long-lived Ti³⁺ species located in the rutile phase is detected by means of EPR- and UV-vis-Spectroscopy. These results clearly prove a laser-induced rearrangement of the TiO₂ lattice. It is more likely that the reconstruction of the TiO₂ structure occurs at the particle surfaces rather than in the bulk, since the former exhibits a higher defect density and thus a higher reactivity.¹²⁷ However, the question arises, whether the absorbed laser energy is invested into a temperature rise followed by a thermal anatase to rutile transition or it is directly transferred to the lattice inducing a bond breakage on the molecular level.

The laser-induced anatase to rutile phase transition has been already studied by several research groups, whereas some of them reported photoinduced thermal driven phase transitions.^{128, 129} Wilkinson and Willsher pointed out that materials exhibiting a large optical absorption coefficients such as TiO₂ or Fe₃O₄ (i.e., with $\alpha > 10^4 \text{ cm}^{-1}$) are likely to experience photoinduced thermal heating.¹³⁰ Hereby the heat is homogeneously distributed over the illuminated volume resulting in a large temperature rise following the pulsed excitation. The temperature induced in TiO₂ by a single laser pulse can be estimated according to the following equation:¹³⁰

5. Discussion

$$Q_0 = \frac{E_0 \cdot \alpha}{\rho \cdot C} \quad (5.1)$$

Q_0 : Temperature (K)

E_0 : Incident Energy per unit area (J cm^{-2})

C : Specific heat capacity ($\text{J g}^{-1} \text{K}^{-1}$)

ρ : Density (g cm^{-3})

α : Absorption coefficient (m^{-1})

Accordingly, the required temperature for the anatase to rutile phase transition of 680°C can be achieved with a laser intensity of $40 \text{ mJ cm}^{-2} \text{ pulse}^{-1}$ (using values for the anatase phase, i.e., $\alpha = 1.2 \cdot 10^4 \text{ cm}^{-1}$, $C = 0.69 \text{ J g}^{-1} \text{ K}^{-1}$, and $\rho = 1 \text{ g cm}^{-3}$ (lower density value than that reported for bulk TiO_2 (3.9 g cm^{-3}) due to the powdered samples used in the experiments).¹³¹

However, such a photoinduced thermal heating of the illuminated volume followed by a phase transition is less probable. It contradicts to the studies of Stopper and Dohrmann, who demonstrated by means of time-resolved optoacoustic calorimetry that 88 % of the released heat is dissipated in a few nanoseconds over the whole system thus no significant temperature increase occurs.¹³² Recently, Ricci *et al.*^{133, 134} have shown by a careful analysis of the Stokes to anti-Stokes Raman peak ratio that the local temperature of the nanoparticles during the laser illumination was 370 K, thus an only thermally driven anatase to rutile phase transition could be ruled out. Moreover, Yates *et al.*¹³⁵ have found that the photoinduced reconstruction of the TiO_2 surface was not affected by cooling the surface below 150 K.

In fact, the photoinduced desorption/adsorption of oxygen molecules on the surface of nanometer sized TiO_2 systems is reported to play a fundamental role for the non-thermal phase transition induced upon laser illumination.^{133, 134, 136, 137} Hereby, the phase transition was attributed to surface modifications by a proper depletion of adsorbed oxygen on the crystal surface. The desorption of the oxygen molecules from the TiO_2 lattice yielding oxygen vacancies leads to an enhancement of the surface chemical reactivity. Subsequently, stable chemical bonds are formed between the surfaces of neighboring anatase particles resulting in the formation of polycrystalline aggregates. The interface between the bound anatase particles, which are only present in the inner region of these agglomerated particles, provides the nucleation sites of the rutile phase.¹³⁸ The formation of the rutile phase inside of the aggregate is in agreement with our results. We,

furthermore, detected long-lived trapped electrons in the rutile phase, the lower reactivity of which evinces that they are located inside the TiO_2 aggregate or cluster. The appearance of such non-reactive subsurface trapped electrons by tempering has also been reported by Diebold *et al.*¹³⁹. The relative number of the preferential nucleation sites for the anatase to rutile phase transition is found to increase as the population of oxygen vacancies at the particle surface increases.^{133, 134} Zhou *et al.*^{127, 140} reported that the rutile phase nucleates exactly at the twin boundaries generated by anatase 112 surfaces. If the direct contact between anatase particles is prevented, the phase transformation was found to be retarded or prohibited at all. For example, no phase transformation has been observed for anatase TiO_2 particles functionalized with nitric groups or with a La_2O_3 shell.^{133, 138}

The long-lived Ti^{3+} centers in TiO_2 detected in the present study are most likely produced by oxygen removal during the laser illumination of anatase TiO_2 (this has also been detected for the rutile phase). Desorption of one oxygen molecule leaves four additional electrons in the lattice. These electrons can either stay in the vacancy forming so-called F-centers, or they are transferred to Ti^{4+} yielding Ti^{3+} species. The conversion of Ti^{4+} to Ti^{3+} upon laser excitation with 355 nm has already been reported by Forsgren *et al.*¹⁴¹. Concomitantly, the hydrophilicity of the surface was improved. Since we were able to detect such Ti^{3+} centers by means of EPR- and UV-vis-Spectroscopy (see Figure 4.2), this evinces that the phase transition observed in the present study occurs *via* the photoinduced oxygen desorption. However, the question arises, how the formation of the oxygen vacancies or of the rather long-lived Ti^{3+} species proceeds.

For example, Serpone *et al.*^{6, 122} reported that during laser flash photolysis studies long-lived Ti^{3+} centers can be produced *via* the so-called Auger recombination process. This Auger process is found to be the predominant mechanism when the number of photons exceeds the number of absorbing particles by far, which is in agreement with our experimental conditions.^{142, 143} In the Auger process the energy released by the recombination of an electron-hole pair is absorbed by another electron (or hole) resulting in the formation of highly energetic electrons (or holes), which can dissipate the energy either by an electron ejection from the semiconductor nanoparticle resulting in the formation of solvated electrons or by a phonon emission leading to the generation of long-lived deeply trapped electrons. The presence of solvated electrons can be ruled out here since the experiments have been performed employing dry TiO_2 powders instead of aqueous TiO_2 suspensions. However, the only experimental evidence for the formation of

5. Discussion

such Ti^{3+} species *via* an Auger process is the fact that the published transient absorption signals detected in TiO_2 do not decay to the initial value observed before the laser pulse but exhibit a long-lived transient absorption signal within the time scale of observation.^{6, 7, 9, 11, 15, 16, 144} Moreover, the Auger recombination is normally observed in heavily doped, direct bandgap semiconductors. In direct bandgap semiconductors the recombination proceeds upon releasing photons, while in indirect semiconductors in most cases phonons are released, the energy of which is usually not high enough to excite other charge carriers.⁵⁸

Lisachenko *et al.*¹⁴⁵ proposed two possible processes to explain for the photodesorption of oxygen molecules from the metal oxide surface:

(1) Photothermic processes, whereby the excitation energy is transformed into phonon energy of the solid resulting in the excitation of the vibrational mode of the surface-atom bond followed by the rupture of this bond.

(2) Photoelectronic processes, whereby the excitation energy is absorbed by the atom-surface bond thus changing the potential energy of the bond directing it towards the repulsive branch of the potential curve for the atom-surface interaction. Subsequently, the potential energy is converted into kinetic energy of the emitted particles, thus entailing the nature of its desorption. This mechanism is based on the research of Terenin, who pointed out that the emitted particle can gain the rest of the photon energy, if the latter exceeds the energy necessary for bond breaking.¹⁴⁶

Based on Time-of-Flight (TOF) spectroscopy measurements, which allow the determination of the temperature of the desorbed molecules, Lisachenko ruled out the photothermic model.¹⁴⁵ In photothermic processes the average velocity of the desorbed molecules should correspond to the surface temperature. The detected kinetic temperature of the desorbed oxygen molecules, however, exceeds by far the highest surface temperature produced by the laser beam. The photodesorption of oxygen from the TiO_2 surface is rather found to proceed *via* photoelectronic processes induced by electronic transitions. Hereby, the photodesorption of preadsorbed oxygen molecules (which are present on the metal oxide surface partially reduced, i.e., as superoxide radical anions) is caused by the capture of a photogenerated hole.¹⁴⁷⁻¹⁴⁹



The desorption of the oxygen molecule from the TiO₂ surface lattice includes the partial neutralization of the oxygen anion:¹³⁵



The oxidation of further oxygen anions results in the transformation of two neighboring O²⁻ anions into molecular oxygen. Accordingly, two single-photon excitations are required for the formation of one oxygen vacancy:



The structural changes of the TiO₂ lattice observed in the present study can only be induced by the removal of strongly bound species according to eqs. 5.3. and 5.4. The photooxidation of lattice bound oxygen *via* photogenerated holes resulting in the release of molecular oxygen has been proposed as a mechanism for O₂ formation by Salvador¹⁵⁰ and for the gas phase photocatalytic oxidation of organic compounds by Pichat^{151, 152} and Lisachenko.¹⁵³

The idea behind the mechanism of photoelectronic processes including the excitation energy transfer to the surface-atom bond resulting in the formation of an oxygen vacancy is also supported by other experimental techniques such as ion and electron bombardment, where the kinetic energy of the accelerated ions is transferred to the TiO₂ lattice.^{154, 155} Actually, Fukushima *et al.*¹⁵⁶ observed the anatase to rutile transition during the TiO₂ film formation by means of ion bombardment. Moreover, the laser induced phase transition of Silicon has been explained by energy transfer from optically excited electron-hole plasma to the crystal lattice resulting in the crystal melting. This process is known as non-thermal melting.¹⁵⁷⁻¹⁵⁹ However, the latter occurs only at femtosecond excitation at a laser fluency of about 0.2 J cm⁻².

According to the above presented discussion, in the photoinduced processes the absorbed light energy is transferred to the lattice inducing bond-breaking and displacement of atoms involved in the reconstructive transformation from anatase to rutile. According to Stopper and Dohrmann 88 % of the energy absorbed by colloidal TiO₂ after the laser pulse is dissipated in less than one nanosecond as heat over the whole system as the consequence of the charge-carrier recombination, while the remaining 12 %

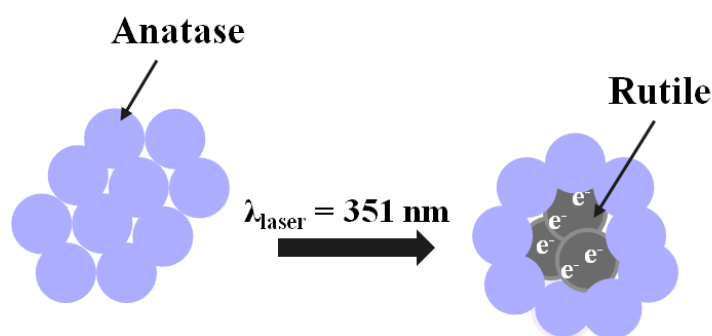
5. Discussion

can be stored for at least 2 μs .¹³² Applying a laser pulse with an excitation wavelength of 351 nm a total energy of 347 kJ mol^{-1} can be released as heat. According to Stopper and Dohrmann 305 kJ mol^{-1} will be dissipated over the whole particulate system, while 42 kJ mol^{-1} can be utilized locally. Employing a laser intensity of $23 \text{ mJ cm}^{-2} \text{ pulse}^{-1}$ one UV100 anatase nanoparticle can absorb 522 photons (see table 5.1 below). Assuming that every absorbed photon is utilized as much as $21924 \text{ kJ mol}^{-1}$ can be locally converted into the bond breaking. For the cleavage of one Ti-O bond an energy of 315 kJ mol^{-1} is required. Hence, with the one laser pulse of 23 mJ cm^{-2} up to 70 Ti-O bonds per TiO_2 anatase particle can be broken. For the transition of bulk anatase to rutile it was reported that 7 out of the 24 Ti-O bonds per unit cell need to be broken leading to the cooperative displacement of both Ti and O.^{133, 137} It is more likely, however, that most of the Ti-O bonds are broken at the TiO_2 surface. The anatase nanoparticles of UV100 are spherical in shape, therefore the number of TiO_2 unit cells present at the surface is estimated to be 180. Hence, during each laser pulse 3 Ti-O bonds per unit cell can be broken. Subsequently, that is already after the second laser pulse, the phase transition can be initiated.

The inhomogeneous distribution of the black spots containing the rutile phase and long-lived Ti^{3+} -centers (see Figure 4.1) observed here for the laser irradiated powder samples indicates different reactivities of the TiO_2 clusters at the surface. Assuming a homogeneous distribution of the photons over the illuminated TiO_2 surface all exposed TiO_2 units should be destabilized during the laser pulse. As a result bond breaking and atom displacement can occur. After the laser illumination the more stable TiO_2 units manage to return back into the initial state (this self-repair mechanism can also be supported by the photo adsorption of the oxygen or water molecules), thus the initial anatase phase remains (see Figure 4.1). However, the more reactive TiO_2 clusters (most likely due to a higher defect density) undergo intense irreversible structural changes such as oxygen removal followed by the observed phase transition. The latter results in the reported grey-blue coloration of the TiO_2 sample. As a matter of fact, the photodeposition of metal nanoparticles on metal oxide surfaces also results in an inhomogeneous distribution of metal islands on the surface.¹⁶⁰

Summing up the above presented discussion, the following laser-induced processes take place in anatase TiO_2 powder upon illumination with intense laser pulses: formation of electron-hole pairs, followed by an energy and charge transfer to the TiO_2 lattice. The regions of the TiO_2 surface with high defect density undergo irreversible changes, such as

removal of the lattice oxygen resulting in the formation of oxygen vacancies. This enhances the surface reactivity of the TiO₂ particles, thus at the interfaces of the anatase nanoparticles the phase transition to rutile occurs. The presence of the Ti³⁺ centers in the illuminated powder evinces that the phase transition to rutile occurs *via* the oxygen release from the TiO₂ surface induced by the electron/energy transfer (see Scheme 5.1). However, the major part of the TiO₂ nanoparticles are able to conduct self-repair processes and therefore exhibit no significant morphological and structural changes.



Scheme 5.1: Schematic illustration of the laser-induced processes occurring in anatase TiO₂ (Hombikat UV100).

The message of the discussion presented here so far is that upon the illumination with pulsed laser light intense structural changes of the TiO₂ photocatalyst may proceed. These findings are essential for the evaluation of the underlying photocatalytic reactions. Although there are many studies which present such structural changes of the TiO₂ nanoparticles upon illumination,^{128, 151, 152, 161-165} this effect has rarely been considered for the interpretation of photocatalytic processes.¹⁶⁶ Based upon these possible reactions it is certainly highly indicated to study the role of the surface reorganization on the photoinduced reactions upon the illumination. The knowledge of these processes can most probably open new design pathway for the future photocatalysts.

5.2 Assignment of the transient absorption spectra

TiO₂ is one of the most studied photocatalysts. In the scientific literature different laser flash photolysis studies are presented dealing with the reaction dynamics of the charge carriers photogenerated in colloidal TiO₂ suspensions⁶⁻⁹, in TiO₂ films¹⁰⁻¹⁴, and in dry TiO₂ powders^{94, 100, 167, 168} as already mentioned in chapter 2.1. In all these publications the authors attributed the optical changes induced by laser excitation in TiO₂ to the formation of free and trapped electrons as well as of trapped holes. The analysis of the

5. Discussion

published transient absorption spectra for different TiO₂-samples recorded in the absence of any electron donor and acceptor revealed that the feature of transient absorption spectra is less dependent on the sample preparation, i.e., film, powder, or colloidal suspension rather than on the time resolution of the respective laser study. Hence, most of the transient absorption spectra measured in the picoseconds time regime exhibit transient absorption maxima located above 600 nm.^{6, 14, 15, 73} In some studies a continuous increase of the transient absorption intensity with the wavelength has been reported.^{33, 169, 170} In the nanosecond to microsecond time scale the intensity of the transient absorption at the longer wavelengths decreases, while at around 500 nm no changes occur resulting in a spectral blue shift. The dependence of the spectral changes on the time resolution of the laser study is depicted in Figure 5.1 (left). Since the trapped holes absorb in the UV-vis and electrons in the vis-IR wavelength region, the blue shift of the transient spectra observed at different times after the laser pulse has been related to the fact that the surface trapped electrons are photogenerated immediately after the excitation and relax during the next 500 ps into deeper traps in the bulk (see Figure 5.1 (right)), while the holes remain at the TiO₂ particle surface.³³

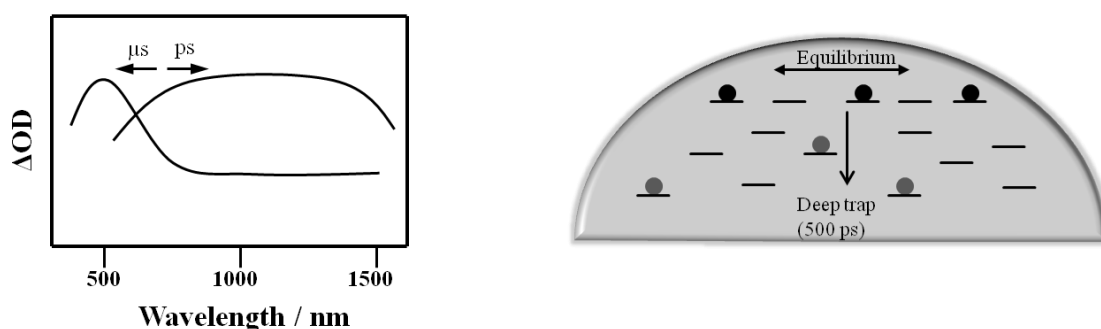


Figure 5.1: (left) Comparison between the typical initial transient absorption spectrum observed in a picosecond and in a nanosecond laser flash photolysis experiment, respectively. (right) Schematic diagram illustrating the spatial and energetic distribution of electron traps in a TiO₂ particle.

Similar to the reports published in the literature very broad transient absorption spectra with a maximum located around 500 nm for colloidal anatase nanoparticles (see Figure 4.4 (right)) and for TiO₂ anatase UV100 (see Figure 4.7 (right)) have been observed here 0.1 μs after the laser pulse. Both samples show a slight increase of the initial signal intensities with the observation wavelength. Upon increasing the laser intensity the transient absorption below 450 nm drastically increases, while the transient signals in the visible range only exhibit slight changes (see Figure 4.5 (right) and Figure 4.8 (right)).

For rutile a similar transient absorption has been detected but already at lower laser intensities of $7 \text{ mJ cm}^{-2} \text{ pulse}^{-1}$ (see Figure 4.11 (right)). In this study the observed transient absorption spectrum for rutile corresponds very well to the reported one.¹⁶⁷ The different transient absorption spectra for rutile and anatase observed at the same laser excitation conditions have been explained by a different trapping behavior of the photogenerated charge carriers in the different phases. However, the discussion presented below provides another explanation for the detected difference between the anatase and the rutile phases.

For a better comparison of the results obtained with different TiO_2 samples it is important to determine the amount of the absorbed photons per TiO_2 particle and per TiO_2 unit. The amount of photons absorbed per TiO_2 particle (N_p) or per TiO_2 unit (N_u) during the laser pulse can be calculated according to:

$$N_p = \frac{I \cdot \lambda_{\text{exc}} \cdot 1/6 \cdot \pi \cdot d^3 \cdot \alpha}{c \cdot h} \quad (5.5)$$

$$N_u = \frac{I \cdot \lambda_{\text{exc}} \cdot V_{\text{EZ}} \cdot \alpha}{c \cdot h \cdot Z} \quad (5.6)$$

I: Laser intensity [$\text{J m}^{-2} \text{ pulse}^{-1}$]

λ_{exc} : Excitation wavelength [m]

d: Crystallite diameter [m]

V_{EZ} : Volume of the unit cell [m^3]

Z: Number of TiO_2 molecules per unit cell

α : Absorption coefficient [m^{-1}]

c: Speed of light [m s^{-1}]

h: Planck constant [J·s]

These equations are developed under the assumption that the particles are spherical. The light penetration depth and the illuminated area determine the illuminated volume; hereby the former one is determined by the reciprocal value of the absorption coefficients representing the absorption depth. Table 5.1 summarizes the calculated number of absorbed photons generated at two different laser intensities for three different TiO_2 samples, namely for dry colloidal TiO_2 powder, UV100, and R15.

5. Discussion

Table 5.1. Number of photons per TiO₂ particle and per TiO₂ unit calculated according to eqs. 5.5 and 5.6 for different TiO₂ samples with the absorption coefficient at 351 nm being $1.2 \cdot 10^6 \text{ m}^{-1}$ for anatase and $6 \cdot 10^6 \text{ m}^{-1}$ for rutile.¹⁷¹

Sample	I / $\text{mJ cm}^{-2} \text{ pulse}^{-1}$	d_{Particle} / nm	N_{p}	N_{u}	$1/N_{\text{u}}$
TiO ₂ Colloid	10	7	38	0.006	167
TiO ₂ Colloid	28	7	106	0.019	52
UV100	7	12.7	159	0.005	200
UV100	23	12.7	522	0.016	62
R15	7	20	3,107	0.023	43
R15	30	20	13,322	0.103	10

According to equations 5.5 and 5.6 the number of absorbed photons per particle is directly proportional to the absorption coefficient, which depends on the crystallographic phase of TiO₂. Since rutile exhibits a much higher absorption coefficient at 351 nm than anatase, the former absorbs considerably more photons per laser pulse provided that all other parameters are kept constant. For example, R15 absorbs around 3,000 photons per particle at a laser intensity of $7 \text{ mJ cm}^{-2} \text{ pulse}^{-1}$, while UV100 absorbs by a factor of 20 less photons at the same laser intensity conditions. Comparing the number of photons absorbed per TiO₂ unit in case of UV100 at a laser intensity of $23 \text{ mJ cm}^{-2} \text{ pulse}^{-1}$ every 62nd TiO₂ unit in a particle is excited per laser pulse, while in R15 already at lower laser intensities every 43rd particle is absorbing a photon. These simple calculations demonstrate that for a "fair" comparison of the transient absorption spectra observed in rutile and in anatase the laser intensity should be adjusted accordingly. This explains the already reported difference between the transient absorption spectra of rutile and anatase. Since the transient absorption spectra have been recorded at the same laser intensity, but in rutile much more particles are excited than in anatase different absorption spectra are monitored. In this work the transient absorption spectra observed in rutile at a laser intensity of $7 \text{ mJ cm}^{-2} \text{ pulse}^{-1}$ are comparable with the spectra observed for anatase samples at a laser intensity of $23 \text{ mJ cm}^{-2} \text{ pulse}^{-1}$. Figure 5.2 shows the normalized transient absorption spectra taken at $0.109 \mu\text{s}$ after the laser pulse for three different TiO₂ photocatalysts: UV100, R15, and colloidal TiO₂ powder. In all three materials a continuous increase of the transient absorption signal upon decreasing observation wavelength is observed until at 390 nm the highest transient absorption signal is reached. In contrast, the transient absorption in the visible range decreases according to the order colloidal TiO₂ > UV100 > R15. These results clearly show that the population of the

photogenerated intermediates responsible for the transient absorption in the visible range depends on the morphological properties of TiO₂.

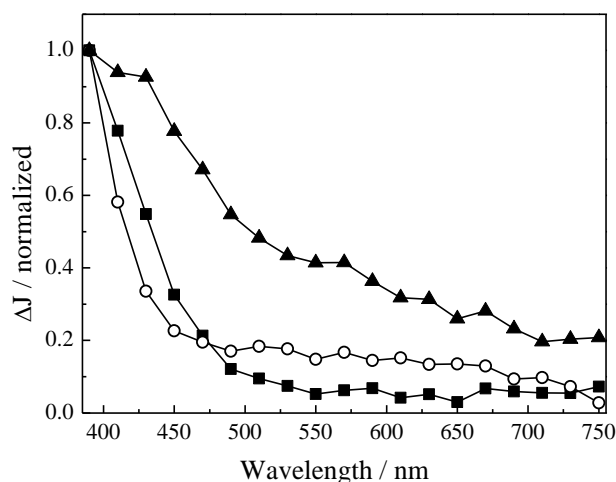


Figure 5.2: Normalized transient absorption spectra observed 0.109 μ s after the laser pulse for (○) UV100 powder, (■) R15 powder, and (▲) colloidal TiO₂ powder. Experimental conditions: N₂-saturated powders, laser intensity per pulse: UV100: 23 mJ cm⁻² pulse⁻¹ (N_u : 0.016), R15: 7 mJ cm⁻² pulse⁻¹ (N_u : 0.023), and colloidal TiO₂: 28 mJ cm⁻² pulse⁻¹ (N_{unit} : 0.019).

In order to identify the region in the transient absorption spectra where the photogenerated intermediates, i.e., trapped electrons as Ti³⁺ centers and trapped holes as \cdot OH/O[•], adsorbed electron acceptors or donors have been added prior to the laser flash experiments. A general trend for all three TiO₂ samples (colloidal TiO₂, UV100, and R15) has been observed: The modification of TiO₂ with an electron acceptor such as Pt leads to a decrease of the transient absorption at wavelengths higher than 450 nm, while at shorter wavelengths no change could be observed. The addition of methanol as an electron donor (or rather hole acceptor) has an opposite effect. The transient absorption in the wavelength region between 390 nm and 450 nm decreases, while at higher wavelengths a continuous increase with the wavelength is monitored. According to these results the latter transient absorption is attributed to the trapped electrons and the former transient absorption to the trapped holes. However, it should be noted here, that the trapped electrons contribute to the transient absorption in the entire wavelength region studied here.

For a better correlation of the transient absorption to the trapped species difference spectra have been calculated. The transient absorption spectrum observed in the presence of the electron donor or acceptor has been subtracted from the transient absorption spectrum observed under inert atmosphere. Since for colloidal TiO₂ suspension no

5. Discussion

transient absorption spectrum could be detected in the absence of scavengers, the transient absorption spectra obtained in the presence of methanol and Pt or O₂ have been subtracted from each other. As shown in Figure 5.3 the trapped holes photogenerated in colloidal TiO₂ exhibit a transient absorption between 390 nm and 550 nm, while the trapped electrons absorb mostly above 550 nm. This outcome corresponds to the published results in which for colloidal particles the transient absorption recorded in the nanosecond time regime at around 520 nm-550 nm has been attributed to the trapped holes.^{11, 167, 172} Using AgNO₃ as the electron scavenger, Durrant *et al.*^{70, 168} attributed the transient absorption at around 460 nm also to the trapped holes. However, their data analysis not been taken into account that the Ag nanoparticles formed during the reduction of the Ag⁺ cations exhibit a plasmon band in this region, which may strongly influence the transient absorption signal. Ilya *et al.*⁹ related the origin of the vis absorbing holes to the common ion impurities in colloidal TiO₂. The trapped holes are more UV-absorbing as shown by radiolysis experiments.^{39, 173} In contrast to the colloidal particles the trapped holes in the bulk TiO₂ powders exhibit no or only a minor transient absorption above 450 nm (see Figure 5.4). Apparently, more trap states located within the band gap are available for the trapping of the holes in the colloidal particles than in the bulk TiO₂ powder.

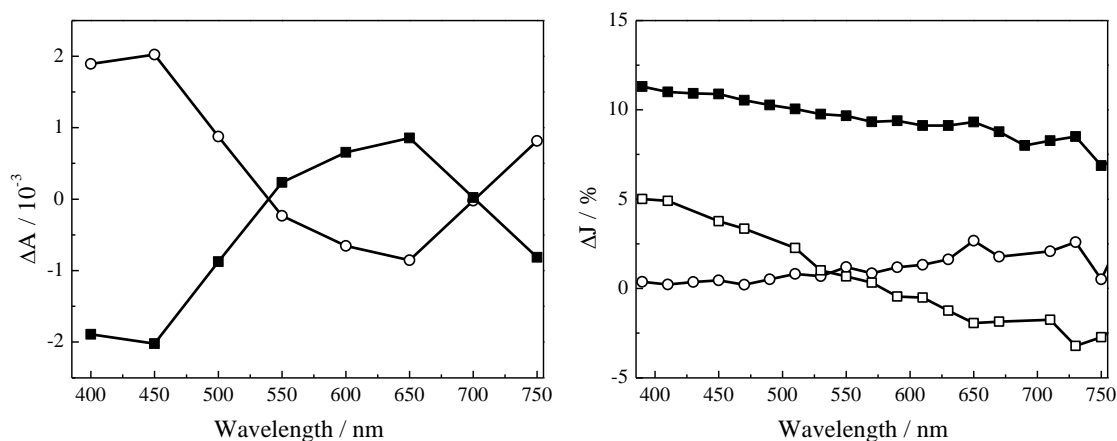


Figure 5.3: (left) Difference transient absorption spectra for transparent colloidal TiO₂ suspension (experimental conditions see Figure 4.15 and Figure 4.16) with (—○—) $\Delta J_{\text{CH}_3\text{OH}} - \Delta J_{\text{Pt}}$. (right) Difference transient absorption spectra for colloidal TiO₂ powder (experimental conditions see Figure 4.17 and Figure 4.18) with (—□—) $\Delta J_{\text{N}_2} - \Delta J_{\text{CH}_3\text{OH}}$, (—○—) $\Delta J_{\text{N}_2} - \Delta J_{\text{O}_2}$. (—■—) Transient absorption spectrum observed under inert atmosphere (experimental conditions see Figure 4.4).

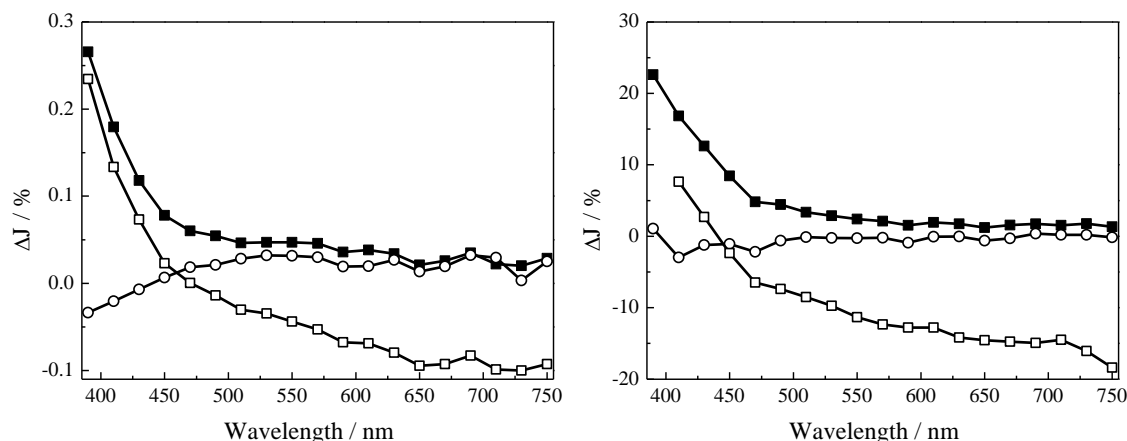


Figure 5.4: Difference transient absorption spectra for (left) UV100 powder and for (right) R15 powder (experimental conditions see Figure 4.19, Figure 4.20, and Figure 4.21, Figure 4.22, respectively) with (-□-) $\Delta J_{N_2} - \Delta J_{CH_3OH}$, (-○-) $\Delta J_{N_2} - \Delta J_{Pt}$, (-■-) Transient absorption spectrum observed under inert atmosphere (experimental conditions see Figure 4.8 and Figure 4.12).

The change of the transient absorption in the wavelength range above 450 nm in the presence of electron donors and acceptors, respectively, indicates that the trapped electrons are located close to the surface, thus they can be readily transferred to Pt. Moreover, in case of rutile and anatase longer life-time of the trapped holes in the presence of Pt have been detected, evincing its role as sufficient electron scavenger (see Figures (left) 4.21, and 4.22). However, the decay kinetics in the presence of O_2 did not change due to the slower reaction of the electrons with adsorbed O_2 molecules (see Figure 4.17 (left)).^{11, 51}

The photooxidation of methanol *via* the photogenerated holes leads to an accumulation of the remaining electrons on the TiO_2 surface resulting in build-up (see Figures (left) 4.18, 4.20, and 4.22). The formation of the additional trapped electrons proceeds through so-called current doubling effect (see equation 4.4). In the absence of molecular oxygen as effective electron scavenger, TiO_2 changes its colour from white to blue indicating the formation of Ti^{3+} centers. The photogenerated electrons are located in the respective traps at the photocatalyst surface and are available now for different reduction reactions.^{174, 175} It has even been reported that in the presence of alcohol a change from n-type to p-type semiconductor behavior may occur⁸⁶.

5.3 Contribution of the long-lived Ti^{3+} centers to the transient absorption spectra upon high laser excitation density

As shown in chapter 5.1 irreversible changes of TiO_2 occur during pulse irradiation with high laser excitation densities. Non-reactive Ti^{3+} centers and a subsequent anatase to rutile phase transition for anatase TiO_2 are detected under these conditions. It is important to mention here, that the change in the reflection observed for anatase below 450 nm at high laser intensities cannot only be related to the transition of the anatase to the rutile phase, since for rutile a similar transient absorption has been detected but already at lower laser intensities of $7 \text{ mJ cm}^{-2} \text{ pulse}^{-1}$ (see Figure 4.11) similar to the transient absorption spectra reported for rutile previously.¹⁶⁷ However, the laser-induced modification of all three TiO_2 samples affects the transient absorption signals. Several observations presented below will support this statement. Firstly, the detected transient absorption signals do not decay to the initial value observed before the laser pulse but exhibit long-lived transients within the time scale of observation. This can be explained assuming that the initial optical properties of TiO_2 before the laser exposure are altered by changes of its stoichiometric composition and by a phase transition as shown in this work. Secondly, a linear dependency of the long-lasting transient absorption on the laser intensity has been found for the rutile phase (see Figure 4.13 (right)). Apparently, the number of the laser-produced long-lived Ti^{3+} centers is higher at higher laser intensities. Moreover, zero intercept of the linear fit of the data suggests (see Figure 4.13 (right)) that in rutile these irreversible changes occur already at very low laser intensities. Also for the anatase phase a long-lived transient component has been detected already at low laser intensities. However, this long-lived transient absorption does not increase with the laser intensity but rather remains constant, in contrast to rutile (see Figure 4.9 (right)). This difference of rutile and anatase samples will be discussed in the next chapter. It is important to notice here, that the long-lasting transient absorption is present at all wavelengths studied. This correlates very well with the UV-vis spectrum of the laser treated TiO_2 exhibiting visible light absorption (see Figure 4.2 (left)).

The observed changes in TiO_2 are most likely complete before the measurement of the transient absorption starts, i.e., 100 ns after the laser pulse. For example, it has been shown that the phase transformation of GaAs proceeds within 200 fs, while the atomic displacement in silicon has been found to occur within 120 fs after the laser pulse.¹⁵⁸ Zhou *et al.*¹²⁷ performed molecular simulation techniques to investigate the anatase to

rutile phase transition. They observed the formation of rutile nucleates with induction times ranging from 26 ns–47 ns. Moreover, the laser-induced darkening of TiO₂ due to the formation of Ti³⁺ centers has been monitored employing femtosecond excitation with laser intensities of less than 200 nJ.¹⁷⁶ According to this consideration the alteration of the TiO₂ phase should strongly affect the transient absorption within the whole investigated time range. Hence, it has been found for all three phases that the transient absorption at 390 nm increases much faster than that at above 450 nm upon increasing the laser intensity. It is important to mention here that for rutile and anatase a linear dependency of the transient absorption signal on the laser intensity has been found indicating that third order processes and nonlinear optical processes can be excluded, since for a two-photon process the transient absorption should depend on the square of the light intensity (see Figure 4.9 (left) and Figure 4.13 (left)). In chapter 5.2 has been shown that the detected transient absorption in the wavelength region between 390 nm and 450 nm results from the formation of trapped holes. Moreover, previous reports are supporting the identification of this transient absorption in mentioned wavelength region^{39, 177, 178} However, the contribution of the photogenerated long-lived Ti³⁺ centers to the transient absorption of the trapped holes is obvious. The difference transient absorption spectra of the spectrum observed at high and low laser excitation clearly demonstrates this. The difference transient absorption above 450 nm is almost zero, while at shorter wavelengths it is still higher than 15 % (see Figure 5.5).

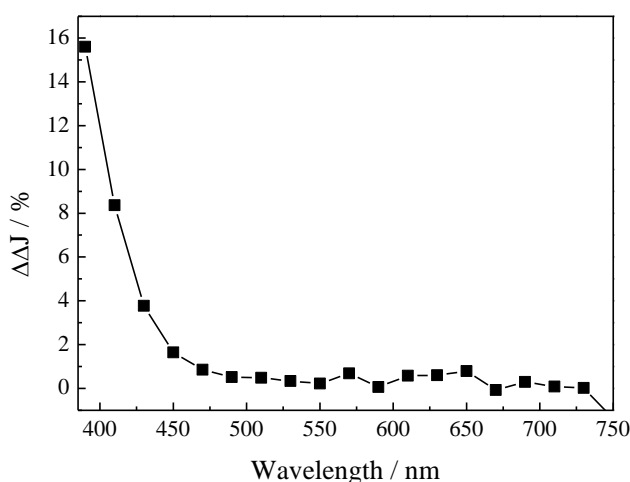


Figure 5.5: Difference transient absorption spectrum for UV100 powder with $\Delta\Delta J = \Delta J_{(23\text{mJ cm}^{-2}\text{pulse}^{-1})} - \Delta J_{(7\text{mJ cm}^{-2}\text{pulse}^{-1})}$, (experimental conditions see Figure 4.7 (right) and Figure 4.8 (right)).

5. Discussion

Several scenarios should be considered to explain the observed spectral changes. On the one hand, the observed transient absorption could represent the sum of the transient absorption induced by the trapped charge carriers and by the long-lived Ti^{3+} centers formed during the laser pulse:

$$\Delta J = A = A_{e^-/h^+} + A_{\text{Ti}^{3+}} = (\epsilon_{e^-} + \epsilon_{h^+}) \cdot c_{e^-/h^+} + \epsilon_{\text{Ti}^{3+}} c_{\text{Ti}^{3+}} \quad (5.7)$$

There are studies showing that oxygen vacancies exhibit an optical transition in the UV-vis wavelength region.¹⁷⁹ Moreover, an increase of the extinction coefficient of TiO_2 in the discussed wavelength range has been reported after heating TiO_2 at 1000 °C.¹⁸⁰ This change in the extinction coefficient has been explained by the formation of Ti^{3+} centers in TiO_2 upon heating. However, in this case contributions to the transient absorption spectra should be found in the entire spectral range rather than only at wavelengths below 450 nm.

On the other hand, the presence of the long-lived Ti^{3+} centers could strongly influence the extinction coefficient of the trapped holes. For example, Katoh *et al.*¹¹⁴ have observed an increased transient absorption of the trapped electrons at high laser excitation density employing picosecond laser pulses. The authors related this change to the increased extinction coefficient of the trapped electrons due to the Coulomb interaction induced by the holes formed at high laser intensity. They supported their conclusion by the report of Boschloo *et al.*¹⁸¹ who observed an increase of the extinction coefficient of the trapped electrons induced by intercalating cations such as Li^+ . In the present study, it seems very likely that due to the Coulomb interaction between the long-lived Ti^{3+} centers and the trapped holes an increase of the extinction coefficient of the latter will be induced. Hence, in accordance with the observations made here, the initial transient absorption intensity should increase linearly with the laser intensity as the amount of the long-lived Ti^{3+} centers also grows steadily. This increase of the transient absorption signal is found to be dependent on the wavelength which can readily be explained by the dependency of the absorption coefficient on the wavelength. Moreover, the influence of the long-lived Ti^{3+} centers on the extinction coefficient of the surface trapped electrons is rather low, since both species are spatially separated: the former are located inside of the agglomerate, while the latter are trapped directly at the particle surface.

The contribution of the absorption of the long-lived electrons to the observed transient absorption spectra can also be explained considering the experiments performed for

colloidal and bulk TiO₂ powders in the presence of the electron acceptors and donors. In the presence of Pt only slight changes below 450 nm have been monitored. This evinces that the transient absorption of the formed long-lived electrons predominates the spectrum in the considered wavelength region. Since such electrons are remote from the surface, similar to O₂ they cannot be transferred to Pt. Hence, their interaction with the trapped holes is still relevant in the presence of Pt. In contrast to the experiments with Pt, the transient absorption below 450 nm decreases in the presence of methanol as electron donor. Here the photogenerated holes are removed, thus the photoinduced formation of oxygen vacancies (see chapter 5.1) or rather long-lived trapped electrons is prohibited. In this case neither long-lived Ti³⁺ centers nor trapped holes are present and the observed transient absorption consists only of contributions of the surface trapped electrons.

Finally, the transient absorption spectra observed at high laser energy, namely at 248 nm, have to be discussed. Using the excitation wavelength of 248 nm a transient absorption maximum at 370 nm has been observed for the anatase phase (see Figure 4.6 (right) and 4.10 (right)). This absorption maximum can predominately be explained by the increase of the extinction coefficient of the trapped holes resulting from the formation of the long-lived trapped charge carriers as described in detail above. It should also be mentioned here that Lawless *et al.*³⁹ reported for •OH radicals trapped at the TiO₂ surface an absorption maximum of 350 nm. For the rutile phase at very high laser excitation conditions, which is also the case upon excitation with 248 nm pulses, a red shift of the maximum from 390 nm to 410 nm is detected (see Figure 4.14 (right)). Already at laser intensities above 20 mJ cm⁻² a saturation of the transient absorption at 390 nm occurs (see Figure 4.13 (right)). This saturation effect can be explained by the fact that the change in the extinction coefficient of TiO₂, which occurs due to the formation of long-lived charge carriers, reached its maximum since only a limited amount of the oxygen vacancies or rather long-lived Ti³⁺ centers can be formed in the TiO₂ phase. Moreover, a decrease of the transient absorption above 500 nm has been observed for all three phases when changing the laser excitation wavelength from 351 nm to 248 nm. This reveals either that the number of the surfaces trapped states for the electrons is reduced upon excitation with 248 nm due to the surface reconstruction or that due to the interaction of the reactive Ti³⁺ with the long-lived Ti³⁺ centers the extinction coefficient of the former decreases. It has been shown that the absorption coefficient of Ti³⁺ embedded in silicate decreases with increasing basicity.¹⁸² Drouilly *et al.*¹⁸³ reported that in ZnO the basicity increases with increasing the oxygen vacancy concentration. Hence, the long-lived Ti³⁺ centers detected

5. Discussion

in the present study will also increase the basicity of the TiO_2 particle surfaces thus leading to a decrease of the extinction coefficient of the trapped electrons absorbing above 450 nm. This effect of the long-lived Ti^{3+} centers is more pronounced upon excitation with 248 nm, since under these conditions the penetration depth of the excitation light is shorter resulting in a much higher charge carrier density and thus a reduced distance between the both species. For the colloidal TiO_2 powder the reduction of the extinction coefficient of the trapped electrons occurs already upon 351 nm excitation. The transient absorption above 500 nm decreases upon increasing the laser intensity (see Figure 4.5 (right)) in comparison to the transient observed at low laser intensities (see Figure 4.4 (right)). Due to the smaller particle size of the colloidal TiO_2 the distance of the long-lived Ti^{3+} centers to the surface trapped electrons is lower, thus their interaction can lead to the above described reduction of the extinction coefficient. Moreover, the observed lower transient absorption for the rutile phase above 450 nm (see Figure 5.2) in comparison to the anatase TiO_2 phase can also be explained by this phenomenon. Due to the higher extinction coefficient of rutile at 351 nm, the charge density in each particle is higher and thus the interaction of the long-lived Ti^{3+} with the surface trapped electrons is stronger.

However, the detailed kinetic analysis of all transients following in the next chapter will present more details to the correlation between the transient absorption spectra and the observed structural changes of the TiO_2 material.

5.4 Recombination kinetics of the photogenerated charge carriers

5.4.1 Dependency on the laser intensity

In this chapter the analysis of the recombination kinetics of the photogenerated charge carriers will be presented. In particular, the effect of the laser intensity or rather of the effect of the long-lived trapped electrons formed at higher laser intensities on the recombination rate constant will be discussed. First analysis of the transient absorption of the trapped charge carriers in colloidal TiO_2 powder will be presented followed by the analysis of the transient signals obtained for UV100 and for R15.

As discussed in detail above the analysis of the transient absorption spectra revealed that two trapped species are formed 100 ns after the laser excitation. These are the holes trapped as oxygen centered radicals ($\cdot\text{OH}$, O^\cdot), and the trapped electrons as Ti^{3+} species. The former absorb in the UV region below 450 nm, while the latter absorb above 450 nm.

The trapped holes formed in colloidal TiO₂ exhibit a broader transient absorption in the wavelength range between 390 nm and 530 nm. Subsequently, the observed decay of the transient absorption in the absence of any electron donor and acceptor can be attributed to the recombination of the trapped electrons with the trapped holes according to equation 5.8. The presence of free or shallowly trapped charge carriers can be neglected, since it has been shown that they react in a timescale of picoseconds (see Figure 2.4).



Different fitting models have been developed to describe the observed decay behavior of the transient absorption as presented in chapter 2.2.3. The transient absorption signals observed for all materials studied here follow bimolecular second order kinetics according to equation 2.9. In contrast to equation 2.9 instead of the charge carrier number $\langle x \rangle(t)$ the transient absorption ΔA has been measured and needs to be introduced in equation:

$$\Delta J = \Delta A = \frac{A_0}{A_0 k_r t + 1} \quad (5.9)$$

Taking into account the relation given in equation 3.5 expression 5.9 can be written as:

$$\Delta J = \Delta A = \frac{\varepsilon_T \cdot c_0}{c_0 k_r t + 1} + B \quad (5.10)$$

where c_0 presents the initial concentration of the formed transient species, exhibiting certain ε_T relative extinction coefficient, and B is the long-lasting transient absorption. The presented transient absorption signals in chapter 4 can be fitted applying the above presented function, although some boundary conditions have to be defined. It is assumed that the concentration of the trapped electrons and holes, which survive in nanosecond timescale and react with each other, is equal:

$$c_0(e_{tr}^+) = c_0(h_{tr}^+) = c_0 \quad (5.11)$$

Hence, if the transient absorption observed at a certain wavelength represents the transition from the trapped state to the conduction band, than c_0 should be wavelength independent. Here, c_0 was set arbitrarily to 0.028 a.u., thus the value of the relative extinction coefficient calculated from the fit function is relative and not an absolute

5. Discussion

number. The fit to second order kinetics for the transient absorption at 450 nm is shown in Figure 5.6 for colloidal TiO₂ powder observed at two different laser pulse energies.

The perfect matching of the fit function with the time dependent change of the transient signals evinces that the bimolecular recombination of the trapped charge carriers (equation 5.8) with one other is the predominant process in the studied time scale region at different laser intensities. The exact recombination rate constant and the initial concentration of the transient species can only be determined if the extinction coefficient of the trapped species is known. It has been reported that the extinction coefficients for the electrons vary strongly between 800-2600 M⁻¹ cm⁻¹ depending on the material preparation. The spectroelectrochemically estimated extinction coefficient for the holes has been reported to be 2930 M⁻¹ cm⁻¹, and for the electrons 2440 M⁻¹ cm⁻¹.^{184, 185} The former deviates strongly from the reported extinction coefficient for the free [•]OH radical of 540 M⁻¹ cm⁻¹.⁴⁹ Due to these discrepancies and to the fact that the extinction coefficient of the trapped species is not known for the TiO₂ powder, in the following, the results will be discussed employing the rate constants with the units for k_r being s⁻¹ a.u.⁻¹

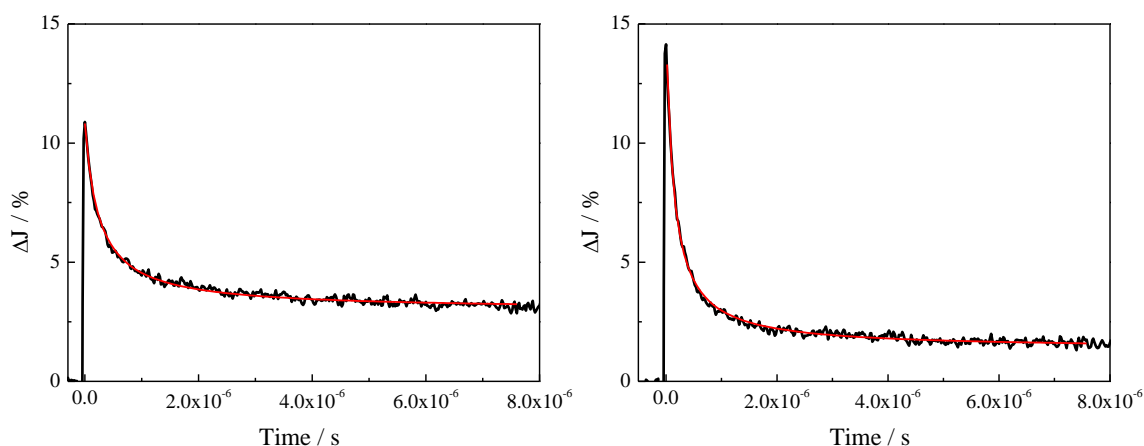


Figure 5.6: Transient absorption signals observed at 450 nm upon laser excitation with $\lambda_{\text{exc}} = 351$ nm for colloidal TiO₂ powder measured (left) at 10 mJ cm⁻² pulse⁻¹ and (right) at 28 mJ cm⁻² pulse⁻¹. The red line represents a fit to second order kinetics according to equation 5.10.

In Figure 5.7 (left) thus determined recombination rate constants are plotted for different wavelengths. As expected the recombination rate constant is wavelength independent and average value of $1.2 \pm 0.2 \cdot 10^8$ s⁻¹ a.u.⁻¹ is found. The relative extinction coefficient depends on the wavelength exhibiting a slight maximum at 450 nm. The ratio of 1.2 of the extinction coefficient obtained at 450 nm to that obtained at 600 nm correlates very well

with the ratio of the spectroelectrochemically determined extinction coefficient of the holes to that of the electrons reported in the literature.⁸⁰

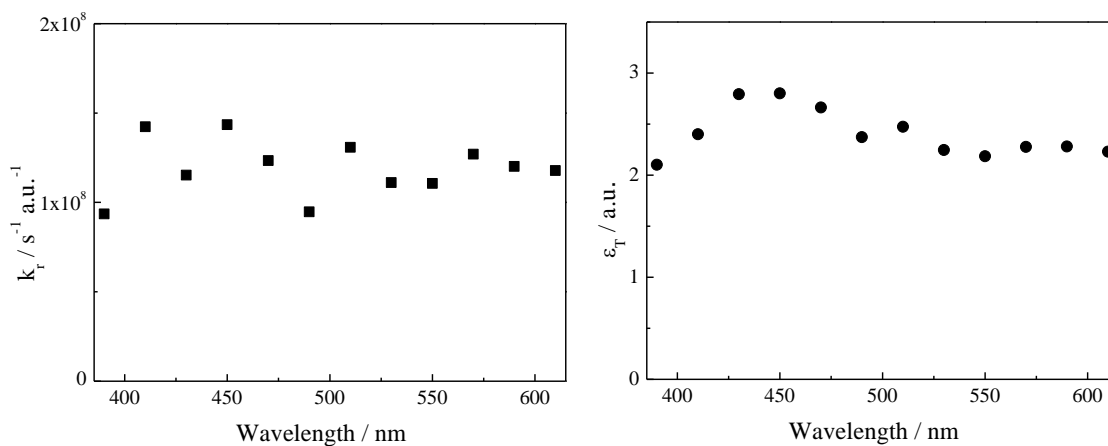


Figure 5.7: (left) Second order rate constants k_T and (right) relative extinction coefficients ϵ_T of the transient species obtained at different wavelengths for colloidal TiO_2 powder at $10 \text{ mJ cm}^{-2} \text{ pulse}^{-1}$.

Figure 5.8 shows the recombination rate constants and the relative extinction coefficients obtained at higher laser intensities. It is apparent that the rate constants obtained in the wavelength region between 430 nm and 500 nm are higher in comparison to the rate constants obtained at lower laser intensities. This correlates also with the life-times of the transients, namely, in the discussed wavelength range a decrease of the life-time $t_{1/e}$ upon increasing the laser intensity is observed (see Figures (left) 4.4, and 4.5). It can be assumed that in the present study the trapped states are already saturated at a laser intensity of $7 \text{ mJ cm}^{-2} \text{ pulse}^{-1}$. Moreover, the life-time of the trapped charge carriers exhibiting transient absorption signals between 390 nm and 430 nm, as well as those absorbing above 500 nm do not change upon increasing the laser intensity evincing that c_0 does not change. Since the concentration of the trapped charge carriers should be the same in the studied wavelength, the observed increase of the rate constant of the transient signals between 430 nm and 500 nm indicates that the trapped species have an additional route to react besides their recombination. This phenomenon is more pronounced for rutile TiO_2 and will be discussed in more detailed later.

It is obvious from the results presented in Figure 5.8 (right) that at higher laser intensities the relative extinction coefficient below 500 nm increases strongly with the decrease of the wavelength, while above 500 nm similar values for the relative extinction coefficient are found as at lower laser intensities. Principally, the relative extinction coefficient should remain constant upon increasing the laser intensity. However, as

5. Discussion

discussed in chapter 5.3 due to the coulombic interaction of the long-lived Ti^{3+} centers formed during initial pulse period with the trapped holes the relative extinction coefficient of the former can be enhanced. Based upon the results obtained from the kinetic data analysis carried out here, which are shown in Figure 5.8 (right), this effect could be proven.

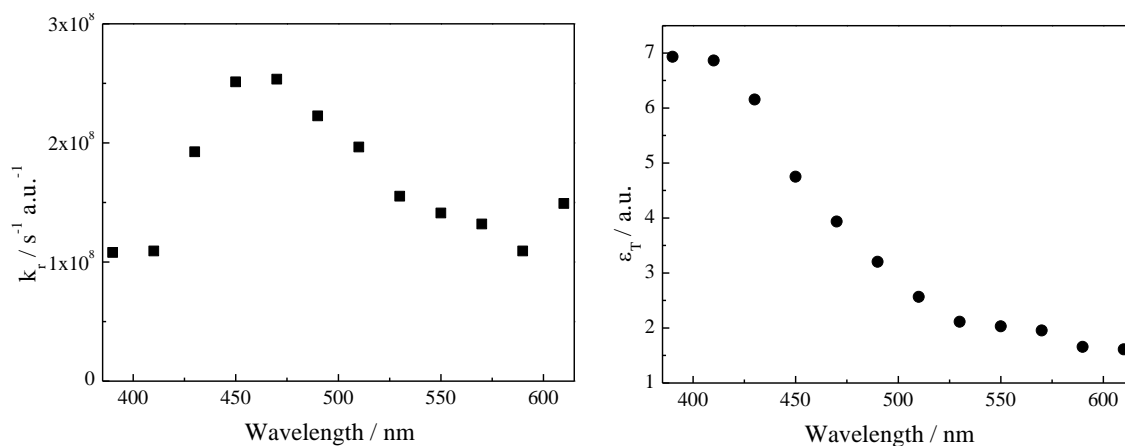


Figure 5.8: (left) Second order rate constants k_r and (right) relative extinction coefficients ϵ_T of the transient species obtained for different wavelengths for colloidal TiO_2 powder at $28 \text{ mJ cm}^{-2} \text{ pulse}^{-1}$.

The transient absorption signals obtained for UV100 also obey second order kinetics according to equation 5.10 (see Figure 5.9). Similar to colloidal TiO_2 powder, the estimated recombination rate constants are wavelength independent at lower laser intensities (see Figure 5.10 (left)). For k_r an average value of $2.2 \pm 0.3 \cdot 10^8 \text{ s}^{-1} \text{ a.u.}^{-1}$ is found. A direct comparison of the recombination rate constants of the different materials is not possible, since the exact concentration of the trapped species is not known. However, both recombination rate constants are of the same order of magnitude, in good correlation with the observation of similar charge carriers life-times observed for colloidal TiO_2 powder and for UV100 (see chapter 4). It is important to mention here that both TiO_2 materials also exhibit similar primary particle sizes.

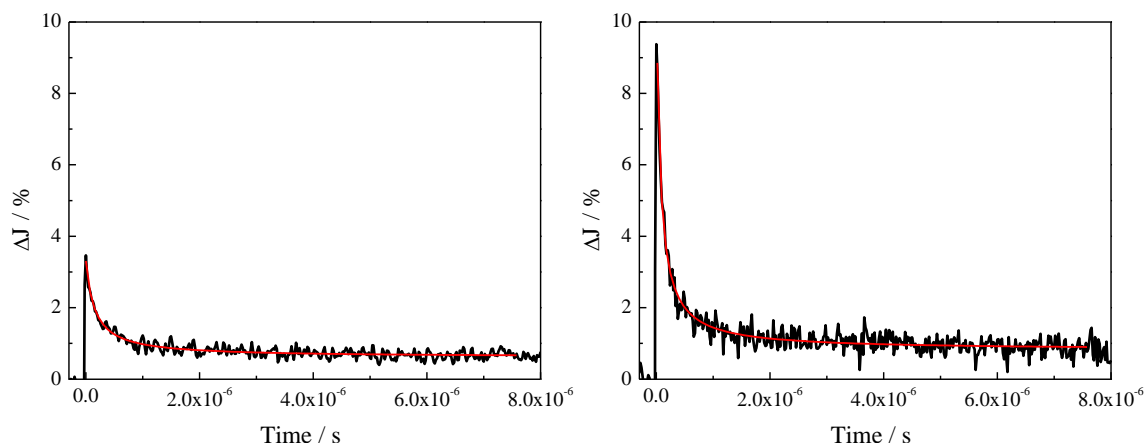


Figure 5.9: Transient absorption signals observed at 450 nm upon laser excitation with $\lambda_{\text{exc}} = 351$ nm for UV100 (left) at $7 \text{ mJ cm}^{-2} \text{ pulse}^{-1}$ and (right) at $23 \text{ mJ cm}^{-2} \text{ pulse}^{-1}$. The red line represents a fit to second order kinetics according to equation 5.10.

The wavelength dependency of the relative extinction coefficients is presented in Figure 5.10 (right). In comparison to the colloidal TiO_2 powder smaller values are found. Principally, the relative extinction coefficient for the trapped charge carriers should be constant for different TiO_2 samples. The observed discrepancy can be explained by the fact that for both TiO_2 samples the same value of 0.028 has been chosen for c_0 . It can be concluded that the concentration of the photogenerated trapped species in colloidal TiO_2 powder is higher than in bulk UV100, since the former exhibits a higher number of defects resulting from the sol-gel synthesis. A more detailed discussion of the dependency of the relative extinction coefficient on the type of TiO_2 sample will be presented below.

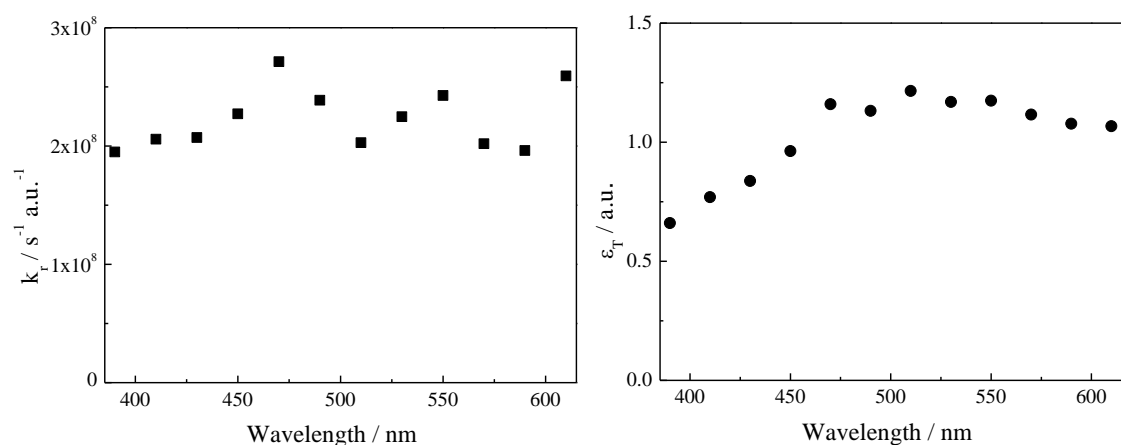


Figure 5.10: (left) Second order rate constants k_r and (right) relative extinction coefficients ε_T of the transient species obtained at different wavelengths for UV100 at $7 \text{ mJ cm}^{-2} \text{ pulse}^{-1}$.

Similar to the results discussed for the colloidal particles, also for UV100 the recombination rate constant in the wavelength range between 430 nm and 500 nm

5. Discussion

increases upon increasing the laser intensity indicating a new reaction route for the trapped charge carriers (see Figure 5.11 (left)). In all other wavelength regions the rate constant does not change, as expected. These results correlate very well with the $t_{1/e}$ values obtained at different excitation conditions (see Figures (left) 4.7, and 4.8). As depicted in Figure 5.11 (right) below 500 nm the relative extinction coefficient of the trapped holes increases drastically due to the Coulomb interaction with the long-lived Ti^{3+} centers, which are formed at higher laser intensities during the initial pulse period.

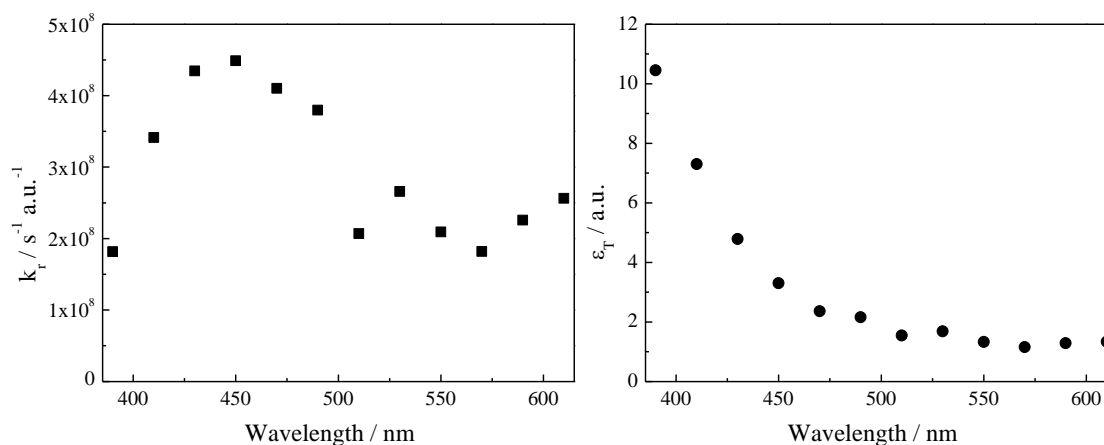


Figure 5.11: (left) Second order rate constants k_r and (right) relative extinction coefficients ϵ_T of the transient species obtained at different wavelengths for UV100 at $23 \text{ mJ cm}^{-2} \text{ pulse}^{-1}$.

For a better understanding of the effect of the laser intensity on the recombination rate constants and on the relative extinction coefficients, the transient absorption signals of the trapped holes obtained with different laser intensities at 390 nm have been analyzed in detail. As shown in Figure 5.12 the recombination rate constants remain constant, while the relative extinction coefficients increase linearly with the laser intensity. As discussed in the previous chapter the electronic transition and thus the relative extinction coefficient of the trapped holes can be influenced by the coulombic interaction with the long-lived trapped electrons. The Coulomb potential depends besides on the distance between the two charges in particular on the charge density. In the present case the charge density is determined by the concentration of the long-lived Ti^{3+} centers. As discussed above, upon increasing the laser intensity the number of the long-lived Ti^{3+} centers increases, hence that their interaction with the trapped holes will become stronger resulting in an enhancement of the relative extinction coefficients. Accordingly, the relative extinction coefficient can be defined as:

$$\epsilon_T(390 \text{ nm}) = \epsilon_T' I \quad (5.12)$$

where ε_T' represents the intensity independent relative extinction coefficient [a.u./ mJ cm⁻² pulse⁻¹] and I the laser intensity. Most likely the ε_T' value of 1.31 found for UV100 is also valid for other 100 % anatase particles exhibiting similar particle sizes, since as it will be shown below ε_T does not depend on the particle size.

Taking into the account the relationship given in (5.12) equation 5.10 can be modified as follows:

$$\Delta J = \Delta A = \frac{\varepsilon_T' I c_0}{c_0 k_r t + 1} + B \quad (5.13)$$

Hereby, it is important to mention that ε_T' is wavelength dependent and needs to be determined separately for each wavelength.

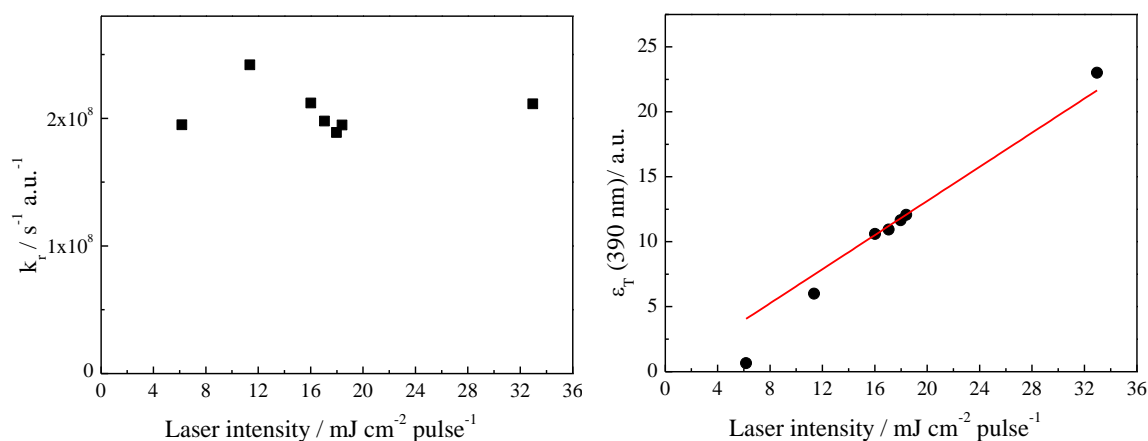


Figure 5.12: (left) Second order rate constants k_r and (right) relative extinction coefficients ε_T of the transient species obtained at different laser intensities for UV100 at 390 nm. The red line represents the linear fit with the formula: $\varepsilon_T(390 \text{ nm}) = 1.31 \pm 0.07 \cdot I$

Figure 5.13 shows the perfect matching of the transient absorption signals obtained for rutile TiO₂ R15 at two different laser intensities with a fit to second order decay kinetics. Since the $t_{1/e}$ presented in chapter 4.2.3 does not change upon the increasing the laser intensity, as it was observed for anatase samples, the critical conditions for rutile are already achieved at laser intensities of 7 mJ cm⁻² pulse⁻¹. Hence, in the following only the decay kinetics at the lower laser intensity will be analyzed.

5. Discussion

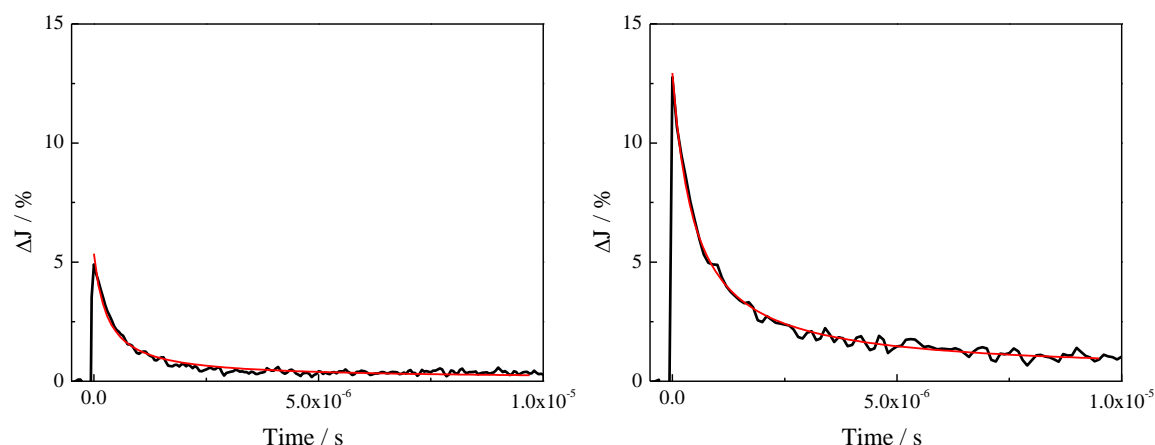


Figure 5.13: Transient absorption signals observed at 450 nm upon laser excitation with $\lambda_{\text{exc}} = 351$ nm for R15 (left) at $7 \text{ mJ cm}^{-2} \text{ pulse}^{-1}$ and (right) at $30 \text{ mJ cm}^{-2} \text{ pulse}^{-1}$. The red line represents a fit to second order kinetics according to equation 5.10.

The analysis of the transient absorption signals measured at different wavelengths revealed that the recombination rate constant at wavelengths above 470 nm is wavelength independent exhibiting a value for k_r of $1.7 \pm 0.2 \cdot 10^8 \text{ s}^{-1} \text{ a.u.}^{-1}$, while at shorter wavelengths the decay rate constants are found to be one order of magnitude lower. Apparently, in rutile particles the trapped electrons react faster than the trapped holes in obvious contradiction to the above presented model. This discrepancy can be explained by a model employed in conventional photoelectrochemistry; that is, the energy of the lower edge of the conduction band of n-type semiconductors decreases with increasing distance from the surface resulting in the so-called upward band bending and the concomitant formation of a space-charge layer. Subsequently, the photogenerated charge carriers can be spatially separated. The electrons are forced to migrate into the bulk of the semiconductor particles, while the holes remain at their surface (see Scheme 5.2 (left)).

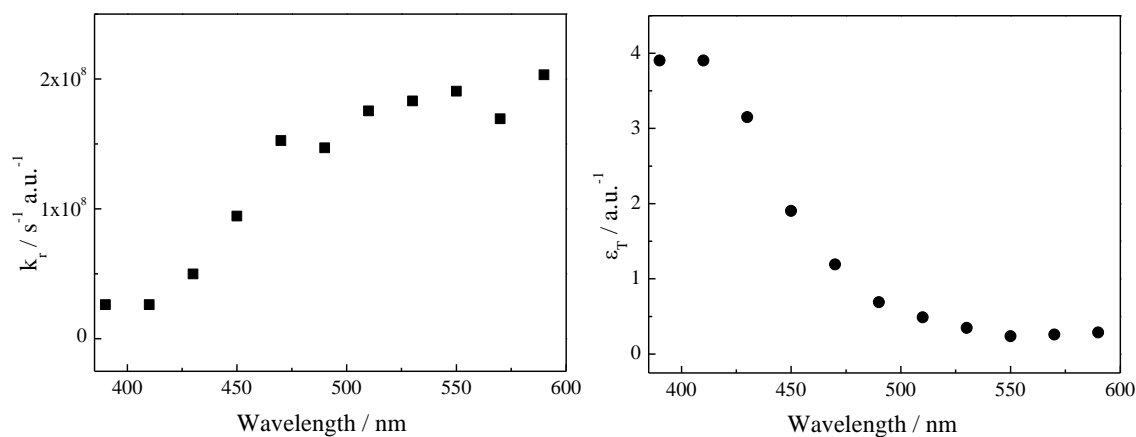
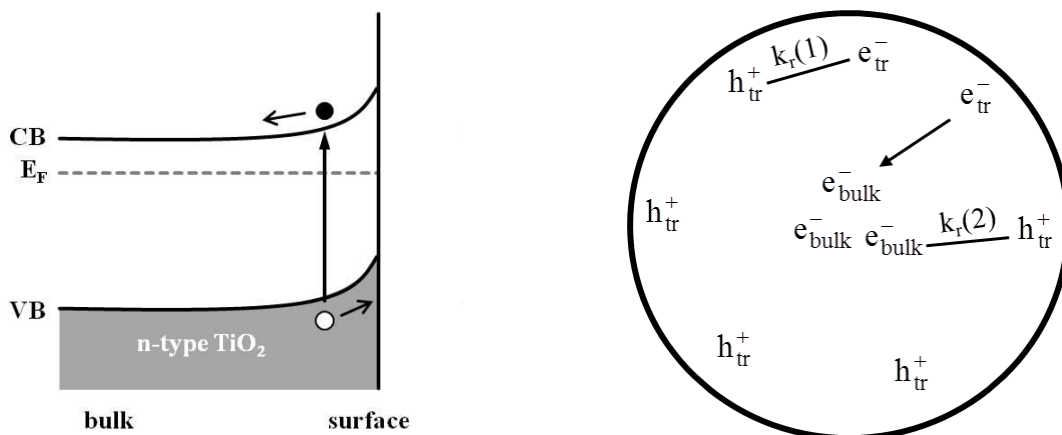


Figure 5.14: (left) Second order rate constants k_r and (right) the relative extinction coefficients ε_T of the transient species obtained at different wavelengths for R15 at $7 \text{ mJ cm}^{-2} \text{ pulse}^{-1}$.



Scheme 5.2: (left) Schematic diagram of the migration of photogenerated electrons into the bulk across space charge layer and the accumulation of the holes at the surface of the illuminated semiconductor. (right) Schematic illustration of the recombination processes between the surface trapped holes and electrons denoted as $k_r(1)$, and the recombination between the surface trapped holes and bulk electrons $k_r(2)$.

However, the magnitude of the band bending V_{BB} depends on the particle size r_0 , the dopant concentration N_d , and the relative dielectric constant ϵ_r :¹⁸⁶

$$V_{BB} = \frac{\epsilon r_0^2 N_d}{6\epsilon_r \epsilon_0} \quad (5.14)$$

The band bending effect becomes relevant for n-doped TiO₂ nanoparticles with particle diameters exceeding 15 nm.¹⁸⁷ An important difference between the anatase nanoparticles discussed above to the rutile nanoparticles is that in case of rutile a higher concentration of dopants, namely of the long-lived Ti³⁺ centers formed upon laser exposure, can be expected. For example, Selloni *et al.*¹⁸⁸ have shown that anatase is more difficult to reduce than rutile. Moreover, the rutile nanoparticles employed here exhibit a slightly bigger mean particle radius of 20 nm than UV100 ($d = 12.7$ nm) and colloidal TiO₂ ($d < 10$ nm). Accordingly, in rutile even the electrons initially formed near the particles' surface migrate into the bulk from where they then undergo recombinations with the surface trapped holes with the recombination rate constants denoted in Scheme 5.2 (right) as $k_r(2)$. This increased distance between the reactants leads to the observed deceleration of the recombination process. Apparently, the bulk electrons do not exhibit any appreciable transient absorption in the studied wavelength range. The rather small number of the remaining surface trapped electrons recombines with surface trapped holes with $k_r(1)$ as denoted in Scheme 5.2 (right). The latter process shows higher recombination rate constants, which are, however, in the same order of magnitude as estimated for anatase

5. Discussion

TiO₂. Moreover, as presented in chapter 4.2.3 the long-lived transient absorption, which is more pronounced at shorter wavelengths, where the trapped holes absorb, than at longer wavelengths, where the trapped electrons absorb, can be attributed to the remaining transient absorption of the trapped holes, which obviously react very slowly with the bulk electrons. Obviously, most of the surface trapped electrons have migrated into the bulk, thus the remaining transient absorption at wavelengths above 450 nm is very low. Moreover, a linear dependency of the long-lived component of the transient absorption signal at 390 nm with the laser intensity has been found (see Figure 4.13 (right)). This can be explained by the fact, that upon increasing the laser intensity the concentration of the long-lived Ti³⁺ centers increases leading to a stronger upward band bending and subsequently to a higher number of slowly reacting trapped holes absorbing at 390 nm. It should be mentioned here, that the constant value B (see equation 5.10) can be also explained by very slow recombination processes as suggested by Serpone *et al.*⁶

Similar to anatase below 500 nm the relative extinction coefficients of the trapped holes in rutile increase strongly, while the relative extinction coefficients of the trapped electrons remain unchanged as depicted in Figure 5.14 (right). However, in contrast to the anatase nanoparticles, in case of rutile this phenomenon is observed already at low laser intensities due to the higher number of the photons absorbed by the rutile nanoparticles per laser pulse as discussed in chapter 5.3.1.

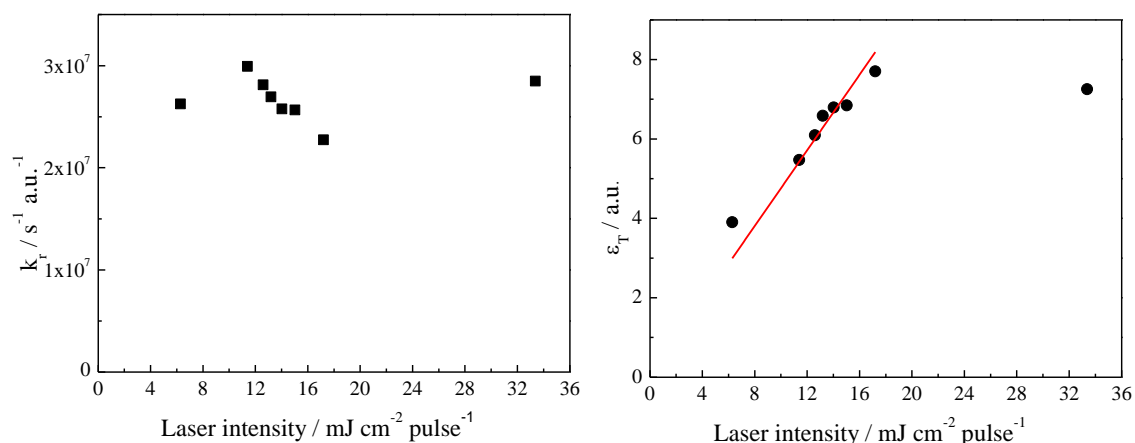


Figure 5.15: (left) Second order rate constants k_r and (right) relative extinction coefficients ϵ_T of the transient species obtained at different laser intensities for R15 at 390 nm. The red line represents the linear fit with a formula: $\epsilon_T(390 \text{ nm}) = 0.95 \pm 0.03 \cdot I$

For the rutile powder no change of the recombination rate constant could be detected upon increasing the laser intensity, while the relative extinction coefficient of the trapped

holes increases linearly with the laser intensity (see Figure 5.15) Hence, all the arguments presented above for anatase are also valid for rutile and equation (5.13) can be applied for rutile samples with ε_T' of 0.95 at 390 nm.

Finally, it is important to compare the decay kinetics observed upon excitation with 248 nm laser pulses. As Figures 4.6, 4.10, and 4.14 show the excitation with the shorter wavelength leads for all three TiO₂ samples to an acceleration of the decay kinetics at longer wavelengths, while only slight changes are observed at shorter wavelengths. These results can be explained using Scheme 5.2 (right). The high charge carrier density and the shorter penetration depth of the laser beam with $\lambda_{\text{exc}} = 248$ nm induce intense structural changes of the studied material surface. Hence, most likely, the surface trapped electrons are transferred from the surface into the bulk of the particle resulting in their shorter lifetime.

In summary, it can be concluded that the change of the relative extinction coefficient obtained for all three TiO₂ samples upon increasing the laser intensity correlates very well with the discussion presented in chapter 5.3. The comparison of the relative extinction coefficients obtained for different TiO₂ morphologies reveals that the concentration of the trapped states is the highest at colloidal anatase TiO₂ particles, while it is the lowest for rutile particles, since in all cases the initial concentration was kept constant and it was assumed that the relative extinction coefficient of the trapped species does not depend on the structural properties of TiO₂. These findings can be readily explained, since the colloidal particles exhibit a higher number of defects and thus trapping sites, while at the rutile surface due to its smaller surface area a considerably reduced number of the trapping sites is present. However, the effect of the long-lived Ti³⁺ centers on the relative extinction coefficient of the trapped holes does not depend on the TiO₂ morphology. For both, anatase and rutile similar values for ε_T' have been found.

Considering the charge carriers recombination kinetics a simple second order rate law could be applied to describe the photoinduced processes under different excitation conditions and for different TiO₂ powders according to equation 5.13. The observed recombination rate constants -at least in the wavelength range where trapped electrons absorb- are similar exhibiting an order of magnitude of $10^8 \text{ s}^{-1} \text{ a.u.}^{-1}$. Comparable values have been reported for the relative recombination rate constant by other research groups working in this field.^{15, 75} The important difference of rutile in comparison to anatase is that in rutile structural changes can be more easily induced upon illumination, resulting in

5. Discussion

a stronger influence of the photogenerated charge carriers on the reaction dynamics. Subsequently, this could also be one of the reasons for the different photocatalytic activities of rutile and anatase. While the former is known as a good oxidant, which is also obvious due to the longer life-time of the trapped holes, the latter is able to reduce protons yielding hydrogen. This could be explained by the presence of considerably higher number of trapped electrons at the surface of the anatase particles, from where they can be transferred more easily to their reaction partners.

5.4.2 Dependency on the particle size

It is well established that besides the morphology of TiO_2 also the particle size plays an important role for the photocatalytic processes. From TRMC (Time-Resolved-Microwave-Conductivity) measurements and laser flash results employing aqueous colloidal TiO_2 suspensions it is known that the increase of the particle sizes leads to longer life-times of the photogenerated charge carriers.^{122, 189} In the present study anatase TiO_2 samples exhibiting different particle sizes have been investigated (see Figure 4.23). The comparison of the transient absorption signals revealed a deceleration of the decay kinetics upon increasing particle sizes (see Figure 4.24). The transient absorption spectra, on the other side, are only slightly influenced by the particle size (see Figure 4.25). For all anatase TiO_2 samples the observed decay kinetics of the transient absorption signals follows second order kinetics according to equation 5.10, and a linear dependency of the reciprocal second order recombination rate constant on the particle size has been found. Figure 5.16 (left) presents the reciprocal recombination rate constant of the transient absorption recorded at 390 nm as a function of the particle size. Obviously, the decay rate constants decrease as the particle sizes increases. The relative extinction coefficient of the trapped holes, however, remains constant for all anatase TiO_2 samples. Apparently, the photoinduced structural changes of the anatase TiO_2 samples do not depend on the particle size, since the amount of the photons absorbed per TiO_2 unit was the same in all these experiments.

The obtained dependency of the rate constant on the particle size can be explained using the band bending model described above. According to equation 5.14 the magnitude of the band bending is proportional the particle radius, thus in case of the bigger particles a stronger upward band bending is expected resulting in a better separation of the photogenerated charge carriers as depicted in Scheme 5.3.

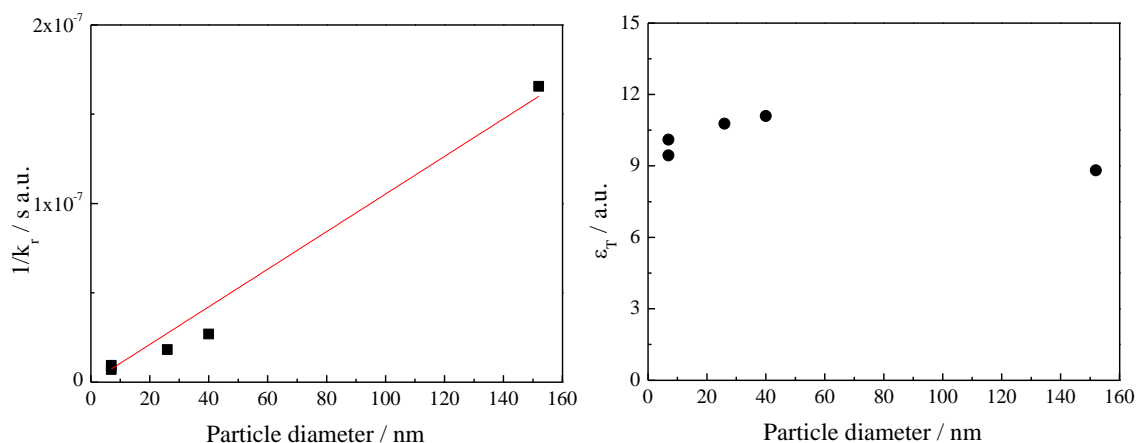
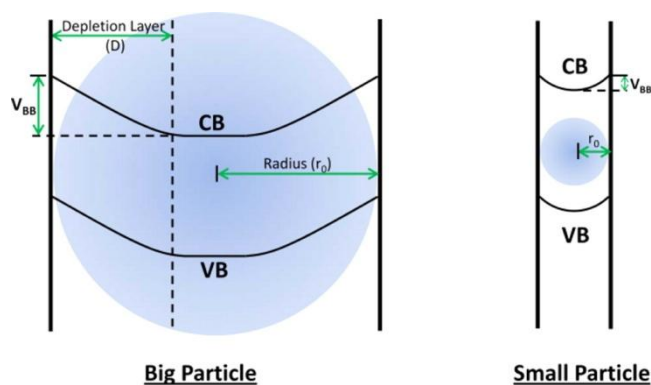


Figure 5.16: (left) Reciprocal second order rate constants k_r and (right) relative extinction coefficients ϵ_T of the trapped holes obtained at 390 nm as the function of the particle diameter for anatase TiO₂. The red line represents a linear fit with a formula: $k_r(390 \text{ nm}) = 1.05 \pm 0.06 \cdot 1/d$



Scheme 5.3: Schematic diagrams of the band bending in big and small particles. Reprinted with permission from ref.¹⁸⁶ Copyright 2012 American Chemical Society.

Upon increasing the particle size the bulk to surface ratio increases, subsequently the distance between the trapped holes and electrons increases. Considering the observed linear dependency of the reciprocal recombination rate constant on the particle diameter equation 5.13 can be further modified as follows:

$$\Delta J = \Delta A = \frac{\epsilon_T' I c_0}{c_0 k_r' / d + 1} + B \quad (5.15)$$

with

$$k_r = k_r' / d \quad (5.16)$$

5. Discussion

Herein, k_r' depends on the wavelength or rather on the region where the trapped electrons and trapped holes absorb. In Figure 5.17 the reciprocal rate constants and the relative extinction coefficients for the transient absorption signals at 450 nm are shown as function of the particle size. Similar to rutile in the anatase particles with diameters exceeding 20 nm the recombination rate constant of the trapped electrons is faster by one order of magnitude than that of the trapped holes. Here all arguments given for the rutile particles are also valid. Moreover, as shown in Figure 4.24 the long-lived transient absorption at 390 nm increases upon increasing the particle size. This can be explained by the fact that due to the band bending effect the number of the long-lived holes increases. As expected, the relative extinction coefficient of the trapped electrons remains constant for all particle sizes studied here (see Figure 5.17 (right)).

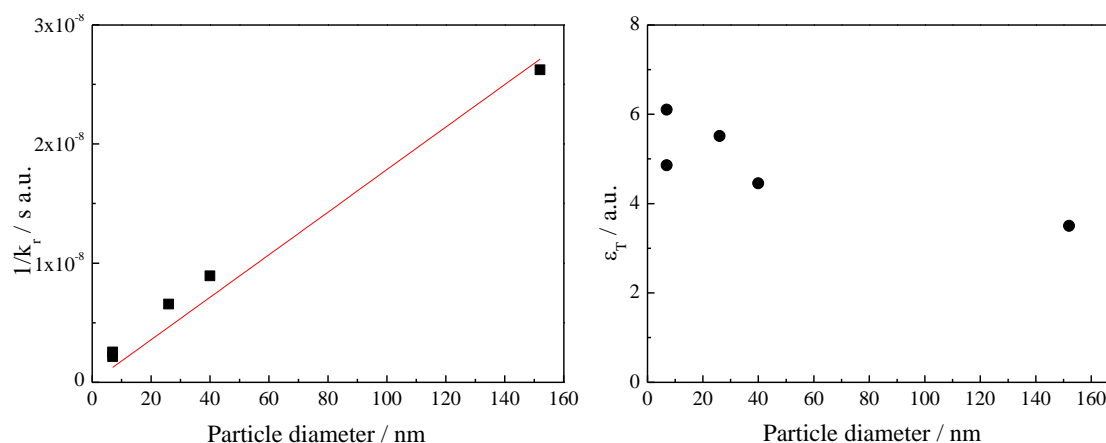


Figure 5.17: (left) Reciprocal second order rate constants k_r and (right) relative extinction coefficients ϵ_T of the trapped holes obtained at 450 nm as the function of the particle diameter for anatase TiO_2 . The red line represents a linear fit with the formula: $k_r(450 \text{ nm}) = 0.18 \pm 0.01 \cdot 1/d$

Similar to anatase also the effect of the particle size on the recombination kinetics of the charge carriers photogenerated in rutile has been analyzed. The comparison of the normalized transient absorption signals at 390 nm, and 410 nm revealed the particle size dependent decay kinetics (see Figure 4.26). In contrast, similar transient absorption spectra have been measured for all rutile samples (see Figure 4.27). The analysis of the recombination rate constant showed that as well as for the trapped holes absorbing at 390 nm (see Figure 5.18 (left)), as for trapped electrons absorbing at 450 nm (see Figure 5.19 (left)) a linear dependency has been observed. Hereby, k_r' at 390 nm is found to be 2.17, while at 450 nm a value of 0.66 is obtained. Such differences between the k_r' values depending on the wavelength can be related to fact that at 390 nm only the recombination

of the trapped holes with the electrons is monitored, while at 450 nm the migration of the electrons from the surface into the bulk competes with this charge carriers recombination.

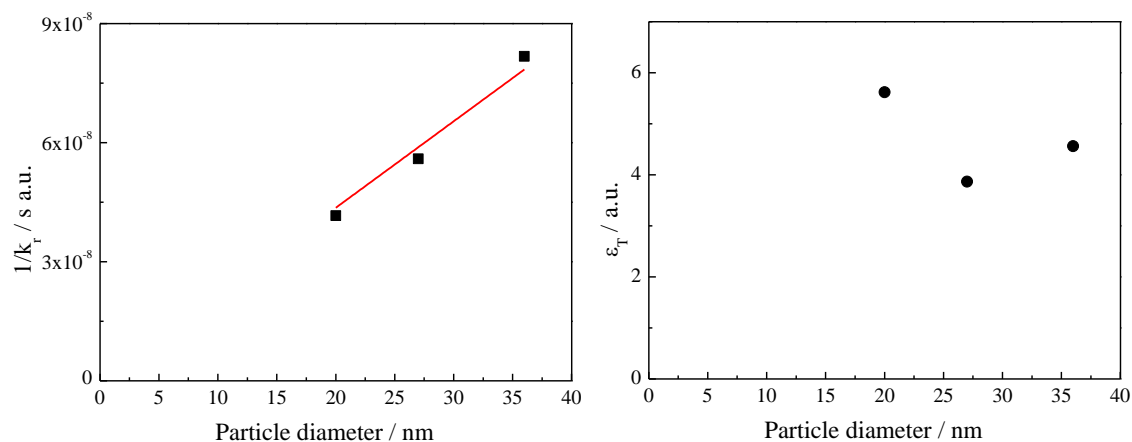


Figure 5.18: (left) Reciprocal second order rate constants k_r and (right) relative extinction coefficients ϵ_T of the trapped holes obtained at 390 nm as a function of the particle diameter for rutile TiO_2 . The red line represents a linear fit with the formula: $k_r(390 \text{ nm}) = 2.17 \pm 0.07 \cdot 1/d$

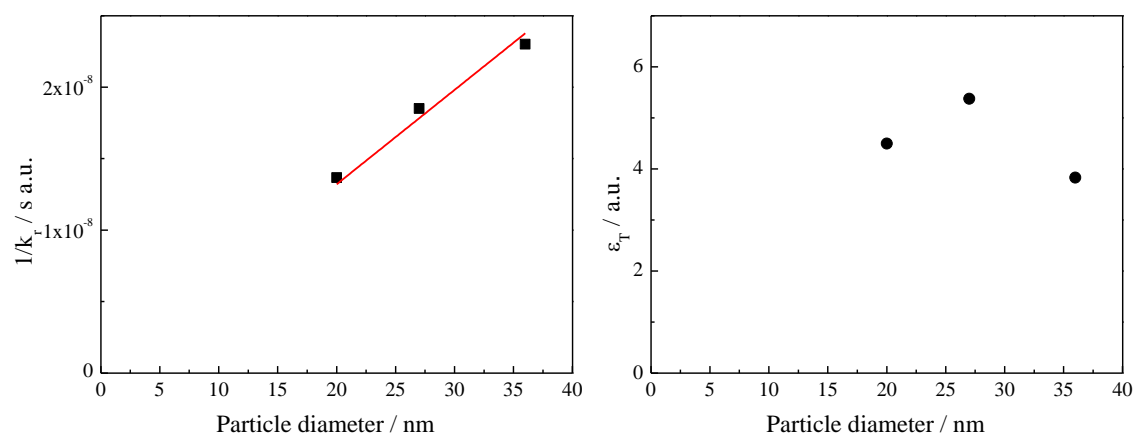


Figure 5.19: (left) Reciprocal second order rate constants k_r and (right) relative extinction coefficients ϵ_T of the trapped holes obtained at 450 nm as a function of the particle diameter for rutile TiO_2 . The red line represents a linear fit with the formula: $k_r(450 \text{ nm}) = 0.66 \pm 0.02 \cdot 1/d$

By comparing the values of k_r for rutile and anatase, it is notable that in case of the former a stronger effect of the particle size on the recombination kinetics of the photogenerated charge carriers is observed. The upward band bending in case of rutile is not only influenced by the particle size but also by the presence of the long-lived Ti^{3+} electrons. Since rutile is easier to reduce than anatase, a stronger upward band bending of rutile in comparison to anatase should occur thus resulting in a better charge carrier separation and hence a larger difference of the recombination rate constants between two particles exhibiting different particle sizes.

5. Discussion

Finally, it is important to correlate the recombination rate constant obtained for the photocatalysts with different particle sizes to their respective photocatalytic activity. A lot of reports have been published explaining different photocatalytic activities in terms of different recombination kinetics, although the latter ones have not been measured. This established fact became a central point of a critical review recently written by Ohtani¹⁹⁰, where he complains: “Thus, “recombination” has been used as an “almighty” card, but at the same time “ghost”, for interpretation of photocatalytic activities without leading to progress in an understanding of photocatalysis and/or photocatalysts, since discussion with the term recombination is just an alternative description of experimental results.” Hence, for example, Pichat *et al.*¹²⁵ attributed the different photocatalytic activity of the anatase TiO₂ samples, which have also been used in the present study, such as PC500, PC105, PC50, and PC10, to the different number of the defects sites, and accordingly, to different electron-hole recombination rates, even though, the latter ones have not been experimentally estimated. However, combining the results obtained by Pichat with the results of the present work it is now possible to correlate the photocatalytic activities and recombination rate constants. For the phenol degradation Pichat *et al.*¹²⁵ reported reaction rates following the order PC500 (d = 7 nm) > PC105(d = 26 nm) > PC50(d = 40 nm) > PC10 (d = 157 nm). This is the order of decreasing recombination rate constants found in the present study. At the first sight this obtained correlation of the results amplifies that in the bigger particles the charge carriers exhibit longer life-time thus leading to the enhanced photocatalytic activities. However, Pichat *et al.* have observed for the pyridine degradation an opposite order of the reaction rates. The authors explained this by the fact that in case of pyridine the surface area plays the dominant role, thus particles with lower surface are less photocatalytically active for the pyridine degradation. These results clearly show that not only the recombination rates determines the photocatalytic activity, but numerous additional effects such as surface area, surface hydroxylation, as well as the pollutant itself due to different degradation mechanisms etc.

6. Summary and conclusions

In contrast to many research reports dealing with the reaction dynamics of the charge carriers photogenerated in transparent films or aqueous suspensions, in the present study the photoinduced processes have been investigated in commercially available TiO₂ powders as well as in the colloidal TiO₂ powder, which has been received from the drying of a self-prepared colloidal TiO₂ suspension and acted as the reference material for better comparison with the reported results.

In this work for the first time, an anatase to rutile phase transition accompanied by the formation of new long-lived Ti³⁺ centers has been experimentally observed during diffuse reflectance laser flash photolysis measurements employing Raman- and EPR-spectroscopy. In case of rutile TiO₂ the presence of these long-lived Ti³⁺ centers has also been proven. The laser-induced modification of the TiO₂ anatase powder involves the following steps: formation of electron-hole pairs followed by an energy and a charge transfer to the TiO₂ lattice, removal of lattice oxygens forming regions at the TiO₂ surface with high defect density thus enhancing the reactivity of the TiO₂ particles and leading to the transition from the anatase to the rutile structure. Additionally, it has been found that the major part of the TiO₂ nanoparticles are able to conduct self-repair processes and therefore exhibit no significant morphological and structural changes at the end of the laser pulse. However, the outcomes of the present study are essential primarily for the interpretation of the transient absorption spectra obtained for different semiconductors. It is of particular importance that the assumption that upon laser excitation no irreversible changes of the studied system occur is not valid anymore at least not for TiO₂. Moreover, it cannot be excluded that such structural changes of TiO₂ also occur during its long illumination times in photocatalytic tests or upon practical applications of photocatalytic materials. Based upon these possible reactions it is most certainly highly indicated to study the role of the surface reorganization initiated by photoinduced reactions in photocatalytic systems. The knowledge of these processes can most certainly open new design pathways for the future photocatalysts.

The analysis of the laser flash photolysis measurements carried out in the present work showed that at lower laser intensities the broad transient absorption spectra of the trapped charge carriers occurred in good agreement with the literature. In contrast, at higher laser intensities and in the case of rutile already at lower laser intensities a strong transient absorption below 450 nm has been observed. The different transient absorption spectra

6. Summary and conclusions

for rutile and anatase obtained under the same experimental conditions have been related to the higher number of the charge carriers photogenerated per rutile nanoparticle exhibiting higher absorption coefficient at the employed laser wavelength than the anatase phase. The respective wavelength regions, where the trapped electrons and holes absorb, were identified employing suitable electron donors and acceptors. Hence, it was possible to determine the transient absorption of which species is influenced more strongly by higher laser exposure that subsequently causes structural changes. In colloidal TiO₂ suspensions as well as in colloidal TiO₂ powder the transient absorption of the trapped holes have been identified to be in the wavelength region between 390 nm and 550 nm, while trapped electrons exhibit the transient absorption signals mainly above 550 nm. In commercial TiO₂ powders, however, the trapped holes show transient absorptions only below 450 nm. This evinces that colloidal particles due to their defect rich surface provide more trapping sites for the photogenerated holes than well crystalline materials such as UV100 and R15. However, taking into account these results and the fact that the observed changes in TiO₂ are most likely complete before the measurement of the transient absorption starts, it is obvious that the presence of the long-lived Ti³⁺ centers formed upon high laser exposure strongly influences the relative extinction coefficient of the trapped holes rather than of the trapped electrons. It is known that the electronic transition and thus the relative extinction coefficient can be influenced by the surrounding electrical field. Hence, the columbic interaction of the trapped holes with long-lived Ti³⁺ centers leads to enhanced relative extinction coefficients of the trapped holes and thus to much higher transient absorption signals below 450 nm rather than in the wavelength region above where the trapped electrons absorb. The linear dependency of the transient absorption at 390 nm on laser intensity found for anatase and rutile supports the thus derived conclusions. Moreover, for the first time this study provided experimental evidence for the fact that the long-lived Ti³⁺ centers contribute to the long lasting transient absorption, as suggested years ago by researchers working in this field.

Employing the laser excitation wavelength of 248 nm it was possible to determine the transient absorption maxima of the trapped holes for anatase and rutile in more detail. Thereby, it could be shown that the holes trapped in anatase absorb at 370 nm while those trapped in rutile absorb at 410 nm. Such a phase dependence of the maxima of the trapped holes has been shown in the present study for the first time. Moreover, due to the shorter penetration depth of the 248 nm laser beam into TiO₂ powder surface much higher charge densities have been produced and thus much stronger structural changes of the thus

excited TiO₂ particles occurred. This results in a decrease of the number of the electrons trapped near the particle surface with the majority of them migrating into its bulk.

The analysis of the decay kinetics revealed that a simple second order rate law could be applied to describe the recombination kinetics of the trapped charge carriers. The observed recombination rate constants - at least in the wavelength range where the trapped electrons absorb - are similar for all three phases exhibiting an order of magnitude of 10⁸ s⁻¹ a.u.⁻¹ in good agreement with respective values reported in the literature. The two anatase samples, that is colloidal TiO₂ powder and Hombikat UV100, showed similar decay kinetics, while for the holes trapped in rutile the decay rate constants were found to be one order of magnitude smaller. This is readily explained by the fact that in rutile structural changes are more easily induced upon illumination, resulting in a stronger influence of the long-lived Ti³⁺ centers on the reaction dynamics. The thus formed Ti³⁺ centers enhance the upward band bending of n-doped TiO₂ resulting in a better charge separation. Hereby, the trapped holes are accumulated at the surface while even the electrons formed close to the surface migrate into the bulk of the particles. These subtle differences in their dynamic properties could also be one of the reasons for the different photocatalytic activities of rutile and anatase. While the former is known as a good oxidant, which can be explained by the longer life-time of the trapped holes, the latter is able to reduce protons more efficiently yielding molecular hydrogen. This could be explained by the presence of a considerably higher number of trapped electrons at the surface of the anatase particles, from where they can be transferred to their reaction partners more easily.

The relative extinction coefficients which are also obtained from the kinetic analysis of the transient absorption decay signals showed a linear dependency on the laser intensity, which is in good agreement with detected structural changes of the TiO₂ materials. Moreover, apparently the effect of the long-lived Ti³⁺ centers on the relative extinction coefficient of the trapped holes does not depend on the TiO₂ morphology. For both, anatase and rutile TiO₂, a similar increase of the extinction coefficient with the employed laser intensity denoted as ε'_T has been found. The exact value of ε'_T , however, depends on the analyzing wavelength.

Finally, a linear correlation between the particle size and the second order recombination rate constants has been established for both, anatase, and rutile. Upon increasing the particle diameter the recombination rate constant decreases. These results

6. Summary and conclusions

are explained employing the band bending model, in which the magnitude of the upward band bending depends on the particle size. Subsequently, in bigger particles, due to the better charge carrier separation and thus due to the longer distance between the trapped electrons and holes, the recombination rate decelerates. The obtained dependency of the particle size on the charge carriers dynamics has been found to be more pronounced in rutile than in anatase which is explained by the stronger structural changes induced in rutile upon laser illumination. Moreover, the obtained relation between the particle size and the recombination rate constant could be successfully applied to explain the respective photocatalytic results reported in the literature.

Based upon the experimentally derived dependencies of the charge carrier dynamics on the laser intensity and on the particle size the following unified second order rate law could be derived:

$$\Delta J = \Delta A = \frac{\varepsilon_r' I c_0}{c_0 k_r' / d t + 1} + B$$

where ε_r' is the laser intensity independent relative relative extinction coefficient, and k_r' is the particle size independent rate constant. While the former depends only on the analyzing wavelength, the later one depends on the TiO₂ phase.

This newly established relationship should allow to describe the reaction dynamics of the charge carriers photogenerated in different photocatalysts and thus to understand the properties of different photocatalyst systems and to specifically develop new photocatalysts with higher activities, longer charge carrier life-times or other improved properties.

7. References

1. Serpone, N.; Emeline, A. V.; Horikoshi, S.; Kuznetsov, V. N.; Ryabchuk, V. K., On the genesis of heterogeneous photocatalysis: A brief historical perspective in the period 1910 to the mid-1980s. *Photochem. Photobiol. Sci.* **2012**, *11*, 1121-1150.
2. Fujishima, A.; Zhang, X.; Tryk, D. A., TiO₂ photocatalysis and related surface phenomena. *Surf. Sci. Rep.* **2008**, *63*, 515-582.
3. Fujishima, A.; Honda, K., Electrochemical photolysis of water at a semiconductor electrode. *Nature* **1972**, *238*, 37-38.
4. Wu, Y.; Lazic, P.; Hautier, G.; Persson, K.; Ceder, G., First principles high throughput screening of oxynitrides for water-splitting photocatalysts. *Energy Environ. Sci.* **2013**, *6*, 157-168.
5. Schneider, J.; Matsuoka, M.; Takeuchi, M.; Zhang, J.; Horiuchi, Y.; Anpo, M.; Bahnemann, D. W., Understanding TiO₂ photocatalysis: Mechanisms and materials. *Chem. Rev.* **2014**, *114*, 9919-9986.
6. Serpone, N.; Lawless, D.; Khairutdinov, R.; Pelizzetti, E., Subnanosecond relaxation dynamics in TiO₂ colloidal sols (particle sizes R(P)=1.0-13.4 nm)- Relevance to heterogeneous photocatalysis. *J. Phys. Chem.* **1995**, *99*, 16655-16661.
7. Bahnemann, D.; Henglein, A.; Lilie, J.; Spanhel, L., Flash-photolysis observation of the absorption spectra of trapped positive holes and electrons in colloidal TiO₂. *J. Phys. Chem.* **1984**, *88*, 709-711.
8. Grätzel, M.; Frank, A. J., Interfacial electron-transfer reactions in colloidal semiconductor dispersions-kinetic-analysis. *J. Phys. Chem.* **1982**, *86*, 2964-2967.
9. Shkrob, I. A.; Sauer, M. C., Hole scavenging and photo-stimulated recombination of electron-hole pairs in aqueous TiO₂ nanoparticles. *J. Phys. Chem. B* **2004**, *108*, 12497-12511.
10. Haque, S. A.; Tachibana, Y.; Willis, R. L.; Moser, J. E.; Grätzel, M.; Klug, D. R.; Durrant, J. R., Parameters influencing charge recombination kinetics in dye-sensitized nanocrystalline titanium dioxide films. *J. Phys. Chem. B* **2000**, *104*, 538-547.
11. Yoshihara, T.; Katoh, R.; Furube, A.; Tamaki, Y.; Murai, M.; Hara, K.; Murata, S.; Arakawa, H.; Tachiya, M., Identification of reactive species in photoexcited nanocrystalline TiO₂ films by wide-wavelength-range (400-2500 nm) transient absorption spectroscopy. *J. Phys. Chem. B* **2004**, *108*, 3817-3823.
12. Yoshihara, T.; Tamaki, Y.; Furube, A.; Murai, M.; Hara, K.; Katoh, R., Effect of pH on absorption spectra of photogenerated holes in nanocrystalline TiO₂ films. *Chem. Phys. Lett.* **2007**, *438*, 268-273.
13. Tamaki, Y.; Furube, A.; Katoh, R.; Murai, M.; Hara, K.; Arakawa, H.; Tachiya, M., Trapping dynamics of electrons and holes in a nanocrystalline TiO₂ film revealed by femtosecond visible/near-infrared transient absorption spectroscopy. *Comptes Rendus Chimie* **2006**, *9*, 268-274.
14. Tamaki, Y.; Hara, K.; Katoh, R.; Tachiya, M.; Furube, A., Femtosecond visible-to-IR spectroscopy of TiO₂ nanocrystalline films: Elucidation of the electron mobility before deep trapping. *J. Phys. Chem. C* **2009**, *113*, 11741-11746.
15. Rothenberger, G.; Moser, J.; Gratzel, M.; Serpone, N.; Sharma, D. K., Charge carrier trapping and recombination dynamics in small semiconductor particles. *J. Am. Chem. Soc.* **1985**, *107*, 8054-8059.
16. Bahnemann, D. W.; Hilgendorff, M.; Memming, R., Charge carrier dynamics at TiO₂ particles: Reactivity of free and trapped holes. *J. Phys. Chem. B* **1997**, *101*, 4265-4275.

7. References

17. Mo, S.-D.; Ching, W. Y., Electronic and optical properties of three phases of titanium dioxide: Rutile, anatase, and brookite. *Phys. Rev. B* **1995**, *51*, 13023-13032.
18. Pascual, J.; Camassel, J.; Mathieu, H., Fine structure in the intrinsic absorption edge of TiO₂. *Phys. Rev. B* **1978**, *18*, 5606-5614.
19. Tang, H.; Berger, H.; Schmid, P. E.; Levy, F.; Burri, G., Photoluminescence in TiO₂ anatase single crystals. *Solid State Commun.* **1993**, *87*, 847-850.
20. Kandiel, T. A.; Feldhoff, A.; Robben, L.; Dillert, R.; Bahnemann, D. W., Tailored titanium dioxide nanomaterials: Anatase nanoparticles and brookite nanorods as highly active photocatalysts. *Chem. Mater.* **2010**, *22*, 2050-2060.
21. Rossetti, R.; Ellison, J. L.; Gibson, J. M.; Brus, L. E., Size effects in the excited electronic states of small colloidal CdS crystallites. *J. Chem. Phys.* **1984**, *80*, 4464-4469.
22. Kormann, C.; Bahnemann, D. W.; Hoffmann, M. R., Preparation and characterization of quantum-size titanium-dioxide. *J. Phys. Chem.* **1988**, *92*, 5196-5201.
23. Bahnemann, D. W.; Kormann, C.; Hoffmann, M. R., Preparation and characterization of quantum size zinc oxide - A detailed spectroscopic study. *J. Phys. Chem.* **1987**, *91*, 3789-3798.
24. Lindan, P. J. D.; Harrison, N. M.; Gillan, M. J.; White, J. A., First-principles spin-polarized calculations on the reduced and reconstructed TiO₂ (110) surface. *Phys. Rev. B* **1997**, *55*, 15919-15927.
25. Chretien, S.; Metiu, H., Electronic structure of partially reduced rutile TiO₂(110) surface: Where are the unpaired electrons located? *J. Phys. Chem. C* **2011**, *115*, 4696-4705.
26. Diebold, U., The surface science of titanium dioxide. *Surf. Sci. Rep.* **2003**, *48*, 53-229.
27. Nowotny, M. K.; Sheppard, L. R.; Bak, T.; Nowotny, J., Defect chemistry of titanium dioxide. Application of defect engineering in processing of TiO₂-based photocatalysts. *J. Phys. Chem. C* **2008**, *112*, 5275-5300.
28. Henderson, M. A., A surface science perspective on TiO₂ photocatalysis. *Surf. Sci. Rep.* **2011**, *66*, 185-297.
29. Enright, B.; Fitzmaurice, D., Spectroscopic determination of electron and hole effective masses in a nanocrystalline semiconductor film. *J. Phys. Chem.* **1996**, *100*, 1027-1035.
30. Lantz, J. M.; Corn, R. M., Time-resolved optical 2nd-harmonic generation measurements of picosecond band flattening processes at single-crystal TiO₂ electrodes *J. Phys. Chem.* **1994**, *98*, 9387-9390.
31. Di Valentin, C.; Selloni, A., Bulk and surface polarons in photoexcited anatase TiO₂. *J. Phys. Chem. Lett.* **2011**, *2*, 2223-2228.
32. Yang, X. J.; Tamai, N., How fast is interfacial hole transfer? In situ monitoring of carrier dynamics in anatase TiO₂ nanoparticles by femtosecond laser spectroscopy. *PCCP* **2001**, *3*, 3393-3398.
33. Tamaki, Y.; Furube, A.; Murai, M.; Hara, K.; Katoh, R.; Tachiya, M., Dynamics of efficient electron-hole separation in TiO₂ nanoparticles revealed by femtosecond transient absorption spectroscopy under the weak-excitation condition. *PCCP* **2007**, *9*, 1453-1460.
34. Skinner, D. E.; Colombo, D. P.; Cavaleri, J. J.; Bowman, R. M., Femtosecond investigation of electron trapping in semiconductor nanoclusters. *J. Phys. Chem.* **1995**, *99*, 7853-7856.
35. Hoffmann, M. R.; Martin, S. T.; Choi, W.; Bahnemann, D. W., Environmental applications of semiconductor photocatalysis. *Chem. Rev.* **1995**, *95*, 69-96.

36. Nowotny, M. K.; Bogdanoff, P.; Dittrich, T.; Fiechter, S.; Fujishima, A.; Tributsch, H., Observations of p-type semiconductivity in titanium dioxide at room temperature. *Mater. Lett.* **2010**, *64*, 928-930.
37. Jaeger, C. D.; Bard, A. J., Spin trapping and electron-spin resonance detection of radical intermediates in the photo-decomposition of water at TiO₂ particulate systems. *J. Phys. Chem.* **1979**, *83*, 3146-3152.
38. Anpo, M.; Shima, T.; Kubokawa, Y., Electron-spin-resonance and photoluminescence evidence for the photocatalytic formation of hydroxyl radicals on small TiO₂ particles. *Chem. Lett.* **1985**, 1799-1802.
39. Lawless, D.; Serpone, N.; Meisel, D., Role of OH radicals and trapped holes in photocatalysis-A pulse radiolysis study. *J. Phys. Chem.* **1991**, *95*, 5166-5170.
40. Kim, W.; Tachikawa, T.; Moon, G. H.; Majima, T.; Choi, W., Molecular-level understanding of the photocatalytic activity difference between anatase and rutile nanoparticles. *Angew. Chem. Int. Ed.* **2014**, *53*, 14036-14041.
41. Berger, T.; Sterrer, M.; Diwald, O.; Knozinger, E.; Panayotov, D.; Thompson, T. L.; Yates, J. T., Light-induced charge separation in anatase TiO₂ particles. *J. Phys. Chem. B* **2005**, *109*, 6061-6068.
42. Micic, O. I.; Zhang, Y. N.; Cromack, K. R.; Trifunac, A. D.; Thurnauer, M. C., Trapped holes on TiO₂ colloids studied by electron-paramagnetic-resonance. *J. Phys. Chem.* **1993**, *97*, 7277-7283.
43. Ishibashi, K.; Fujishima, A.; Watanabe, T.; Hashimoto, K., Quantum yields of active oxidative species formed on TiO₂ photocatalyst. *J. Photochem. Photobiol. A* **2000**, *134*, 139-142.
44. Howe, R. F.; Gratzel, M., Electron-paramagnetic-resonance study of hydrated anatase under UV irradiation. *J. Phys. Chem.* **1987**, *91*, 3906-3909.
45. Zhang, H. Z.; Penn, R. L.; Hamers, R. J.; Banfield, J. F., Enhanced adsorption of molecules on surfaces of nanocrystalline particles. *J. Phys. Chem. B* **1999**, *103*, 4656-4662.
46. Jug, K.; Nair, N. N.; Bredow, T., Reaction of surface hydroxyl groups with VO₄H₃ on anatase surfaces. *Surf. Sci.* **2005**, *596*, 108-116.
47. Shapovalov, V.; Stefanovich, E. V.; Truong, T. N., Nature of the excited states of the rutile TiO₂(110) surface with adsorbed water. *Surf. Sci.* **2002**, *498*, L103-L108.
48. Ji, Y. F.; Wang, B.; Luo, Y., Location of trapped hole on rutile-TiO₂(110) surface and its role in water oxidation. *J. Phys. Chem. C* **2012**, *116*, 7863-7866.
49. Hug, G. L., *Optical spectra of nonmetallic inorganic transient species in aqueous solution*. NSRDS-NBS: 1981; Vol. 69.
50. Arbour, C.; Sharma, D. K.; Langford, C. H., Picosecond flash spectroscopy of TiO₂ colloids with adsorbed dyes. *J. Phys. Chem.* **1990**, *94*, 331-335.
51. Peiro, A. M.; Colombo, C.; Doyle, G.; Nelson, J.; Mills, A.; Durrant, J. R., Photochemical reduction of oxygen adsorbed to nanocrystalline TiO₂ films: A transient absorption and oxygen scavenging study of different TiO₂ preparations. *J. Phys. Chem. B* **2006**, *110*, 23255-23263.
52. Katoh, R.; Furube, A.; Yamanaka, K.; Morikawa, T., Charge separation and trapping in N-doped TiO₂ photocatalysts: A time-resolved microwave conductivity study. *J. Phys. Chem. Lett.* **2010**, *1*, 3261-3265.
53. Tang, J.; Cowan, A. J.; Durrant, J. R.; Klug, D. R., Mechanism of O₂ production from water splitting: Nature of charge carriers in nitrogen doped nanocrystalline TiO₂ films and factors limiting O₂ production. *J. Phys. Chem. C* **2011**, *115*, 3143-3150.

7. References

54. Jing, L.; Zhou, J.; Durrant, J. R.; Tang, J.; Liu, D.; Fu, H., Dynamics of photogenerated charges in the phosphate modified TiO₂ and the enhanced activity for photoelectrochemical water splitting. *Energy Environ. Sci.* **2012**, *5*, 6552-6558.
55. Tachikawa, T.; Tojo, S.; Kawai, K.; Endo, M.; Fujitsuka, M.; Ohno, T.; Nishijima, K.; Miyamoto, Z.; Majima, T., Photocatalytic oxidation reactivity of holes in the sulfur- and carbon-doped TiO₂ powders studied by time-resolved diffuse reflectance spectroscopy. *J. Phys. Chem. B* **2004**, *108*, 19299-19306.
56. Murakami, Y.; Nishino, J.; Mesaki, T.; Nosaka, Y., Femtosecond diffuse-reflectance spectroscopy of various commercially available TiO₂ powders. *Spectrosc. Lett.* **2011**, *44*, 88-94.
57. Zawadzki, P., Absorption spectra of trapped holes in anatase TiO₂. *J. Phys. Chem. C* **2013**, *117*, 8647-8651.
58. Knorr, F. J.; Mercado, C. C.; McHale, J. L., Trap-state distributions and carrier transport in pure and mixed-phase TiO₂: Influence of contacting solvent and interphasial electron transfer. *J. Phys. Chem. C* **2008**, *112*, 12786-12794.
59. Bredow, T.; Jug, K., Sinda1 study of photocatalytic formation and reactions of OH radicals at anatase particles. *J. Phys. Chem.* **1995**, *99*, 285-291.
60. Kowalski, P. M.; Camellone, M. F.; Nair, N. N.; Meyer, B.; Marx, D., Charge localization dynamics Induced by oxygen vacancies on the TiO₂(110) Surface. *Phys. Rev. Lett.* **2010**, *105*.
61. Di Valentin, C.; Pacchioni, G.; Selloni, A., Electronic structure of defect states in hydroxylated and reduced rutile TiO₂(110) surfaces. *Phys. Rev. Lett.* **2006**, *97*.
62. Martin, S. T.; Herrmann, H.; Choi, W. Y.; Hoffmann, M. R., Time-resolved microwave conductivity.1. TiO₂ photoreactivity and size quantization. *J. Chem. Soc., Faraday Trans.* **1994**, *90*, 3315-3322.
63. Martin, S. T.; Herrmann, H.; Hoffmann, M. R., Time-resolved microwave conductivity.2. Quantum-sized TiO₂ and the effect of adsorbates and lieght-intensity on charge-carrier dynamics. *J. Chem. Soc., Faraday Trans.* **1994**, *90*, 3323-3330.
64. Zhu, M.; Mi, Y.; Zhu, G.; Li, D.; Wang, Y.; Weng, Y., Determiation of midgap state energy levels of an anatase TiO₂ nanocrystal film by nanosecond transient infrared absorption excitation energy scanning spectra. *J. Phys. Chem. C* **2013**, *117*, 18863-18869.
65. Katoh, R.; Furube, A., Tunneling-type charge recombination in nanocrystalline TiO₂ films at low temperature. *J. Phys. Chem. Lett.* **2011**, *2*, 1888-1891.
66. Kuznetsov, A. I.; Kameneva, O.; Alexandrov, A.; Bityurin, N.; Marteau, P.; Chhor, K.; Sanchez, C.; Kanaev, A., Light-induced charge separation and storage in titanium oxide gels. *Phys. Rev. E* **2005**, *71*.
67. Yamakata, A.; Ishibashi, T.; Onishi, H., Time-resolved infrared absorption spectroscopy of photogenerated electrons in platinized TiO₂ particles. *Chem. Phys. Lett.* **2001**, *333*, 271-277.
68. Haque, S. A.; Tachibana, Y.; Willis, R. L.; Moser, J. E.; Gratzel, M.; Klug, D. R.; Durrant, J. R., Parameters influencing charge recombination kinetics in dye-sensitized nanocrystalline titanium dioxide films. *J. Phys. Chem. B* **2000**, *104*, 538-547.
69. Colombo, D. P.; Bowman, R. M., Does interfacial charge transfer compete with charge carrier recombination? A femtosecond diffuse reflectance investigation of TiO₂ nanoparticles. *J. Phys. Chem.* **1996**, *100*, 18445-18449.
70. Wang, X.; Kafizas, A.; Li, X.; Moniz, S. J. A.; Reardon, P. J. T.; Tang, J.; Parkin, I. P.; Durrant, J. R., Transient absorption spectroscopy of anatase and rutile: The impact of morphology and phase on photocatalytic activity. *J. Phys. Chem. C* **2015**, *119*, 10439-10447.

71. Murakami, S. Y.; Kominami, H.; Kera, Y.; Ikeda, S.; Noguchi, H.; Uosaki, K.; Ohtani, B., Evaluation of electron-hole recombination properties of titanium(IV) oxide particles with high photocatalytic activity. *Res. Chem. Intermed.* **2007**, *33*, 285-296.
72. Colombo, D. P.; Bowman, R. M., Femtosecond diffuse reflectance spectroscopy of TiO₂ powders. *J. Phys. Chem.* **1995**, *99*, 11752-11756.
73. Furube, A.; Asahi, T.; Masuhara, H.; Yamashita, H.; Anpo, M., Charge carrier dynamics of standard TiO₂ catalysts revealed by femtosecond diffuse reflectance spectroscopy. *J. Phys. Chem. B* **1999**, *103*, 3120-3127.
74. Grela, M. A.; Colussi, A. J., Kinetics of stochastic charge transfer and recombination events in semiconductor colloids. Relevance to photocatalysis efficiency. *J. Phys. Chem.* **1996**, *100*, 18214-18221.
75. Cavaleri, J. J.; Colombo, D. P.; Bowman, R. M., Ultrafast charge carrier dynamics of SnO₂ nanoclusters: A refined interpretation of the electron and hole kinetics in metal oxides. *J. Phys. Chem.* **1998**, *102*, 1341-1346.
76. Salvador, P., On the nature of photogenerated radical species active in the oxidative degradation of dissolved pollutants with TiO₂ aqueous suspensions: A revision in the light of the electronic structure of adsorbed water. *J. Phys. Chem. C* **2007**, *111*, 17038-17043.
77. Imanishi, A.; Okamura, T.; Ohashi, N.; Nakamura, R.; Nakato, Y., Mechanism of water photooxidation reaction at atomically flat TiO₂ (rutile) (110) and (100) surfaces: Dependence on solution pH. *J. Am. Chem. Soc.* **2007**, *129*, 11569-11578.
78. Gao, R. M.; Safrany, A.; Rabani, J., Reactions of TiO₂ excess electron in nanocrystallite aqueous solutions studied in pulse and gamma-radiolytic systems. *Radiat. Phys. Chem.* **2003**, *67*, 25-39.
79. Hush, N. S., Adiabatic theory of outer sphere electron-transfer reactions in solution. *Trans. Faraday Soc.* **1961**, *57*, 557-580.
80. Marcus, R. A., Chemical and electrochemical electron-transfer theory. *Annu. Rev. Phys. Chem.* **1964**, *15*, 155-196.
81. Furube, A.; Asahi, T.; Masuhara, H.; Yamashita, H.; Anpo, M., Direct observation of a picosecond charge separation process in photoexcited platinum-loaded TiO₂ particles by femtosecond diffuse reflectance spectroscopy. *Chem. Phys. Lett.* **2001**, *336*, 424-430.
82. Iwata, K.; Takaya, T.; Hamaguchi, H.; Yamakata, A.; Ishibashi, T. A.; Onishi, H.; Kuroda, H., Carrier dynamics in TiO₂ and Pt/TiO₂ powders observed by femtosecond time-resolved near-infrared spectroscopy at a spectral region of 0.9-1.5 μm with the direct absorption method. *J. Phys. Chem. B* **2004**, *108*, 20233-20239.
83. Anpo, M.; Takeuchi, M., The design and development of highly reactive titanium oxide photocatalysts operating under visible light irradiation. *J. Catal.* **2003**, *216*, 505-516.
84. Tamaki, Y.; Furube, A.; Murai, M.; Hara, K.; Katoh, R.; Tachiya, M., Direct observation of reactive trapped holes in TiO₂ undergoing photocatalytic oxidation of adsorbed alcohols: Evaluation of the reaction rates and yields. *J. Am. Chem. Soc.* **2006**, *128*, 416-417.
85. Memming, R., Electron transfer I. Mattay, J., Ed. Springer-Verlag: Berlin Heidelberg 1994; Vol. 169.
86. Nakabayashi, S.; Komuro, S.; Aoyagi, Y.; Kira, A., Transient grating method applied to electron-transfer dynamics at a semiconductor liquid interface. *J. Phys. Chem.* **1987**, *91*, 1696-1698.
87. Hykaway, N.; Sears, W. M.; Morisaki, H.; Morrison, S. R., Current-doubling reactions on titanium dioxide photoanodes. *J. Phys. Chem.* **1986**, *90*, 6663-6667.

7. References

88. Furube, A.; Asahi, T.; Masuhara, H.; Yamashita, H.; Anpo, M., Direct observation of interfacial hole transfer from a photoexcited TiO₂ particle to an adsorbed molecule SCN⁻ by femtosecond diffuse reflectance spectroscopy. *Res. Chem. Intermed.* **2001**, *27*, 177-187.
89. Draper, R. B.; Fox, M. A., Titanium-dioxide photosensitized reactions studied by diffuse reflectance flash-photolysis in aqueous suspensions of TiO₂ powder. *Langmuir* **1990**, *6*, 1396-1402.
90. Draper, R. B.; Fox, M. A., Titanium-dioxide photooxidation of thiocyanate (SCN)²⁻ - Studied by diffuse reflectance flash-photolysis. *J. Phys. Chem.* **1990**, *94*, 4628-4634.
91. Gottfried Wilhelm Leibniz University of Hannover, 2010; pp Rietveld refined powder X-ray diffraction (XRD) measurements were carried out for the identification of the constituting polymorph and the calculation of the mean crystalline domain which is usually used as the particle size. The measurements were carried out on a Bruker D4 Endeavour diffractometer (Cu Ka radiation, Ni filtered).
92. Gottfried Wilhelm Leibniz University of Hannover Institute for Technical Chemistry, 2010; pp Single-point standard surface area measurements were carried out employing a Micromeritics AutoMate 23 instrument. The gas mixture used for the adsorption determinations was 30% nitrogen and 70% helium. The TiO₂ samples were previously heated to 150 °C for approximately 30 min in order to clean the surface of adsorbed organic compounds and humidity. Desorption determinations were also performed in order to confirm the data obtained from the adsorption measurements.
93. Porter, G., *Flash photolysis and spectroscopy. A new method for the study of free radical reactions.* 1950; Vol. 200, p 284-300.
94. Kessler, R. W.; Krabichler, G.; Uhl, S.; Oelkrug, D.; Hagan, W. P.; Hyslop, J.; Wilkinson, F., Transient decay following pulse excitation of diffuse scattering samples. *Opt. Acta: Inter. J. Opt.* **1983**, *30*, 1099-1111.
95. Hagfeldt, A.; Gratzel, M., Light-induced redox reactions in nanocrystalline systems. *Chem. Rev.* **1995**, *95*, 49-68.
96. Kamat, P. V., Photochemistry on nonreactive and reactive (semiconductors) surfaces. *Chem. Rev.* **1993**, *93*, 267-300.
97. Kessler, R. W.; Wilkinson, F., Diffuse reflectance triplet-triplet absorption spectroscopy of aromatic hydrocarbons chemisorbed on [gamma]-alumina. *J. Chem. Soc., Faraday Trans. 1: Phys. Chem. in Cond. Phases* **1981**, *77*, 309-320.
98. Wilkinson, F., Diffuse reflectance flash photolysis. *J. Chem. Soc., Faraday Trans. 2: Molec. Chem. Phys.* **1986**, *82*, 2073-2081.
99. Wilkinson, F.; Willsher, C. J., The use of diffuse reflectance laser flash photolysis to study primary photoprocesses in anisotropic media. *Tetrahedron* **1987**, *43*, 1197-1209.
100. Willsher, C. J., The study of transient absorptions in optically dense materials by diffuse reflectance laser flash photolysis. *J. Photochem.* **1985**, *28*, 229-236.
101. Wilkinson, F.; Kelly, G. P.; Anpo, M.; Matsuura, T., Laser flash photolysis on solid surfaces. In *Stud. Surf. Sci. Catal.*, Elsevier: 1989; Vol. Volume 47, pp 30-47.
102. Kubelka, P.; Munk, F., Ein Beitrag zur Optik der Farbanstriche. *Zeitschrift für Technische Physik* **1931**, *12*, 593.
103. Lin, T.-P.; Kan, H. K. A., Calculation of reflectance of a light diffuser with nonuniform absorption. *J. Opt. Soc. Am.* **1970**, *60*, 1252-1256.
104. Zhang, W. F.; He, Y. L.; Zhang, M. S.; Yin, Z.; Chen, Q., Raman scattering study on anatase TiO₂ nanocrystals. *J. Phys. D: Appl. Phys.* **2000**, *33*, 912.
105. Zhang, M.-S.; Yin, Z.; Chen, Q.; Xijun, W.; Xiaoli, J., Raman scattering by nanophase titanium dioxide. *Ferroelectrics* **1995**, *168*, 131-137.

106. Parker, J.; Siegel, R., Raman microprobe study of nanophase TiO₂ and oxidation-induced spectral changes. *J. Mater. Res.* **1990**, *5*, 1246-1252.
107. Balachandran, U.; Eror, N., Raman spectra of titanium dioxide. *J. Solid State Chem.* **1982**, *42*, 276-282.
108. Parker, J.; Siegel, R., Calibration of the raman spectrum to the oxygen stoichiometry of nanophase TiO₂. *Appl. Phys. Lett.* **1990**, *57*, 943-945.
109. Khomenko, V.; Langer, K.; Rager, H.; Fett, A., Electronic absorption by Ti³⁺ ions and electron delocalization in synthetic blue rutile. *Phys. Chem. Miner.* **1998**, *25*, 338-346.
110. Howe, R. F.; Grätzel, M., Electron-paramagnetic-resonance observation of trapped electrons in colloidal TiO₂. *J. Phys. Chem.* **1985**, *89*, 4495-4499.
111. Berger, T.; Sterrer, M.; Diwald, O.; Knözinger, E., Charge trapping and photoadsorption of O²⁻ on dehydroxylated TiO₂ nanocrystals - An electron paramagnetic resonance study. *Chemphyschem* **2005**, *6*, 2104-2112.
112. Priebe, J. B.; Radnik, J. r.; Lennox, A. J.; Pohl, M.-M.; Karnahl, M.; Hollmann, D.; Grabow, K.; Bentrup, U.; Junge, H.; Beller, M., Solar hydrogen production by plasmonic Au/TiO₂ catalysts: Impact of synthesis protocol and TiO₂ phase on charge transfer efficiency and H₂ evolution rates. *Acs Catalysis* **2015**, *5*, 2137-2148.
113. Naldoni, A.; Allieta, M.; Santangelo, S.; Marelli, M.; Fabbri, F.; Cappelli, S.; Bianchi, C. L.; Psaro, R.; Dal Santo, V., Effect of nature and location of defects on bandgap narrowing in black TiO₂ nanoparticles. *J. Am. Chem. Soc.* **2012**, *134*, 7600-7603.
114. Katoh, R.; Murai, M.; Furube, A., Transient absorption spectra of nanocrystalline TiO₂ films at high excitation density. *Chem. Phys. Lett.* **2010**, *500*, 309-312.
115. Tang, J. W.; Durrant, J. R.; Klug, D. R., Mechanism of photocatalytic water splitting in TiO₂. Reaction of water with photoholes, importance of charge carrier dynamics, and evidence for four-hole chemistry. *J. Am. Chem. Soc.* **2008**, *130*, 13885-13891.
116. Kim, W.; Tachikawa, T.; Moon, G.-h.; Majima, T.; Choi, W., Molecular-Level Understanding of the Photocatalytic Activity Difference between Anatase and Rutile Nanoparticles. *Angew. Chem. Int. Ed.* **2014**, *53*, 14036-14041.
117. Kowalska, E.; Remita, H.; Colbeau-Justin, C.; Hupka, J.; Belloni, J., Modification of titanium dioxide with platinum ions and clusters: Application in photocatalysis. *J. Phys. Chem. C* **2008**, *112*, 1124-1131.
118. Tafalla, D.; Salvador, P., Mechanisms of charge transfer at the semiconductor-electrolyte interface: Oxygen electroreduction at naked and platinized n-TiO₂ electrodes. *Ber. Bunsenges. Phys. Chem.* **1987**, *91*, 475-479.
119. Sudha, D.; Sivakumar, P., Review on the photocatalytic activity of various composite catalysts. 2015; Vol. 97, pp 112-133.
120. Li, Z.; Liu, R.; Xu, Y., Larger effect of sintering temperature than particle size on the photocatalytic activity of anatase TiO₂. *J. Phys. Chem. C* **2013**, *117*, 24360-24367.
121. Wang, X.; SÄ, L.; Su, R.; Wendt, S.; Hald, P.; Mamakhel, A.; Yang, C.; Huang, Y.; Iversen, B. B.; Besenbacher, F., The influence of crystallite size and crystallinity of anatase nanoparticles on the photo-degradation of phenol. In *Special issue on Photocatalysis and Photoelectrolysis*, 2014; Vol. 310, pp 100-108.
122. Serpone, N.; Lawless, D.; Khairutdinov, R., Size effects on the photophysical properties of colloidal anatase TiO₂ particles-size quantization or direct transitions in this indirect semiconductor. *J. Phys. Chem.* **1995**, *99*, 16646-16654.
123. Pichat, P.; Courbon, H.; Enriquez, R.; Tan, T. T. Y.; Amal, R., Light-induced isotopic exchange between O₂ and semiconductor oxides, a characterization method that deserves not to be overlooked. *Res. Chem. Intermed.* **2007**, *33*, 239-250.

7. References

124. Enriquez, R.; Pichat, P., Different net effect of TiO₂ sintering temperature on the photocatalytic removal rates of 4-chlorophenol, 4-chlorobenzoic acid and dichloroacetic acid in water. *J. Environ. Sci. and Health, Part A* **2006**, *41*, 955-966.
125. Agrios, A. G.; Pichat, P., Recombination rate of photogenerated charges versus surface area: Opposing effects of TiO₂ sintering temperature on photocatalytic removal of phenol, anisole, and pyridine in water. *J. Photochem. Photobio. A: Chem.* **2006**, *180*, 130-135.
126. Mendive, C. B., Effects of the UV(A) light on chemical reactions at the interface metal oxide / aqueous solution. San Martin, 2007; p 244.
127. Zhou, Y.; Fichthorn, K. A., Microscopic view of nucleation in the anatase-to-rutile transformation. *J. Phys. Chem. C* **2012**, *116*, 8314-8321.
128. Lee, H. Y.; Lan, W. L.; Tseng, T. Y.; Hsu, D.; Chang, Y. M.; Lin, J. G., Optical control of phase transformation in Fe-doped TiO₂ nanoparticles. *Nanotechnology* **2009**, *20*, 315702.
129. Ma, H. L.; Yang, J. Y.; Dai, Y.; Zhang, Y. B.; Lu, B.; Ma, G. H., Raman study of phase transformation of TiO₂ rutile single crystal irradiated by infrared femtosecond laser. *Appl. Surf. Sci.* **2007**, *253*, 7497-7500.
130. Wilkinson, F.; Willsher, C. J.; Uhl, S.; Honnen, W.; Oelkrug, D., Optical detection of a photoinduced thermal transient in titanium dioxide powder by diffuse reflectance laser flash photolysis. *J. Photochem.* **1986**, *33*, 273-278.
131. Hanaor, D. A. H.; Sorrell, C. C., Review of the anatase to rutile phase transformation. *J. Mater. Sci.* **2011**, *46*, 855-874.
132. Stopper, K.; Dohrmann, J. K., Laser-induced reactions on 2.4-nm colloidal TiO₂ particles in aqueous solution: A study by time-resolved optoacoustic calorimetry. *Z. Phys. Chem.* **2000**, *214*, 555-572.
133. Ricci, P. C.; Carbonaro, C. M.; Stagi, L.; Salis, M.; Casu, A.; Enzo, S.; Delogu, F., Anatase-to-rutile phase transition in TiO₂ nanoparticles irradiated by visible light. *J. Phys. Chem. C* **2013**, *117*, 7850-7857.
134. Ricci, P. C.; Casu, A.; Salis, M.; Corpino, R.; Anedda, A., Optically controlled phase variation of TiO₂ nanoparticles. *J. Phys. Chem. C* **2010**, *114*, 14441-14445.
135. Mezheny, S.; Maksymovych, P.; Thompson, T. L.; Diwald, O.; Stahl, D.; Walck, S. D.; Yates Jr, J. T., STM studies of defect production on the TiO₂(1 1 0) and TiO₂(1 1 0) surfaces induced by UV irradiation. *Chem. Phys. Lett.* **2003**, *369*, 152-158.
136. Stagi, L.; Carbonaro, C. M.; Corpino, R.; Chiriu, D.; Ricci, P. C., Light induced TiO₂ phase transformation: Correlation with luminescent surface defects. *Physica Status Solidi (B)* **2014**, *252*, 124-129.
137. Vasquez, G. C.; Peche-Herrero, M. A.; Maestre, D.; Gianoncelli, A.; Ramirez-Castellanos, J.; Cremades, A.; Gonzalez-Calbet, J. M.; Piqueras, J., Laser-induced anatase-to-rutile transition in TiO₂ nanoparticles: promotion and inhibition effects by Fe and Al doping and achievement of micropatterning. *J. Phys. Chem. C* **2015**, *119*, 11965-11974.
138. Zhang, J.; Li, M.; Feng, Z.; Chen, J.; Li, C., UV raman spectroscopic study on TiO₂. I. Phase transformation at the surface and in the bulk. *J. Phys. Chem. B* **2006**, *110*, 927-935.
139. Diebold, U.; Lehman, J.; Mahmoud, T.; Kuhn, M.; Leonardelli, G.; Hebenstreit, W.; Schmid, M.; Varga, P., Intrinsic defects on a TiO₂(110) surface and their reaction with oxygen: a scanning tunneling microscopy study. *Surf. Sci.* **1998**, *411*, 137-153.
140. Penn, R. L.; Banfield, J. F., Formation of rutile nuclei at anatase {112} twin interfaces and the phase transformation mechanism in nanocrystalline titania. *Am. Mineral.* **1999**, *84*, 871-876.

141. Forsgren, J.; Paz, M. D.; Leon, B.; Engqvist, H., Laser induced surface structuring and ion conversion in the surface oxide of titanium: Possible implications for the wettability of laser treated implants. *J. Mat. Sci.: Mat. in Med.* **2013**, *24*, 11-15.
142. Henglein, A. W., H., Photochemical energy conversion. Norris, J. R., Meisel, D., Ed. Elsevier: New York, 1989; pp. 161-172.
143. Ghosh, A. K.; Wakim, F. G.; Addiss, R. R., Photoelectronic processes in rutile. *Phys. Rev.* **1969**, *184*, 979-988.
144. Ahmed, A. Y.; Kandiel, T. A.; Oekermann, T.; Bahnemann, D., Photocatalytic activities of different well-defined single crystal TiO₂ surfaces: Anatase versus rutile. *J. Phys. Chem. Lett.* **2011**, *2*, 2461-2465.
145. Lisachenko, A. A., Photon-driven electron and atomic processes on solid-state surface in photoactivated spectroscopy and photocatalysis. *J. Photochem. Photobio. A: Chem.* **2008**, *196*, 127-137.
146. Terenin, A. N., *Uchenye zapiski LGU (rus)* **1939**, *5*, 26-40.
147. Zhang, Z.; Yates, J. T., Direct observation of surface-mediated electron-hole pair recombination in TiO₂(110). *J. Phys. Chem. C* **2010**, *114*, 3098-3101.
148. Yates, J. T., Photochemistry on TiO₂: Mechanisms behind the surface chemistry. *Surf. Sci.* **2009**, *603*, 1605-1612.
149. Thompson, T. L.; Yates, J. T., Monitoring hole trapping in photoexcited TiO₂(110) using a surface photoreaction. *J. Phys. Chem. B* **2005**, *109*, 18230-18236.
150. Salvador, P., Mechanisms of water photooxidation at n-TiO₂ rutile single crystal oriented electrodes under UV illumination in competition with photocorrosion. *Prog. Surf. Sci.* **2011**, *86*, 41-58.
151. Courbon, H.; Formenti, M.; Pichat, P., Study of oxygen isotopic exchange over UV irradiated anatase samples and comparison with photooxidation of isobutane into acetone. *J. Phys. Chem.* **1977**, *81*, 550-554.
152. Courbon, H.; Pichat, P., Occurrence and mechanism of oxygen isotopic exchange catalyzed by UV irradiated SnO₂, ZnO and ZrO₂ at 320 K. *Comptes Rendus Hebdomadaires Des Seances De L Academie Des Sciences Serie C* **1977**, *285*, 171-174.
153. Titov, V. V.; Milchaylov, R. V.; Lisachenko, A. A., Spectral features of photostimulated oxygen isotope exchange and NO adsorption on "self-sensitized" TiO_{2-x}/TiO₂ in UV-Vis region. *J. Phys. Chem. C* **2014**, *118*, 21986-21994.
154. Pan, J. â. M.; Maschhoff, B. L.; Diebold, U.; Madey, T. E., Interaction of water, oxygen, and hydrogen with TiO₂(110) surfaces having different defect densities. *J. Vac. Sci. Technol. A* **1992**, *10*, 2470-2476.
155. M.L. Knotek, P. J. F., *Phys. Rev. Lett.* **1978**, *40*, 964.
156. Boyd, I. W.; Rimini, E.; Fukushima, K.; Yamada, I., Beam processing and laser chemistry surface smoothness and crystalline structure of ICB deposited TiO₂ films. *Appl. Surf. Sci.* **1989**, *43*, 32-36.
157. Shank, C. V.; Yen, R.; Hirlimann, C., Time-resolved reflectivity measurements of femtosecond-optical-pulse-induced phase transitions in silicon. *Phys. Rev. Lett.* **1983**, *50*, 454-457.
158. Stampfli, P.; Bennemann, K., Time dependence of the laser-induced femtosecond lattice instability of Si and GaAs: Role of longitudinal optical distortions. *Phys. Rev. B* **1994**, *49*, 7299-7305.
159. Zier, T.; Zijlstra, E. S.; Kalitsov, A.; Theodonis, I.; Garcia, M. E., Signatures of nonthermal melting. *Structural Dynamics* **2015**, *2*, 054101.
160. Friedmann, D.; Hansing, H.; Bahnemann, D., Primary processes during the photodeposition of Ag clusters on TiO₂ nanoparticles. *Z. Phys. Chem.* **2007**, *221*, 329-348.

7. References

161. Sato, S.; Kadowaki, T.; Yamaguti, K., Photocatalytic oxygen isotopic exchange between oxygen molecules and the lattice oxygen of TiO₂ prepared from titanium hydroxide. *J. Phys. Chem.* **1984**, *88*, 2930-2931.
162. Parussulo, A. L. A.; Huila, M. F. G.; Araki, K.; Toma, H. E., N₃-dye-induced visible laser anatase-to-rutile phase transition on mesoporous TiO₂ films. *Langmuir* **2011**, *27*, 9094-9099.
163. Wang, C. Y.; Pagel, R.; Dohrmann, J. K.; Bahnemann, D. W., Antenna mechanism and deaggregation concept: novel mechanistic principles for photocatalysis. *C. R. Chimie* **2006**, *9*, 761-773.
164. Montoya, J. F.; Bahnemann, D. W.; Peral, J.; Salvador, P., Catalytic role of TiO₂ terminal oxygen atoms in liquid-phase photocatalytic reactions: oxidation of aromatic compounds in anhydrous acetonitrile. *ChemPhysChem* **2014**, *15*, 2311-2320.
165. Montoya, J. F.; Ivanova, I.; Dillert, R.; Bahnemann, D. W.; Salvador, P.; Peral, J., Catalytic role of surface oxygens in TiO₂ photooxidation reactions: Aqueous benzene photooxidation with (TiO₂) O¹⁸ under anaerobic conditions. *J. Phys. Chem. Lett.* **2013**, *4*, 1415-1422.
166. Mendive, C. B.; Hansmann, D.; Bredow, T.; Bahnemann, D., New insights into the mechanism of TiO₂ photocatalysis: Thermal processes beyond the electron-hole creation. *J. Phys. Chem. C* **2011**, *115*, 19676-19685.
167. Yamakata, A.; Vequizo, J. J. M.; Matsunaga, H., Distinctive behavior of photogenerated electrons and holes in anatase and rutile TiO₂ powders. *J. Phys. Chem. C* **2015**, *119*, 24538-24545.
168. Kafizas, A.; Wang, X.; Pendlebury, S. R.; Barnes, P.; Ling, M.; Sotelo-Vazquez, C.; Quesada-Cabrera, R.; Li, C.; Parkin, I. P.; Durrant, J. R., Where do photogenerated holes go in anatase:Rutile TiO₂? A transient absorption spectroscopy study of charge transfer and lifetime. *J. Phys. Chem. A* **2016**, *120*, 715-723.
169. Yamanaka, K.-i.; Morikawa, T., Charge-carrier dynamics in nitrogen-doped TiO₂ powder studied by femtosecond time-resolved diffuse reflectance spectroscopy. *J. Phys. Chem. C* **2012**, *116*, 1286-1292.
170. Salmi, M.; Tkachenko, N.; Lamminmaki, R. J.; Karvinen, S.; Vehmanen, V.; Lemmetyinen, H., Femtosecond to nanosecond spectroscopy of transition metal-doped TiO₂ particles. *J. Photochem. Photobiol. A* **2005**, *175*, 8-14.
171. Eagles, D. M., Polar modes of lattice vibration and polaron coupling constants in rutile TiO₂. *J. Phys. Chem. Solids* **1964**, *25*, 1243-1251.
172. Tojo, S.; Tachikawa, T.; Fujitsuka, M.; Majima, T., Iodine-doped TiO₂ photocatalysts: Correlation between band structure and mechanism. *J. Phys. Chem. C* **2008**, *112*, 14948-14954.
173. Rajh, T.; Saponjic, Z. V.; Micic, O. I., Reactions of hydrous titanium dioxide colloids with strong oxidizing agents. *Langmuir* **1992**, *8*, 1265-1270.
174. Mohamed, H. H.; Dillert, R.; Bahnemann, D. W., Kinetic and mechanistic investigations of the light induced formation of gold nanoparticles on the surface of TiO₂. *Chem. Eur. J.* **2012**, *18*, 4314-4321.
175. Mohamed, H. H.; Mendive, C. B.; Dillert, R.; Bahnemann, D. W., Kinetic and mechanistic investigations of multielectron transfer reactions induced by stored electrons in TiO₂ nanoparticles: A stopped flow study. *J. Phys. Chem. A* **2011**, *115*, 2139-2147.
176. Richter, S.; Moencke, D.; Zimmermann, F.; Kamitsos, E. I.; Wondraczek, L.; Tuennermann, A.; Nolte, S., Ultrashort pulse induced modifications in ULE - from nanograting formation to laser darkening. *Optical Materials Express* **2015**, *5*, 1834-1850.

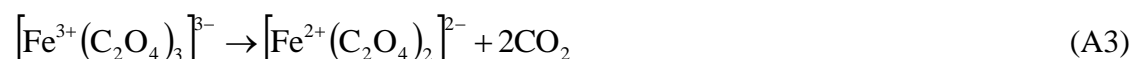
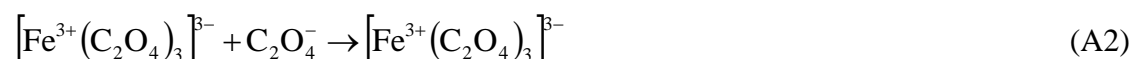
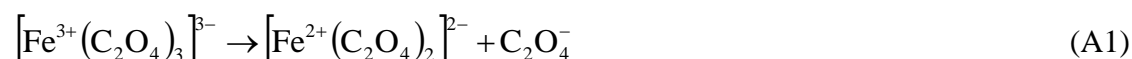
177. Kamat, P. V.; Bedja, I.; Hotchandani, S., Photoinduced charge-transfer between carbon and semiconductor clusters-One electron reduction of C-60 in colloidal TiO₂ semiconductor suspensions. *J. Phys. Chem.* **1994**, *98*, 9137-9142.
178. Meekins, B. H.; Kamat, P. V., Role of water oxidation catalyst IrO₂ in shuttling photogenerated holes across TiO₂ interface. *J. Phys. Chem. Lett.* **2011**, *2*, 2304-2310.
179. Lisachenko, A. A.; Kuznetsov, V. N.; Zakharov, M. N.; Mikhailov, R. V., The interaction of O₂, NO, and N₂O with surface defects of dispersed titanium dioxide. *Kinet. Catal.* **2004**, *45*, 189-197.
180. Won, D.-J.; Wang, C.-H.; Jang, H.-K.; Choi, D.-J., Effects of thermally induced anatase-to-rutile phase transition in MOCVD-grown TiO₂ films on structural and optical properties. *Appl. Phys. A* **2001**, *73*, 595-600.
181. Boschloo, G.; Fitzmaurice, D., Electron accumulation in nanostructured TiO₂ (anatase) electrodes. *J. Phys. Chem. B* **1999**, *103*, 7860-7868.
182. Moringa, K.; Yoshida, H.; Takebe, H., Compositional dependence of absorption spectra of Ti³⁺ in silicate, borate, and phosphate glasses. *J. Am. Ceram. Soc.* **1994**, *77*, 3113-3118.
183. Drouilly, C.; Krafft, J.-M.; Averseng, F. d. r.; Lauron-Pernot, H. l. n.; Bazer-Bachi, D.; Chizallet, C. l.; Lecocq, V.; Costentin, G. n., Role of oxygen vacancies in the basicity of ZnO: From the model methylbutynol conversion to the ethanol transformation application. *Appl. Catal. A: Gen.* **2013**, *453*, 121-129.
184. Cowan, A. J.; Leng, W.; Barnes, P. R. F.; Klug, D. R.; Durrant, J. R., Charge carrier separation in nanostructured TiO₂ photoelectrodes for water splitting. *PCCP* **2013**, *15*, 8772-8778.
185. Safrany, A.; Gao, R.; Rabani, J., Optical properties and reactions of radiation Induced TiO₂ electrons in aqueous colloid solutions. *J. Phys. Chem. B* **2000**, *104*, 5848-5853.
186. Zhang, Z.; Yates, J. T., Jr., Band bending in semiconductors: Chemical and physical consequences at surfaces and interfaces. *Chem. Rev.* **2012**, *112*, 5520-5551.
187. Memming, R., *Semiconductor electrochemistry*. Wiley-VCH: Weinheim 2001.
188. Cheng, H.; Selloni, A., Surface and subsurface oxygen vacancies in anatase and differences with rutile. *Phys. Rev. B* **2009**, *79*, 092101.
189. Colbeau-Justin, C.; Kunst, M.; Huguenin, D., Structural influence on charge-carrier lifetimes in TiO₂ powders studied by microwave absorption. *J. Mater. Sci.* **2003**, *38*, 2429-2437.
190. Ohtani, B., Titania photocatalysis beyond recombination: A critical review. *Catalysts* **2013**, *3*, 942-953.
191. Kirk, A. D.; Namasivayam, C., Errors in ferrioxalate actinometry. *Anal. Chem.* **1983**, *55*, 2428-2429.
192. Hatchard, C. G.; Parker, C. A., *A new sensitive chemical actinometer. II. Potassium ferrioxalate as a standard chemical actinometer*. 1956; Vol. 235, p 518-536.

8. Appendix

A. Determination of the laser intensity

The number of the exciting photons reaching the sample was determined with ferrioxalate actinometry recommended in the ref¹⁹¹: 3 ml of 0.15 M $K_3Fe(C_2O_4)$ in 0.05 M H_2SO_4 were exposed 40 laser pulses and 1 ml of the illuminated solution was transferred to a 10 ml flask and 2 ml of 0.05 % phen/0.75 M $NaCH_3CO_2$ /0.2 M H_2SO_4 developer was added followed by 1 mL of 1 M KF solution plus water to 10 mL.

The irradiation of $K_3Fe(C_2O_4)$ solution leads to the Fe^{3+} reduction *via* the following reactions:



The number of the photo-generated Fe^{2+} ions ($n_{Fe^{2+}}$) was calculated according to:

$$n_{Fe^{2+}} = \frac{N_A V_1 V_3 A_{510}}{V_2 l} \quad (A4)$$

N_A : Avogadro constant

V_1 : volume of $K_3Fe(C_2O_4)$ in 0.05 M H_2SO_4 irradiated with laser (l)

V_2 : volume of the aliquot taken for analysis (l)

V_3 : final volume (l)

l : path length of the spectrophotometer cell (cm)

ϵ : molar extinction coefficient of Fe^{2+} complex ($11100 \text{ l mol}^{-1} \text{ cm}^{-1}$)

The number of the absorbed photons was obtained from:

$$n_a = \frac{n_{Fe^{2+}}}{\Phi_\lambda} \quad (A5)$$

The quantum yield Φ for the Fe^{2+} formation at 351 nm was taken 1.21 and at 248 nm 1.25.¹⁹² Using the Planck equation the number of photons were expressed as energy values and following relation has been found between the relative laser energy measured with a photodiode and the laser energy obtained with actinometry at the excitation wavelengths of 351 nm and 248 nm, respectively:

$$I_{351nm} = 0.12I_{rel} (\pm 0.018) \quad I_{rel} = 30 - 70 \quad (A6)$$

$$I_{248nm} = 1.04I_{rel} (\pm 0.16) \quad I_{rel} = 15 - 45 \quad (A7)$$

8. Appendix

B. Transient absorption spectra under O₂ and N₂

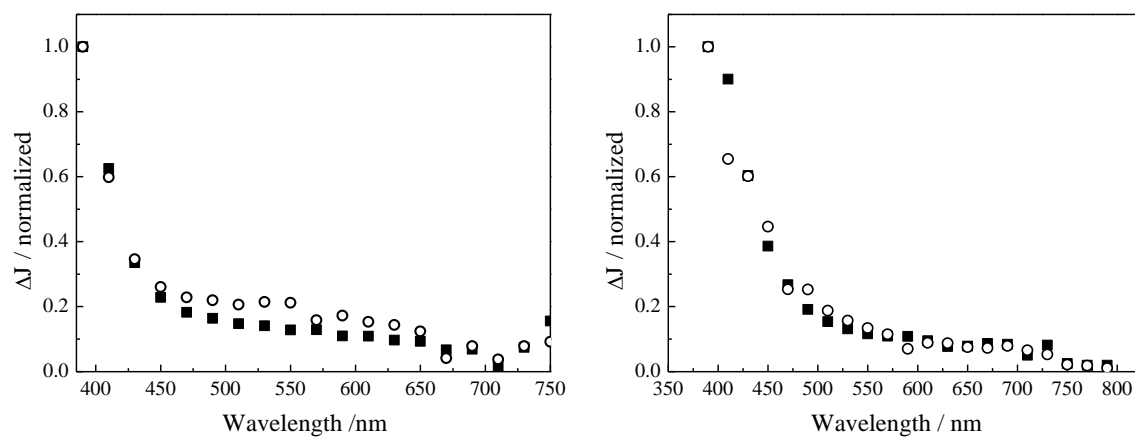


Figure B1: Normalized transient absorption spectra obtained 227 ns after the laser pulse with $\lambda_{\text{exc}} = 351$ nm in the presence of (■) O₂ and (○) N₂ for (left) UV100 and (right) R15.

Publications

1. Borges, K. A.; L. M. Santos, R. M.; Paniago, N. M.; Barbosa, N.; Schneider, J.; Bahnemann, D. W.; T. Patrocínio, A. O.; Machado, A. E. H., Characterization of a high efficient N-doped TiO₂ photocatalyst prepared *via* factorial design. *New J. Chem.* **2016**, DOI: 10.1039/C6NJ00704J.
2. Schneider, J.; Nikitin, N.; Wark, M.; Bahnemann, D. W.; Marschall, R., Improved charge carrier separation in barium tantalate composites investigated by laser flash photolysis. *PCCP* **2016**, *18*, 10719-10726.
3. Hakki, A.; Schneider, J.; Bahnemann, D. W., Understanding the chemistry of photocatalytic processes in: Schneider, J., Bahnemann, D., Ye, J., Puma, G. Li, Dionysiou, D. D. (Eds.), *Photocatalysis: Fundamentals and Perspectives*, RSC, 2016.
4. Etacheri, V.; Valentin, C. Di; Schneider, J.; Bahnemann, D. W.; Pillai, S. C., Visible-light activation of TiO₂ photocatalysts: Advances in theory and experiments. *J. Photochem. Photobiol. C* **2015**, *25*, 1-27.
5. Curti, M.; Schneider, J.; Bahnemann, D. W.; Mendive, C. B., Inverse opal photonic crystals as a strategy to improve photocatalysis: underexplored questions. *J. Phys. Chem. Lett.* **2015**, *6*, 3903-3910.
6. Mendive, C. B.; Bredow, T.; Schneider, J.; Blesa, M.; Bahnemann, D. W., Oxalic acid at the TiO₂/water interface under UV(A) illumination: Surface reaction mechanisms. *J. Catal.* **2015**, *322*, 60-72.
7. Patrocínio, A. O. T.; Schneider, J.; Franca, M. D.; Santos, L. M.; Caixeta, B. P.; Machado, A. E. H.; Bahnemann, D. W., Charge carrier dynamics and photocatalytic behavior of TiO₂ nanopowders submitted to hydrothermal or conventional heat treatment. *RSC Adv.*, **2015**, *5*, 70536-70545.
8. Schneider, J.; Matsuoka, M.; Takeuchi, M.; Zhang, J.; Horiuchi, Y.; Anpo, M.; Bahnemann, D. W., Understanding TiO₂ photocatalysis: Mechanisms and materials. *Chem. Rev.* **2014**, *114*, 9919-9986.
9. Schneider, J.; Kandiel, T.; Bahnemann, D. W., Solar photocatalytic hydrogen production: Current status and future challenges. in: Viswanathan, Balasubramanian, Subramanian, Vaidyanathan Ravi, Lee, Jae Sung (Eds.), *Materials and processes for solar fuel production nanostructure science and technology*, Springer, 2014.
10. Schneider, J.; Bahnemann, D. W., Undesired role of sacrificial reagents in photocatalysis. *J. Phys. Chem. Lett.* **2013**, *4*, 3479-3483.
11. Ivanova, I.; Schneider, J.; Gutzmann, H.; Kliemann, J. O.; Gärtner, F.; Klassen, T.; Bahnemann, D. W., Mendive, C. B., Photocatalytic degradation of oxalic and dichloroacetic acid on TiO₂ coated metal substrates. *Catal. Today* **2013**, *209*, 84-90.
12. Sharifi, M.; Schneider, J.; Wark, M., Investigation on the optimal oxidation agent for a maximum yield of sulfonic acid groups in MCM-41. *Micropor. Mesopor. Mat.*, **2012**, *170*, 506-510.
13. Heinzerling, P.; Boymans, N.; Schneider, J., Goldrubinglas – von alchemistischer Glaskunst bis zur chemischen Nanotechnologie. *Chemkon* **2012**, *19*, 163.

Publications

Books:

J. Schneider, D. W. Bahnemann, J. Ye, G. Li Puma, D. D Dionysiou (Eds.) "Photocatalysis: Fundamentals and Perspectives", RSC Energy and Environment 2016.

D. D Dionysiou, J. Schneider, D. W. Bahnemann, J. Ye, G. Li Puma (Eds.) "Photocatalysis: Applications", RSC Energy and Environment 2016.

Oral presentations:

J. Schneider, T. Kandiel, D. W. Bahnemann, "New insights into the dynamics of charge carriers photogenerated in TiO₂ nanoparticles", 2nd International Conference on Materials for Energy, May 12-16, 2013, Karlsruhe, Germany.

J. Schneider, T. Kandiel, D. W. Bahnemann, "Dynamics of photogenerated charge carriers in different TiO₂ crystal phases", 4th International Conference on Semiconductor Photochemistry (SP 4), June 23-27, 2013, Prague, Czech Republic.

J. Schneider, D. W. Bahnemann, "Sacrificing mechanistic information: The undesired role of sacrificial reagents in photocatalysis", 247th National Spring Meeting of the American-Chemical-Society (ACS), March 16-20, 2014, Dallas, USA.

J. Schneider, A. Hakki, R. Dillert, D. W. Bahnemann, "The use of sacrificial reagents in water photocatalysis: A critical assessment", 20th International Conference on Photochemical Conversion and Storage of Solar Energy (IPS 20), 27 July – 1 August, 2014, Berlin, Germany.

J. Schneider, K. Nikitin, Ralf Dillert, D. W. Bahnemann, "Laser-Flash-Photolysis-Spectroscopy (LFPS): A nondestructive method?", 21st International Conference on Photochemical Conversion and Storage of Solar Energy (IPS 21), July 25-29, 2016, St. Petersburg, Russia.

Curriculum vitae

Personal Data

Name, Forename: Schneider, Jenny
Date of birth: 08.11.1985
Place of Birth: Kokpekty (Kasachstan)

Education

11/2011-08/2016 PhD Study at the Institute of Technical Chemistry, Leibniz University of Hannover: “Nanosecond Laser Flash Photolysis Studies for the Elucidation of Photoinduced Processes in Different TiO₂ Photocatalysts”

04/2011-10/2011 Master Thesis at Institute of Technical Chemistry, Leibniz University of Hannover: “Studies on the Fluorescence Behavior of Semiconductor-Nanoparticles on Ceramic Surfaces”

10/2009 – 10/2011 Master of Science in Material- and Nanochemistry at the Leibniz University of Hannover

10/2006-10/2009 Bachelor of Science in Chemistry at the Leibniz University of Hannover

08/2003-07/2006 Abitur at Herschelschule Hannover